Ore Geology Reviews 140 (2022) 104501

Contents lists available at ScienceDirect

Ore Geology Reviews

journal homepage: www.elsevier.com/locate/oregeorev

Invited Review Article

Trace element geochemistry of iron-(oxy)-hydroxides in Ni(Co)-laterites: Review, new data and implications for ore forming processes

L. Santoro [a,b,*], F. Putzolu [b,c], N. Mondillo [b,c], M. Boni [b,c], R. Herrington [b]

[a] Dipartimento di Scienze della Terra, Università degli Studi di Torino, Via Valperga Caluso 35, 10125 Torino, Italy
[b] Department of Earth Sciences, The Natural History Museum, Cromwell Road, London SW7 5BD, UK
[c] Dipartimento Scienze della Terra, Università di Napoli "Federico II", Complesso Universitario di Monte S. Angelo, Via Cintia 26, 80126 Napoli, Italy

ARTICLE INFO

Keywords:
Goethite
Hematite associated to supergene ore deposits in gossan and oxidation zones
Critical metals (Ni, Co, REEs, Sc, V, Ga, PGEs) deportment within Fe-(oxy)-hydroxides related to Ni(Co)-laterite deposits
Influence of Parent rock and weathering conditions (pH-Eh) on goethite/hematite ratios and goethite-hematite chemistry
Silicon role in trace element uptake of Fe-(oxy)-hydroxides
Goethite potentiality as unconventional ore mineral

ABSTRACT

Iron-(oxy)-hydroxide (FeO/OH) phases are abundant in all supergene ore deposits. The most common FeO/OH phase in supergene environments is goethite, although hematite, lepidocrocite, ferrihydrite, and maghemite can also occur. Natural FeO/OHs are rarely chemically pure, as a range of metal cations can be readily incorporated into their mineral structure. Although an extensive body of literature exists on the scavenging action of synthetic FeO/OHs, there is a general lack of studies of natural systems and, more specifically, of studies dealing with the geochemistry of trace elements in FeO/OHs associated with supergene ores. Furthermore, although it is known that FeO/OHs in supergene ore systems typically contain elevated levels of useful metals like REE, Sc, V, Co, Mn, Cr, and Ni, in most cases, these phases are considered as gangue and hence, the metals are not recovered. Only in the case of Ni(Co)-laterite deposits the FeO/OHs are often exploited for Ni and Co, and sometimes for Sc.

Most previous works on Ni(Co)-laterite deposits have focused on the lateritization process of the parent rocks and the mineralogy of the resulting Ni(Co)-bearing minerals. Only rarely have published studies focused on REE, V, Sc, and PGE deportment within FeO/OHs.

In this study, we describe new mineralogical and chemical data (XRPD, SEM-EDS, EPMA, ICP-AES, LA-ICP-MS, and TEM-HRTEM) obtained from a range of natural FeO/OH samples collected from four important Ni(Co)-laterite deposits, namely Wingellina (Western Australia), Piauí (Brazil), Karaçam and Çaldağ (Turkey). In the course of this study, we investigated the geochemistry of goethite and hematite within the oxidation zone of the respective laterite profiles, evaluating the deportment of minor metals such as Ti, Sc, Cr, Ni, Co, V, Zn, and Mn.

Although derived from different parent rocks located in different geographic areas, the FeO/OH samples collected share a number of common features. In particular, there are commonalities in ore textures, mineralogy, and metal deportment. Based on multivariate statistical analysis, the chemistry of the studied FeO/OHs define three major elemental associations: *i)* Mn–Al–Ti–Sc–V as evident in goethite samples from Wingellina; *ii)* Mg–Ni–Si–Zn as exemplified by samples from Karaçam and Piauí, and *iii)* Cr–V as illustrated by the Çaldağ samples. These contrasting geochemical footprints can be explained in terms of first- and second-order controls with the chemical composition of the parent rock representing the first-order, and favorable pH conditions for the fixation of trace elements within FeO/OHs representing the second-order control. Seasonality and maturation may be additional factors influencing FeO/OHs mineralogy, as periods of arid climate may have favored the dehydration of some FeO/OHs to form more stable species (such as goethite to hematite) over time. In summary, our observations have helped to better understand the ore deposition model relating to surficial weathering systems and have also established the parameters that control the distribution of economically relevant by-product metals in FeO/OHs in diverse conditions during the formation of Ni(Co)-laterites.

1. Introduction

Iron-(oxy)-hydroxides (FeO/OHs) are one of the most ubiquitous mineral groups on Earth (Cornell and Schwertmann, 2003) and can be found in all environments as final products of weathering processes involving the atmosphere, lithosphere, biosphere, pedosphere, and

* Corresponding author at: Dipartimento di Scienze della Terra, Università degli Studi di Torino, Via Valperga Caluso 35, 10125 Torino, Italy.
E-mail address: licia.santoro@unito.it (L. Santoro).

https://doi.org/10.1016/j.oregeorev.2021.104501
Received 2 March 2021; Received in revised form 22 September 2021; Accepted 23 September 2021
Available online 28 September 2021

hydrosphere (Cornell and Schwertmann, 2003; Faivre and Frankel, 2016). Their primary genesis is related to a range of diverse thermodynamic, geochemical, and biological processes such as crystallization of Fe minerals from magmatic melts, dissolution, transport, mineral precipitation from hydrothermal fluids, and finally supergene processes. In the secondary environment, they can form by the weathering of primary phases with physical or geochemical redistribution through erosion and mechanical transport from the lithosphere/pedosphere to the atmosphere and hydrosphere, with final precipitation of minerals in oxidative environments or by biogenic processes (Cornell and Schwertmann, 2003). As a result, FeO/OH are widely distributed in soils, weathered rocks, lakes, and river sediments (Lindsley, 1991). Their abundance, physio-chemical properties, and high stability in a wide range of environments have led to the study of FeO/OH phases in a wide range of scientific fields such as geochemistry, geology, mineralogy, environmental sciences, engineering, medicine, biology, and industrial chemistry (Cornell and Schwertmann, 2003; Schwertmann and Cornell, 2007; Villacís-García et al., 2015; Faivre and Frankel, 2016).

Cornell and Schwertmann (2003) and Faivre and Frankel (2016) document 16 known iron oxides, hydroxides, or oxy-hydroxides, 13 of which can be found in nature. These Fe-phases can be discriminated on grounds of their composition and, specifically, on *i)* the occurrence of Fe^{2+}, Fe^{3+} or both in the mineral structure, and *ii)* the occurrence of "O" or "OH" or both. The most abundant FeO/OHs phases occurring in nature are goethite *sensu stricto* [α-$Fe^{3+}O(OH)$], hematite (α-$Fe^{3+}{}_2O_3$), and magnetite ($Fe^{3+}{}_2Fe^{2+}O_4$), followed by the goethite polymorph lepidocrocite [γ-$Fe^{3+}O(OH)$], maghemite (γ-$Fe^{3+}{}_2O_3$), ferrihydrite [5 $Fe^{3+}{}_2O_3{\cdot}9H_2O$; $Fe^{3+}{}_5O_7(OH){\cdot}4H_2O$; $Fe^{3+}{}_5O_3(OH)_9$, $Fe^{3+}{}_4O_5(OH)_2{\cdot}2.6H_2O)_{12}$; $Fe^{3+}{}_{10}O_{14}(OH)_2$] (Towe and Bradley, 1967; Fleischer et al., 1975; Russel, 1979; Michel et al., 2007), schwertmannite [$Fe^{3+}{}_8O_8(OH)_6(SO)nH_2O$], and the rare goethite polymorph akaganeite (β-$Fe^{3+}OOH$).

Goethite is the end member of many mineral transformations and is also the most stable FeO/OH phase thermodynamically, so it is ubiquitous in rocks and soils under oxidizing conditions. Goethite has two further polymorphs: Lepidocrocite and akaganeite (Mackay, 1962). The former occurs in rock and soils as an oxidation product of Fe^{2+}, while the latter is rare and mostly found in marine environments (Cornell and Schwertmann, 2003). Schwertmannite is very poorly crystalline, contains sulfur and so is a common oxidation product of pyrite or occurs as a precipitate from acid mine waters. Ferrihydrite commonly occurs as nanometre-scaled particles suspended in the aqueous fraction of soils and weathered rocks, in precipitates around cold and hot springs, and in acid mine effluents (Childs, 1992; Fortin and Langley, 2005). Ferrihydrite is a common precursor to goethite and hematite in soils and sedimentary systems and transforms rapidly due to its thermodynamic instability (Schwertmann et al., 2004; Cudennec and Lecerf, 2006). In fact, the conversion of ferrihydrite into more stable Fe-phases by dissolution and re-precipitation of goethite and/or hematite is common under both acidic and basic conditions (Schwertmann and Murad, 1983; Nagano et al., 1994; Cornell and Schwertmann, 2003). Although ferrihydrite can commonly coexist with other FeO/OHs like goethite, its identification in soils and rocks is problematic using routine analyses such as X-ray Powder Diffraction due to its poor crystallinity (Faivre and Frankel, 2016). Hematite and magnetite are widespread in rocks and soils and may have a magmatic, hydrothermal, or low-temperature biogenic origins; both phases are susceptible to supergene modification, and hematite occurs as the end phase from both ferrihydrite and goethite transformations (Cornell and Schwertmann, 2003). Maghemite is a common weathering product of magnetite, whilst a phase known as "*green rust*" is a product of corrosion observed in anoxic soils (Faivre and Frankel, 2016), and comprise a mixed-valence iron mineral consisting of layers of $Fe^{2+}OH$, where Fe^{2+} is locally replaced by Fe^{3+}, with a Fe^{2+}/Fe^{3+} ratio between 0.8 and 3.6.

A number of the FeO/OH minerals, largely magnetite, hematite, and goethite, form the main iron ore minerals in Fe-*skarns, banded iron formation* (BIF) and *oolitic ironstones* (Einaudi and Burt, 1982; Morris, 1985; Morris, 2002; Siehl and Thein, 1989; Heikoop et al., 1996; Taylor et al., 2001; Kneeshaw and Kepert, 2002; Klein, 2005; Mücke, and Farshad, 2005; Bekker et al., 2010; Bekker et al., 2014).

In laterites, ore deposits form through the breakdown of primary minerals (e.g., sulfides and silicates) as consequence of their interaction with meteoric waters. During this process, the more soluble chemical elements of the parent rocks are leached while poorly soluble elements remain in place, forming stable residual and secondary minerals. The features of the weathering profile (e.g., its thickness, mineralogy, geochemistry), and the type of the final supergene assemblages are controlled by the nature of the parent rock/primary ores, the uplift rate, and the prevailing climatic conditions (Bárdossy and Aleva, 1990; Chavez, 2000; Large, 2001; Boni and Large, 2003; Gleeson et al., 2003; Hitzman et al., 2003; Golightly, 2010). Typical examples of supergene deposits are metal-bearing laterites, bauxites, supergene Cu- and non-sulfide Zn/Pb-nonsulfide systems. In these deposit types, FeO/OHs are mostly concentrated in the upper residual portions of the ore deposit (also known as cap, ferricrete, duricrust, gossan, oxide zone), although they can also occur throughout the weathering profile and in the "*limonite*" horizon of laterite deposits. The FeO/OHs in supergene ore deposits are commonly poorly crystalline (fine-grained nano/microcrystalline textures) and often occur with Mn-(oxy)-hydroxides and nano/microcrystalline to amorphous silica. Due to the poor crystallinity, the mineralogy of FeO/OHs in supergene deposits was typically poorly defined, leading to the term "*limonite*", covering minerals of general chemical formula (FeOOH)*nH_2O. Limonite is shown to be dominated by goethite (Kelly, 1957) and although obsolete, the term "*limonite*" is still widely used in the mining industry to indicate a distinct zone in the weathering profiles of laterite deposits. However, in the scientific literature, the use of the term"*limonite*" has been replaced by the terms "*oxide zone*" and "*oxide ore*".

The weathering process that results in the formation of supergene ore deposits can also trigger the remobilization and the enrichment of a range of potentially valuable metals (e.g., Ni, Zn, Pb, Co, Mn, REE, Sc, Ga, Ge, In) as well as potentially deleterious elements (e.g., Hg, Cd, Cr, Tl). During this process, FeO/OHs that formed from the breakdown of iron-rich sulfide and silicate phases (e.g., pyrite, pyrrhotite, olivine, amphibole, pyroxene) play a primary role in scavenging the above-listed metals; in fact, they can adsorb or incorporate a suite of metals into their crystalline structure (Cornell and Schwertmann, 2003; Santoro et al., 2020).

Natural goethite is seldom chemically pure as it generally hosts a wide range of metal cations in its structure, which can be either isovalent (e.g., Al^{3+}, Co^{3+}, Sc^{3+}) or heterovalent (e.g., Ni^{2+}, Zn^{2+}, Cd^{2+}) with respect to Fe^{3+}. The process of scavenging trace elements is the result of the physical and chemical properties of the FeO/OHs, namely the high specific surface areas of the particles and strong affinities for the surface-binding heavy metals (Fendorf et al., 1997; Villalobos and Leckie, 2001; Cornell and Schwertmann, 2003; Antelo et al., 2005; Granados-Correa et al., 2011; Perelomov et al., 2011).

In extreme cases, the uptake of valuable metals in goethite reaches levels that can be considered economic for exploitation. For example, Ni (Co)-laterites goethites may contain up to 4% Ni and 0.5% Co (Eliopoulos and Economou-Eliopoulos, 2000; Herrington, 2012) and may also be potential targets for Sc, which is found to be mostly concentrated in goethite, and less in hematite or clay minerals (Audet, 2008; Aiglsperger et al., 2015; Aiglsperger et al., 2016; Chassé et al., 2017; Chassé et al., 2019; Teitler et al., 2019; Ulrich et al., 2019). According to a recent study by Levard et al. (2018), a nearly continuous solid-solution between the αFeOOH and αScOOH species can be obtained under laboratory conditions despite the significant differences in the atomic radii between the Fe^{3+} and Sc^{3+} cations. These findings have provided important insights for predicting the geochemical behavior of Sc in secondary Fe-rich natural systems.

Trace metal-rich FeO/OHs are also abundant in bauxites and in "*red muds*", the waste products of the Bayer process used for bauxite

Table 1
List of Ni-laterite deposits reported in the text by references: provenance, protolith and critical elements deportment within FeO/OHs.

Location	Deposit	Type	Protolith lithology	Primary mineralogy (magmatic to hydrothermal)	Supergene mineralogical association	Geochemistry of FeO/OHs	Reference
New Caledonia	Konianmbo, Bien Sûr	hydrous Mg-silicate type	serpentinized harzburgite	opx > ol > cpx; amph, Cr-sp, mt, srp	*goe* > *hm;* MnO/OH, smc, tlc	**goe*: 1776–7082 ppm Ni; 34 – 1860 ppm Co; 661–4652 ppm Mn; 11,000–42,800 ppm Cr, 50–136 ppm Sc; 200–500 ppm V; *hm*: 1752–6242 ppm Ni; 61.4–1784 ppm Co; 68–6479 ppm Mn; 6400-49,700 ppm Cr; 30–76 ppm Sc and 146–302 ppm V	Dublet et al. (2012), Dublet et al. (2015), Cathelineau et al. (2017), Muñoz et al. (2019), Ulrich et al. (2019)
	Koniambo, Nakéty		serpentinized harzburgite	opx > ol > cpx; amph, Cr-sp, mt, srp	*goe* > *hm;* MnO/OH, smc, tlc	**goe*: up to ~10,000 ppm Ni; up to ~125 ppm Sc;	Teitler et al. (2019)
	N'Go, Cap Bocage		serpentinized dunite + harzburgite	opx > ol > cpx; amph, Cr-sp, mt, srp			
	Tiebaghi		serpentinized lherzolite	opx + cpx > ol; Cr-sp, mt, srp			
	Koniambo, N'Go, Tiebaghi		gabbro dykes	plag > amph; Fe-Ti ox, mt	*hm* > *goe;* kln > AlOOH	**hm*: <~50 ppm Sc	
	N'Go, Nakéty		amphibolite dykes	amph > opx; Fe-Ti ox, ttn	*goe* > *hm;* AlOOH > kln, smc	**goe*: up to ~10,000 ppm Ni; up to ~300ppm Co; up to ~800 ppm Sc	
	Goro	hydrous Mg-silicate type/oxide type	serpentinized harzburgite-dunite	amph, chl, opx, srp,	*goe* > *hm;* tlc, smc	scarce info on the FeO/OH geochemistry	Wells et al. (2009), Dublet et al. (2015), Dublet et al. (2017)
Indonesia	Soroako area	hydrous Mg-silicate type	variably serpentinised harzburgite	ol, opx > srp; chl, Cr-sp, mt	*goe, mgh* > *hm;* Ni-srp, smc, tlc	scarce info on the FeO/OH geochemistry	Golightly and Arancibia (1979), Sufriadin et al. (2011), Ilyas and Koike (2012), Maulana et al. (2016)
	Kolondale area		serpentinized harzburgite	srp > opx; ol > cpx	*goe* > *hm*; smc, tlc,	scarce info on the FeO/OH geochemistry	Fu et al. (2014), Fu et al. (2018)
	Weda Bay (kln Rahai area)		dunite-harzburgite	Cr-sp, ol, opx, srp	*goe* > *hm;* MnO/OH, smc, tlc	****goe: ~1–2 wt% NiO. Scarce info on FeO/OH geochemistry.	Farrokhpay et al. (2019)
Philippines	Pujada	hydrous Mg-silicate type	dunite-harzburgite and clynopyroxenites	N/A	*goe* +MnO/OH + srp + sep	*****limonite:avg 0.2 wt% Co; avg.1.6 wt% Cr; avg.2.2 wt% Mn; avg.1.6wt% Ni	Santos-Ynigo (1965), Fan and Gerson (2011)
	Intex		dunite-harzburgite, clynopyroxenite, lherzolite	Cr-sp, cpx, mt, ol, opx, srp	*goe* > *hm;* MnO/OH, tlc	***goe:* 0.24–0.79 wt% NiO; 0.10–0.27 wt% CoO; 0.15–1.78 wt% MnO; 0.34–0.96 wt% Cr_2O_3, 1.46-6.49 wt% Al_2O_3; *hm:* 0.13–0.41wt% NiO; 0.64–0.16wt% CoO; 0.19–1.04 wt% MnO; 0.08–0.10 wt% Cr_2O_3; 0.08–0.10 wt% Al_2O_3	Tupaz et al. (2020a)
	Berong		serpentinized harzburgite	brc, Cr-sp, mgs, mt, ol, opx, sep, srp	*goe* > *hm;* AlOOH, MnOH, tlc,	*goe*:0.75–1.71 wt% NiO; 0.11–0.65 wt% CoO; avg. 0.35–5.91 wt% MnO; 0.25–0.81 wt% Cr_2O_3; 3.35–10.68 wt% Al_2O_3; *hm:* 0.85wt% NiO; 0.49 wt% CoO; avg. 1.04 wt% MnO; avg.0.36wt% Cr_2O_3; 0.51 wt% Al_2O_3	Tupaz et al. (2020b)
Cuba	Moa-Baracoa, Mayari Crystal	oxide type	serpentinized harzburgite	Cr-sp, mt, ol, opx, srp	*goe* > *mgh, hm;* AlOOH, MnO/OH	scarce info on the FeO/OH geochemistry	Lewis et al. (2006), Marchesi et al. (2006), Aiglsperger et al. (2016)
Domenican Republic	Loma Ortega	hydrous Mg-silicate type	serpentinized peridotite	ol, opx, cpx, srp	*goe* > *hm* > *mgh;* MnO/OH, sep, sme	scarce info on the FeO/OH geochemistry	Tauler et al. (2017)
	Facondo		serpentinized dunite±harzburgite	ol, opx, srp	*goe* > *hm* > *mgh;* AlOOH, MnO/OH, sep		Lewis et al. (2006), Aiglsperger et al. (2015)

(*continued on next page*)

Table 1 (*continued*)

Location	Deposit	Type	Protolith lithology	Primary mineralogy (magmatic to hydrothermal)	Supergene mineralogical association	Geochemistry of FeO/OHs	Reference
Australia	Bulong and Siberia	smectite/ oxide type	serpentinized dunite, pyroxenite/peridotite sills cutting dolerite	srp > ol; amph, chl, Cr-sp, mt, srp	*goe* > > *hm, mgh*; kln, MnO/OH, Ni-srp, smc, tlc	scarce info on the FeO/OH geochemistry	Elias et al. (1981), Elias et al. (2006)
	Murrin Murrin	smectite type	serpentinized dunite and peridotites	chl, Cr-sp, mt, ol, srp	*goe* > *hm,* mgm; kln, mgs, smc	scarce info on the FeO/OH geochemistry	Gaudin et al. (2015)
	Wingellina	oxide type	serpentinized dunites, peridotites and gabbro/ gabbronorite	chl, Cr-sp, ol, srp	*goe* > *hm;* AlOOH, kln, MnO/OH, smc	******goe*: avg. 1.4 wt% NiO; avg. 0.86 wt% CoO; avg. 0.88 Cr_2O_3; avg. 3.1 MnO; *hm*: avg. 0.64 wt% NiO; avg. 0.68% wt % CoO; avg. 0.89 Cr_2O_3 avg. 2.07 MnO	Putzolu et al. (2018), Putzolu et al. (2019)
	Syerston-Flemington		clynopyroxenite	cpx > > opx; grt	*hm* > *goe, mgm*; AlOOH, kln, smc	******goe*: avg. 690–1500 ppm; *hm*: avg. 148–680 ppm	Chassé et al. (2017). Chassé et al. (2019)
Greece	Kastoria	oxide type	serpentinised peridotite	Cr-sp, ol, srp	*goe* > *hm;* MnO/ OH, tlc,	******goe*: 0.70–1.46 wt% NiO; 0.55–2.22 wt% MnO; 0.78–3.68 Cr_2O_3; 2.02–2.58 wt % Al_2O_3	Eliopoulos and Economou-Eliopoulos (2000)
	Profitis		harzburgite, dunite and orthopyroxenite	opx > ol; chl	*goe* > *hm;* tlc	******goe*: 0.12–0.87 wt% MnO; 0.49–1.03 wt% Cr_2O_3;	
	Nissi	bauxite-laterite	allochtonous material	N/A	*goe* > *hm;* AlOOH; ill, kln, MnO/OH, mnt, smc, tlc	******goe*: 0.00–1.00 wt% NiO; 0.19–1.07 wt% MnO; 0.30–1.70 wt% Cr_2O_3; 2.22–3.69 wt% Al_2O_3	
	Parhari		serpentinized dunite-harzburgite	Cr-sp, chl, ol, opx, prvk, Ti-ox	*goe* > *hm*, AlOOH, ill	******goe:* 0.18–0.23 wt% MnO; 0.30–0.31 wt% Cr_2O_3; 0.77–2.03 wt% Al_2O_3	
	Patitira	bauxite-laterite	allochtonous material	N/A	*goe* > *hm;* AlOOH; ill, kln, MnO/OH, mnt, smc, tlc	*******goe*: 0.6-1–4 wt% NiO; 0.4 wt% MnO;0.3–0.7 wt% Cr_2O_3; 2.1–10 wt% Al_2O_3	Gamaletsos et al. (2018)
Albania	Bitincke	oxide type	serpentinized peridotite	srp > opx, ol; Cr-sp	*goe;* MnO/OH, mnt, smc	scarce info on the FeO/OH geochemistry	Thorne et al. (2012)
Turkey	Karaçam	oxide type	serpentinized cumulate peridotite (harzburgite and lherzolite	N/A	N/A	N/A	Herrington et al. (in review)
	Çaldağ		serpentinized peridotite and serpentinite	srp > opx, ol; Cr-sp, mgs,	*goe* > *hm*; MnOH	scarce info on the FeO/OH geochemistry	Thorne et al. (2009)
	Gordes	smectite/ oxide type?/ hydrous Mg type???	serpentinized peridotite	chl, srp	*goe* > *hm*; MnOH, smc	*******goe:* avg. 0.75–2.22 wt% Cr_2O_3; avg. 0.36–1.34 wt% MnO; avg. 0.52–391 wt% NiO; avg. 1.21–6.9 wt% As_2O_3	Eliopoulos et al. (2012)
	Sarıçimen (Çaldıran-Van)	oxide/ smectite type?	serpentinized harzburgite	chl, Cr-sp, mill, mt, ol, opx	*goe, hm, mgh;* MnO/OH, tlc	scarce info on the FeO/OH geochemistry	Çolakoğlu and Arehart (2010)
Oman	Ibra	oxide type	gabbro	cpx, mt, plag, srp	*hem* > *goe, mgh;* AlOOH, ill, mnt, mt, smc, tlc	******goe:* 0.27–0.84wt% NiO; 0.06–0.16 wt% CoO; 0.12–0.32 wt% MnO; 0.71–2.71 wt% Cr_2O_3; 3.14–5.23 wt% Al_2O_3; *hm:* 0.03–1.4 wt% NiO; 0.00–0.52 wt% CoO; 0.2–1.11 wt% MnO; 0.1–4.9 wt% Cr_2O_3; 0.2–5.6 wt % Al_2O_3	Al-Khirbash (2015) and Al-Khirbash (2016)
	East Ibra		serpentinized harzburgite–dunite	chl, cpx, mt, nep, srp	*goe* > *hm, mgh;* AlOOH, ill, mnt, mt, smc, tlc	******goe:* 0.05–0.62 wt% NiO; 0.00–0.08 wt% CoO; 0.02–1.4 wt% MnO; 0.03–2.24 wt% Cr_2O_3; 0.14–4.75 wt% Al_2O_3; *hm:* 0.07–0.9 wt% NiO; 0.026–0.28 wt% CoO; 0.03–1.95 wt% MnO; 0.1–2.22 wt% Cr_2O_3; 0.011–2.87wt% Al_2O_3	
	Tiwi					******goe:* 0.00–1.35 wt%NiO; 0.00–0.17 wt%CoO; 0.01–0.82 wt% MnO; 0.00–1.66 wt% Cr_2O_3; 0.01–8.21 wt% Al_2O_3; *hm:* 0.003–0.61 wt% NiO; 0.00–0.09 wt% CoO; 0.5–0.38wt% MnO; 0.1–1.31 wt% Cr_2O_3; 0.1–4.5 wt% Al_2O_3;	

(*continued on next page*)

Table 1 (*continued*)

Location	Deposit	Type	Protolith lithology	Primary mineralogy (magmatic to hydrothermal)	Supergene mineralogical association	Geochemistry of FeO/OHs	Reference
	Al–Russayl					**goe:* 0.08–2.38wt% NiO; 0.02–0.69 wt% CoO; 0.01–1.71 wt% MnO; 0.05–2.98 wt% Cr_2O_3; 0.01–6.96 wt% Al_2O_3; *hm:* 0.21–0.28 wt% NiO; 0.11–0.42 wt% CoO; 0.89–01.95 wt% MnO; 0.00–0.23 wt% Cr_2O_3; 0.01–0.02 wt% Al_2O_3	
Cameroon	Nkamouna	oxide type	serpentinized peridotite and gabbro	brc, sp, mgs, mt, ol, srp, px	*goe, hm, mgm;* AlOOH, kln,MnO/OH, smc	scarce info on the FeO/OH geochemistry	Lambiv Dzemua and Gleeson (2012), Lambiv Dzemua et al. (2013)
Ivory Coast	Sipilou, Moyango	smectite type	serpentinized dunite	chl, Cr-sp, mt, ol, opx, srp	*goe, hm, mgh;* AlOOH, kln, smc, tlc,	scarce info on the FeO/OH geochemistry	Nahon et al. (1982)
Colombia	Cerro Matoso	hydrous Mg-silicate type/oxide type	serpentinized harzburgite	Cr-sp, ol, opx, srp	*goe, hm, mgh;* AlOOH, mgs, sep, smc, tlc,	scarce info on the FeO/OH geochemistry	Gleeson et al. (2004), Tobón et al., 2020
	Planeta Rica	hydrous Mg-silicate type	high serpentinized harzburgite and gabbros	mt, ol, opx, srp		scarce info on the FeO/OH geochemistry	
Brazil	Santa Fè	oxide type	serpentinized dunite, peridotite and pyroxenite	amph, chl, Cr-sp, Fe-Ti ox, Fe-Ni-sph, mt, ol, opx, prvk, srp	*goe* > *hm;* AlOOH, MnO/OH, Ti-ox; smc	**goe:* 0.41–1.63 wt%NiO; o.19–0.39 wt% CoO; 0.14–0.59 wt% MnO; 0.66–1.88 wt% Cr_2O_3: 3.4–5.57 wt% Al_2O_3; *hm:* 0.22–0.85 wt% NiO; 0.34–0.43 CoO; 0.14–1.59 wt% MnO; 0.13–0.67 wt% Cr_2O_3; 0.09–2.95 wt% Al_2O_3	Putzolu et al. (2021)
	Niquelândia	smectite type	serpentinized dunite, peridotite and pyroxenite	chr, opx, cpx, ol, srp	*goe* > *hm,*kln, mgs, smc,	scarce info on the FeO/OH geochemistry	Colin et al. (1990), Mano et al. (2014)
	Barro Alto		serpentinized dunite, harzburgite, pyroxenite and gabbronorite	amph, chl, Cr-sp, ol, srp	*hm, goe;* sep, smc, tlc	scarce info on the FeO/OH geochemistry	Ratiè et al. (2015)

Notes: abbreviation: amph=amphibole; bt=biotite; brc=brucite; chl= chlorite; cpx=clynopyroxene; Cr-sp=Cr-spinel; Fe-Ti ox= ilmenite; rutile; goe=goethite; grt=granet;
N/A = not applicable.
* = LA-ICP-MS;
** = EPMA;
*** = SEM-EDS;

treatment. For example, Mondillo et al. (2019) showed that FeO/OHs in bauxite can incorporate various amounts of Sc, V, Cr, Co, Ni, and REE and that these concentrations can be detected within FeO/OHs contained in *red muds* (Logomerac, 1971; Borra et al., 2015; Borra et al., 2016a; Borra et al., 2016b; Deady et al., 2016; Zhang et al., 2016; Davris et al., 2016; Davris et al., 2017; Reid et al., 2017; Akcil et al., 2018; Bolanz et al., 2018; Rivera et al., 2018; Tóth et al., 2019). Iron oxide-hydroxides in Zn-nonsulfide deposits also contain variable amounts of valuable metals such as Ge, Zn, and Pb (Mondillo et al., 2014; Mondillo et al., 2018a; Mondillo et al., 2018b; Santoro et al., 2013; Santoro et al., 2014; Santoro et al., 2015; Santoro et al., 2020).

Innovative hydrometallurgical and bioprocessing methods targeting the dissolution of minerals show that significant Ni, Co, Sc, and V could potentially be recovered directly from FeO/OHs and hence, a deeper understanding of the geochemistry of FeO/OHs is critical to the evaluation of these phases as unconventional sources of economic metals. For this reason, in this contribution, we firstly review previous studies focused on the natural FeO/OHs occurring in the *"oxide zone"* of Ni(Co)-laterites to unravel the formation processes that may favor metal uptake into FeO/OHs, and secondly present the findings of a mineralogical and geochemical characterization of four geologically and geographically diverse Ni(Co)-laterite deposits: Wingellina (Western Australia), Piauí (Brazil), Karaçam and Çaldağ (Turkey). Our work delivered a detailed geochemical characterization of FeO/OHs aimed to better define the most favorable formation conditions and the factors leading to metal enrichment in laterite ore deposits. Based on the results we were able to identify possible geochemical and genetic similarities between the studied laterite deposits and other deposits of this type worldwide.

2. Current understanding of natural iron-(oxy)-hydroxides within Ni-laterite deposits

Most of the existing literature on supergene ore deposits focuses on the currently exploited ore minerals (such as garnierite, nepouite, asbolane, lithiophorite, nontronite, etc.), typically neglecting FeO/OHs, which have been covered in only a cursory manner. The following paragraphs summarize the existing literature, focusing on the morphology, petrography, and geochemistry of FeO/OHs associated with Ni(Co)-laterite deposits (Table 1). It is important to note here that analyses carried out in previous studies may not be comparable to the new data collected using state-of-the-art methods.

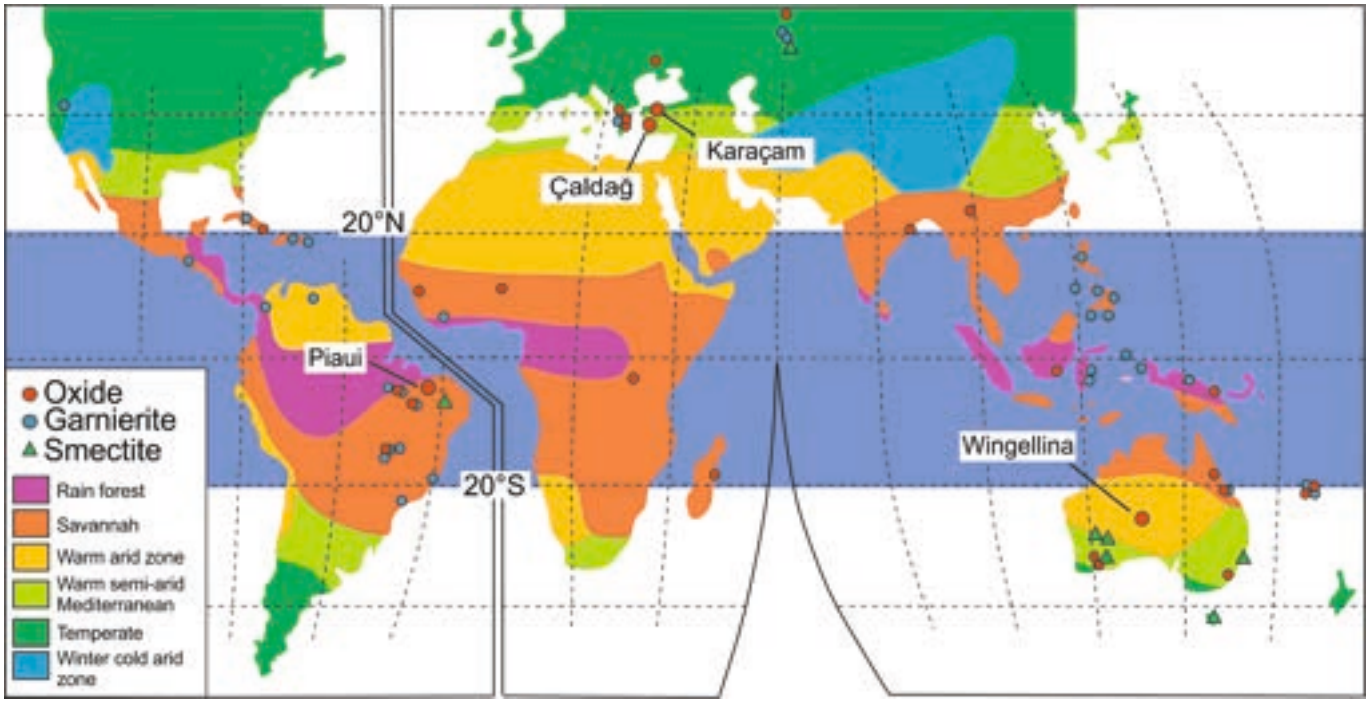

Fig. 1. Morphoclimatic map showing the location of the selected iron-(oxy)-hydroxides-rich Ni(Co)-laterite samples in the context of the major worldwide laterite districts. The optimal climatic zone for lateritic weathering, stretching from 22°N to 22°S of latitude, is highlighted in blue (modified after Butt and Cluzel, 2013; Putzolu, 2021). (For interpretation of the references to color in this figure legend, the reader is referred to the web version of this article.)

2.1. Ni(Co)-laterite deposits: genesis, classification, and role of iron-(oxy)-hydroxides in determining the metals distribution

Ni(Co)-laterites are principally targeted for Ni and Co, although important research has been carried out evaluating their potential as sources of Sc, REEs, PGEs and V (Aiglsperger et al., 2015; Aiglsperger et al., 2016; Chassé et al., 2017; Chassé et al., 2019; Teitler et al., 2019; Ulrich et al., 2019). Ni(Co)-laterites form from mafic and ultramafic rocks weathered under tropical to sub-tropical conditions. During such weathering, the hydrolysis of ferromagnesian minerals (i.e., olivine and pyroxene) triggers the neo-formation of Ni-phyllosilicates (i.e., garnierite and smectite) as well as Ni- and Co-bearing oxy-hydroxides, with FeO/OHs being the most common components (Golightly, 2010; Butt and Cluzel, 2013; Myagkiy et al., 2017). In general, a Ni(Co)-laterite profile consists of from bottom to top: *i)* bedrock, usually consisting of peridotites, dunites, and their serpentinized counterparts; *ii)* saprolite zone, containing the remnants of the protolith embedded in newly formed Ni-bearing phyllosilicates (garnierite and/or smectite), with subordinate goethite and relict spinel; *iii)* transition zone, commonly corresponding to a mottled clay-rich horizon; *iv)* oxide zone (historically referred to as the limonite zone), whose mineralogical association consists mainly of goethite with minor hematite, maghemite, gibbsite and lithiophorite-asbolane; *v)* iron cap, with hematite and goethite as the main minerals. Ni(Co)-laterites have been subdivided into three main types, although mixed-type deposits are also common (Brand et al., 1998; Gleeson et al., 2003; Freyssinet et al., 2005; Golightly, 2010; Berger et al., 2011; Butt and Cluzel, 2013; Putzolu et al., 2019): *i)* oxide-type deposits, where the main regolith unit is the ferruginous saprolite: in this ore type FeO/OHs, together with Mn-(oxy)-hydroxides, are the main sources of Ni and Co; *ii)* clay-silicate type deposits, dominated by Ni-bearing smectites in saprolite; *iii)* hydrous Mg-silicate deposits known as "*garnierite-type ores*", where Ni is hosted in mineralogically complex mixtures of serpentine, talc and sepiolite, in veins and fractures or in the porosity of the rocks in the saprolite zone (Gleeson et al., 2003; Freyssinet et al., 2005). Recently formed (Tertiary) Ni-laterite deposits occur at a latitude of about ± 22° from the equator. Several main districts can be recognized (Fig. 1): *a)* Southern Pacific (New Caledonia, Philippines, and Indonesia) (e.g., Teitler et al., 2019; Ulrich et al., 2019; Tupaz et al., 2020a; Tupaz et al., 2020b); *b)* Caribbean islands (Cuba, Dominican Republic) (e.g., Villanova-de-Benavent et al., 2014; Aiglsperger et al., 2016); *c)* Australia (Elias, 2006); *d)* Brazil (de Oliveira et al., 1992); *e)* other less important districts located in Western Africa (Nahon et al., 1982) and in the Mediterranean realm (Herrington et al., 2016). It is worth mentioning that the Mediterranean deposits (e.g., those in Albania, Greece and Turkey), as well as those in the Urals and Australia, are located outside the zone of current optimal climatic conditions and thus, represent products of paleo-weathering processes (Freyssinet et al., 2005; Herrington et al. 2007).

As reported above, recent studies discuss the Ni(Co)-laterites as a source of useful metals other than Ni and Co. For example, several works have addressed the Sc behavior in laterite deposits from mining districts in Australia, New Caledonia, Cuba, and Dominican Republic (Aiglsperger et al., 2016; Chassé et al., 2017; Chassé et al., 2019; Putzolu et al., 2019; Teitler et al., 2019; Ulrich et al., 2019). This work showed that Sc enrichment is largely controlled by *i)* the nature of the magmatic protolith (i.e., it has to be enriched in both amphibolite and pyroxenite), *ii)* by the concentration in secondary weathering products (i.e., FeO/OHs and smectite) and *iii)* its behavior in the weathering profile as a result of the aging and recrystallization of supergene phases. Aiglsperger et al. (2015) and Aiglsperger et al. (2016) assessed the potential of the Dominican Republic and Cuban laterites for hosting economic concentrations of PGEs. The results highlighted that PGEs might also be upgraded during weathering in the oxide zone because of secondary processes resulting in the genesis of PGE nanoalloys in the weathering residue. More recent studies recorded subeconomic REE enrichment in Ni-laterites of the Dominican Republic, Australia, and New Caledonia (Aiglsperger et al., 2015; Putzolu et al., 2019; Ulrich et al., 2019), where REEs are mostly accommodated in Mn-oxy-hydroxides, or alternatively form discrete REE-phases (Ce-oxides) with traces recorded in FeO/OHs and clays.

2.1.1. Iron-(oxy)-hydroxides in the southern Pacific Ni(Co)-laterite area

2.1.1.1. New Caledonia. New Caledonian laterites account for ~9% of the global mined supply of Ni metal, with an annual production of ~200,000 tons (USGS, 2021; INSG, 2021). The Ni(Co)-laterites of New Caledonia developed from the weathering of ophiolites (the "Peridotite Nappe" Avias, 1967), consisting of ultramafic to mafic rocks (harzburgites, lherzolites, dunites, pyroxenites, gabbros, amphibolites) (Prinzhofer et al., 1980; Prinzhofer and Allègre, 1985; Cluzel et al., 2001; Cluzel et al., 2012; Marchesi et al., 2009; Ulrich et al., 2010; Pirard et al., 2013). Except for at Goro, where exploitable Ni reserves are also found in the goethite-rich oxide zone (e.g., Wells et al., 2009; Maurizot et al., 2019), the vast majority of New Caledonian Ni-laterites are classified as belonging to the hydrous Mg-silicate type, with Ni mainly concentrated in "*garnierite*" (Manceau and Calas, 1985; Dublet et al., 2012; Dublet et al., 2015; Dublet et al., 2017; Cathelineau et al., 2017; Muñoz et al., 2019). These types of deposits commonly contain FeO/OHs, and several studies have discussed their enrichment in critical metals: Teitler et al. (2019) and Ulrich et al. (2019) have investigated the metal deportment (REEs, Sc, V, Co, Mn, Cr, Ni) within the FeO/OHs of New Caledonian laterites by combining mineralogical-geochemical analytical techniques (i.e., XRPD, Raman spectroscopy, SEM-EDS, EPMA-WDS, and LA-ICP-MS). Goethite is the main FeO/OH phase developed from the weathering of ultramafic protoliths, whereas goethite mixed with hematite commonly derives from weathering of gabbroid rocks (Teitler et al., 2019; Ulrich et al., 2019). Different goethite types, having different geochemistry and morphology, were observed at different depths in the laterite profile (Teitler et al., 2019). From the bottom of the laterite profile to its top, the following were observed: *i)* skeletal goethite replacing olivine and pyroxene at the bedrock-saprock transition zone; *ii)* epigenetic goethite, replacing primary and secondary serpentines in saprolite; *iii)* fine-grained goethite matrix cementing skeletal and epigenetic goethite fragments in *"yellow limonite"* and *"red limonite"*, whose color derives from fine-grained hematite formed through goethite dissolution; *iv)* euhedral goethite at the base of the ferricrete cap; *v)* zoned goethitic and hematitic pisoliths at the top of the profile.

The highest Ni grade was measured in skeletal and epigenetic goethite (avg. ~1 wt% Ni and ~0.7 wt%, respectively); Si mostly occurs within epigenetic goethite (avg. ~2 wt% Si), whereas major occurrences of Al and Cr are found in the goethite from the ferricrete zone (avg. ~2 wt% and ~4 wt% respectively). Scandium is mostly concentrated within *"yellow limonite"* goethites (up to 100 ppm). Further data on trace metals (Sc, V, Mn, Co, Ni) in the FeO/OHs of New Caledonia laterites are reported in Ulrich et al. (2019): Goethite containing ~11,000–42,800 ppm Cr, ~661–4652 ppm Mn, ~34–1860 ppm Co, ~1776–7082 ppm Ni, ~50–136 ppm Sc and ~200–500 ppm V; hematite containing ~6400–49,700 ppm Cr, ~468–6479 ppm Mn, ~61.4–1784 ppm Co, ~1752–6242 ppm Ni, ~30–76 ppm Sc and ~146–02 ppm V.

The Ni enrichment in New Caledonian goethites has been explained by the dissolution of Ni-bearing phyllosilicates and Ni capture in FeO/OHs (Beukes et al., 2000; Singh et al., 2002; Teitler et al., 2019). Manganese and Co may be incorporated in FeO/OHs located in the upper levels of the laterite by adsorption and/or replacement of Fe (Gerth, 1990; Singh et al., 2002), after the dissolution of unstable Mn oxides under low pH conditions (Ulrich et al., 2019). The REEs content in New Caledonian goethite is negligible (Ulrich et al., 2019), whereas Sc is relatively high. The LA-ICP-MS data show a contrasting Sc-enrichment in cumulate- and amphibolite-derived goethite: the cumulate-derived goethites have lower Sc (up to ~100 ppm), whereas Sc in amphibolite-derived goethites is significantly higher (up to ~800 ppm) (Teitler et al., 2019). Hematite is more abundant in the upper levels of gabbro-derived laterite; it forms at the expense of goethite after dehydration processes and contains low Sc (<50 ppm), as the majority of Sc formerly hosted within goethite is released during its dissolution and migrates in the lowermost section of the oxide zone (Teitler et al., 2019). These authors concluded that the chemistry of the parent rock mainly controls Sc enrichment in goethite, since goethites formed from peridotite contain low Sc mirroring the low Sc concentrations of primary olivine and enstatite, whereas goethites derived from the weathering of the amphibole-rich protoliths (i.e., amphibolites) contain higher Sc concentrations since amphibole contains elevated Sc. Goethite recrystallization and/or hematitization in the upper part of the oxide ore may also play an essential role in the final Sc enrichment in FeO/OHs since Sc is remobilized from the uppermost horizons of the laterite profile and migrates downward, where it is selectively captured by the earlier formed goethites in the lowermost laterite horizons (Ulrich et al., 2019). Ulrich et al. (2019) concluded that *"Sc concentrations within iron-(oxy)-hydroxides phases are high enough to be potentially exploited as a Ni-Co by-product"*.

2.1.1.2. Indonesia. Indonesia has become the world's largest Ni producer, accounting for the 26% of Ni global mine production (760,000 tons Ni, USGS, 2021), and has the world's largest published Ni ore reserves (21,000,000 tons Ni, USGS, 2021). Indonesian Ni(Co)-laterite deposits are derived from the chemical weathering of Cretaceous ophiolite-related ultramafic rocks (Ballantyne, 1991; Kadarusman et al., 2004) protoliths mainly consisting of lherzolite, harzburgite and minor dunite, pyroxenite, and gabbroic dikes (Fu et al., 2014). Studies of these laterite systems have focused on the deposits of Sulawesi Island (Golightly 1981; Golightly and Arancibia, 1979; Chen et al., 2004; Sufriadin et al., 2011; Ilyas and Koike, 2012; Fan and Gerson, 2013; Fu et al., 2014; Fu et al., 2018; Maulana et al., 2016; Farrokhpay et al., 2019). These deposits belong mostly to the hydrous Mg-silicate type, with local development of an overlying oxide zone. Summarising the literature, the main FeO/OHs consist of fine-grained goethite with minor hematite. Goethite in the saprolite hosts from 1.5 to 2.0% NiO on average (Farrokhpay et al., 2019). While these studies include information about Sc and REE contents in protoliths, further detailed information about minor and trace element behavior and content within FeO/OHs is lacking.

2.1.1.3. Philippines. The Philippines account for ~14% of global Ni mined with an annual production of 320,000 tons and has published Ni reserves of 4,800,000 tons, making it the world's second largest Ni producer (USGS, 2021). In the Philippines, laterites are formed on Cretaceous ultramafic rocks consisting of harzburgite, lherzolite, dunite, and gabbro (Dimalanta et al., 2020 and references therein). Several studies have revealed that Ni was hosted within goethites precipitated in the oxide horizons (i.e., Rio Tuba, Acoje, Pujada, Intex and Berong deposits, Santos-Ynigo, 1965; Morikawa, 1975; Ogura et al., 1983; Fan and Gerson, 2011; Tupaz et al., 2020a; Tupaz et al., 2020b). As in the case of Indonesia, details of the geochemistry of critical elements in FeO/OHs are scarce. Recent studies by Tupaz et al. (2020a) and Tupaz et al. (2020b) focused on the geochemical signatures of serpentine minerals of the bedrock and saprolite horizons of Intex (Mindoro Island) and Berong (Palawan Island) laterite deposits with EPMA data for goethite and hematite reporting Ni, Co, Cr, and Mn contents. Goethite and hematite samples at Berong host higher concentrations of useful trace metals when compared to Intex samples (Table 1). Remarkably, at Berong, Ni and Co contents of goethite are up to 1.71 wt% NiO and 0.65 wt% CoO vs. the 0.79 wt% NiO and 0.27 wt% CoO of Intex goethites. A similar trend was observed within hematite (up to 0.85 wt% NiO and 0.49 wt% CoO at Berong vs. the 0.41 wt% NiO and 0.16 wt% CoO at Intex).

2.1.2. Iron-(oxy)-hydroxides in the Caribbean Ni(Co)-laterite district

The Caribbean Islands also host significant Ni(Co)-laterite deposits accounting for 5,500,000 tons of Ni reserves (USGS, 2021). The most important deposits are located on Cuba (Pinares de Mayarí, Nicaro, Moa Bay and Punta Gorda, Linchenat and Shirakova, 1964; Lavaut, 1998)

and in the Dominican Republic (Falcondo and Loma Ortega, Haldemann et al., 1979; Villanova-de-Benavent et al., 2014; Tauler et al., 2017). Caribbean Ni(Co)-laterites formed through the weathering of Late Cretaceous to Paleocene/Eocene ophiolitic serpentinized peridotites (harzburgite) with subordinate dunite, lherzolite, and minor pyroxenite (Fonseca et al., 1985; Murashko and Lavandero, 1989; Lewis and Jiménez, 1991; Lewis et al., 2002; Lewis et al., 2006 ; Villanova-de-Benavent et al., 2014). The peridotites are locally cut by gabbro dikes, pegmatite gabbro, norite, and minor pyroxenite (Proenza et al., 1999a; Proenza et al., 1999b; Marchesi et al., 2006).

Both *"fresh"* and serpentinized peridotites have been exposed to weathering and erosion since the early Miocene (Linchenat and Shirakova, 1964; Haldemann et al., 1979; Lithgow, 1993; Lavaut, 1998; Iturralde-Vinent et al., 2006; Lewis et al., 2006; Villanova-de-Benavent et al., 2014). Based on mineralogy, Cuban Ni-laterites (i.e., Punta Gorda and Moa Bay) are classified as oxide-type deposits, while the Dominican Republic ores (i.e., Falcondo and Loma Ortega) are classified as hydrous Mg-silicate type deposits (Brand et al., 1998; Lewis et al., 2006; Proenza et al., 2007; Villanova-de-Benavent et al., 2014; Tauler et al., 2017).

The potential of Caribbean Ni(Co)-laterite deposits as unconventional sources of Sc, REEs, and PGEs was investigated by Aiglsperger et al. (2015) and Aiglsperger et al. (2016). Samples from different profile horizons of both Moa Bay (Cuba) and Falcondo (Dominican Republic) were analyzed using XRPD, SEM-EDS, EPMA-WDS, and LA-ICP-MS techniques. The results indicate that at Moa Bay, goethite is the main FeO/OH. Goethite is locally replaced by hematite in the uppermost horizons and by minor maghemite, which is more abundant in the lower portion of the oxide zone. At Falcondo, goethite dominates over hematite, with these phases forming the main FeO/OHs in the oxide zone. In these studies, Sc distribution relates to FeO/OH in the weathering profile at Moa Bay, whereas at Falcondo, REEs mostly occur as REE-bearing phosphate minerals, as Ce-accumulations in association with Mn-oxides or within the clay-zones of the laterite horizon (Aiglsperger et al., 2016). These studies also highlighted that PGEs are present within microscopic (~1–15 μm) chromian spinel inclusions or as secondary mineral inclusions within the saprolite and the upper part of the oxide zone.

2.1.3. Iron-(oxy)-hydroxides in the Australian Ni(Co)-laterite district

Ni(Co)-laterite deposits in Western Australia developed from the weathering of mafic and ultramafic intrusions belonging to Archean and Proterozoic greenstone belts and layered intrusions (Elias et al., 1981; Elias, 2006; Brand et al., 1996; Gaudin et al., 2005). The lithologies of the protoliths consist of gabbro, anorthosite, troctolite, pyroxenite, dunite, peridotite, and komatiite. The laterite deposits of Western Australia are classified either as clay-type (e.g., Murrin Murrin) or oxide-type (e.g., Wingellina) deposits.

Anand and Gilkes (1987) investigated the geochemistry of natural FeO/OHs in a number of laterite deposits of Western Australia. Their work described goethite, hematite, and maghemite properties within the duricrust and *"friable horizons"* of laterite profiles, developed on granite and dolerite protoliths and highlighted the occurrence of FeO/OHs with high levels of Al-substitution (16 to 33 mol% in goethite, 2.5 to 10 mol %, in hematite) and variably enriched in Ni, Co, Cr, V, Zn, Cu, and Mn. These studies show that metal deportment within the FeO/OHs is strongly dependent on parent rock chemistry. Further studies have been carried out on Ni(Co)-laterite deposits in Western Australia by Elias et al. (1981), Elias, (2006), Putzolu et al. (2018), Putzolu et al. (2019), Putzolu et al. (2020), and Santoro et al. (2021), and although some geochemical data on FeO/OHs were reported by the authors, FeO/OHs were not the focus of their studies (Table 1).

Laterites in eastern Australia developed during Tertiary time from weathering of an *'Alaskan-type'* ultramafic – mafic intrusive complex consisting of clynopyroxenites anomalously enriched in Sc (Johan et al., 1989). The latter are the parent rocks of the laterite deposits. The profile of the eastern Australia laterites consists of five horizons: *i)* a smectite-dominant saprolite horizon, *ii)* a transitional laterite, where smectite is progressively replaced by iron oxides and kaolinite, *iii)* an oxide zone, dominated by goethite and hematite, *iv)* a ferricrete, mostly consisting of hematite with less goethite, *v)* a transported reworked horizon. Chassé et al. (2017) and Chassé et al. (2019) analyzed goethite and hematite, showing that the highest Sc concentrations were detected in poorly crystalline Al-rich goethite (up to ~1500 ppm Al) and hematite (up to ~680 ppm Al) within the oxide zone. Sc enrichment is linked to: *i)* high Sc concentration in the parent rock, *ii)* long-lasting weathering in a stable tectonic environment, and *iii)* favorable weathering environment, allowing the Sc to be scavenged by the FeO/OHs.

2.1.4. Iron-(oxy)-hydroxides in the Mediterranean Ni(Co)-laterite district

The Ni(Co)-laterite deposits of the Balkan Peninsula and eastern Turkey are located within the Mirdita–Sub Pelagonian and Pelagonian tectonic zones (Eliopoulos et al., 2012) and include a number of deposits such as Lokris, Evia, Kastoria, Profitis Ilias, Tsouka, Vermio, Edessa, Olympus (Greece), Bitinke and Gouri (Albania), Rzanovo and Topola (Serbia), Gordes and Çaldağ (Turkey) (Eliopoulos and Economou-Eliopoulos, 2000; Eliopoulos et al., 2012; Thorne et al., 2009; Thorne et al., 2012).

The deposits of Albania and Greece formed from the weathering of Upper Jurassic–Lower Cretaceous serpentinized ophiolites, largely comprised of peridotites, local dunite, pyroxenite, and gabbro. The ophiolite suites have undergone a multistage alteration to form both autochthonous Ni(Co) and allochthonous Fe–Ni-laterites. The latter show FeO/OHs with elevated Al/Fe ratios and enrichment in PGEs. A good correlation between Al, Ti, REEs, Th, and U is also demonstrated (Salpeteur et al., 1995; Gray et al., 1996; Eliopoulos and Economou-Eliopoulos, 2000; Eliopoulos and Economou-Eliopoulos, 2010; Eliopoulos et al., 2012; Eliopoulos et al., 2014; Herrington et al. 2016).

Eliopoulos and Economou-Eliopoulos (2000) specifically investigated the REEs, PGEs, U, and Th content of minerals in both the autochthonous Ni(Co)-laterites and allochthonous Fe–Ni-bauxite-laterites in Greece using a range of analytical techniques. Their results indicate that: *i)* goethite > hematite are the most common minerals in the oxide zone, *ii)* goethite exhibits variable proportions of $Fe^{3+} \leftrightharpoons Al^{3+}$ substitutions and can accommodate Ni (up to ~1.5 wt% NiO), Cr (up to ~3 wt% Cr_2O_3) and Mn (up to ~2 wt% MnO), *iii)* REEs, U and Th behavior is similar and relates to conditions of low Eh and elevated organic complexes. They concluded that *"Pt mobility is higher than that of Pd, and that most Pt and a small proportion of Pd are associated with secondary Al-rich goethite"*. Another study carried out by Eliopoulos and Economou-Eliopoulos (2010) and Eliopoulos et al. (2012) highlighted that some Balkan and Turkish goethites incorporate elevated As (up to 6.9 wt% As_2O_3) as well as Ni, Cr, Mn, and As (Table 1). The remobilization and stability of As within goethite was considered dependent on the presence of organic matter, which enhanced the redox reactions and caused changes in pH of the weathering fluids, which resulted in an increase of the As-stability within goethite (Mamindy-Pajany et al., 2009). Using synchrotron X-ray methods, Gamaletsos et al. (2018) found that the As in such goethite occurs as arsenate anions (AsO_4^{3-}) adsorbed onto the mineral surface. Vind et al. (2018) looked at the occurrence of Sc within goethite and hematite associated with Greek bauxites and bauxite residues; in this study, the authors affirmed that the majority of Sc within bauxite is hosted by hematite through isomorph substitution of Sc^{3+} and Fe^{3+}, whereas goethite is believed to adsorb Sc on the crystal surfaces. Samouhos et al. (2019) conducted more specific studies by investigating the geochemistry and nano-mineralogy of FeO/OHs (mainly hematite-like) using TEM. The results showed that hematite occurs in: *i)* sub-micron flattened nanocrystals (particle size: 50–400 nm) or larger mineral aggregates (about 0.50 μm), *ii)* hematite hosts a series of trace elements as Ni (up to 1 wt%), Ca (<2 wt%), Ti (<2 wt%), Cr (<3 wt%) and Mn (<1 wt%), whose incorporation results in distortion in the crystal structure of hematite, *iii)* REE uptake by hematite was not investigated in detail but suspected.

Table 2
Location and bulk-rock mineralogy (XRPD) of the selected samples.

Deposit	Sample ID	Location in the profile	Mineralogy
Çaldağ	CN-03	high grade oxide zone	goethite
	CN-10080902	high grade oxide zone	goethite
Karaçam	KC-04	transition zone	goethite, smectite, quartz and Mn-oxy-hydroxide
	KC-09	high grade oxide zone	goethite, quartz and Mn-oxy-hydroxide
Wingellina	WPDD009-7	upper oxide zone	goethite, hematite and gibbsite.
	WPDD005-11	upper oxide zone	goethite, gibbsite, spinel and kaolinite
Piaui	CoG3-Pi-160413-16	oxide zone	goethite, hematite, chlorite, quartz and chromite

Previous studies of Turkish Ni-laterites at Çaldağ and Karaçam were mainly focused on the lateritization process and geochemical signatures of the associated weathering profiles (Andersen et al., 2009; Thorne et al., 2009; Herrington et al., in review) and, hence, were not specifically focused on unraveling individual FeO/OH phases.

2.1.5. *Other examples of iron-(oxy)-hydroxides from minor Ni(Co)-laterite districts*

Ni(Co)-laterites of Oman were derived from the weathering of Late Cretaceous ophiolites consisting of serpentinized peridotites and cumulate layered gabbros, diabase dikes, and basic pillow lavas (Glennie et al., 1973). Investigations carried out by Al-Khirbash (2015) and Al-Khirbash (2016) revealed low Ni and Co contents within hematite (up to ~1.4 wt% NiO, and ~0.5 wt% CoO, respectively); other minor elements hosted within hematite are Cr (up to ~5 wt% Cr_2O_3), Mn (up to ~1.9 wt% MnO), Al (up to ~5 wt% Al_2O_3). Goethite contains up to ~2 wt% NiO and ~0.6 wt% CoO as well as Cr (up to max ~3 wt% Cr_2O_3), Mn (up to ~1.7 wt% MnO), Al (up to ~8 wt% Al_2O_3) (Table 1). Both hematite and goethite contain minor TiO_2, CaO, and MgO (all <1 wt%). The higher Ni content in goethite compared to hematite is explained in terms of Ni loss during dehydration of goethite to form hematite.

Other studies have been carried out on deposits in Western Africa (Nahon et al., 1982 and reference therein; Yongue-Fouateu et al., 2006 and reference therein; Lambiv Dzemua and Gleeson, 2012; Lambiv Dzemua et al., 2013), Colombia (Gleeson et al., 2004; Tobón et al., 2020) and Brazil (Colin et al., 1990; Carvalho-e-Silva et al., 2003; Mano et al., 2014; Ratiè et al., 2015; Putzolu et al., 2021), however, in these papers there is only scant reference to the trace elements incorporation within FeO/OHs (Table 1).

3. Geological features of the studied laterite deposits

3.1. *Çaldağ Ni-laterite (Turkey)*

The Çaldağ Ni(Co)-laterite deposit is located within the Aegean region of Turkey, approximately 70 km to the East of Izmir (Fig. 1). The parent rock is a fragment of Tethys ophiolite suite obducted over Triassic dolomites (Önen and Hall, 2000; Herrington et al., 2016). The laterite deposit developed on variably serpentinized ultramafic bodies (dunite, lherzolite, harzburgite) and is cut by late calcite and magnesite veins (Thorne et al., 2009). The laterite profile at Çaldağ shows the typical features of an oxide-type deposit where fine-grained goethite, associated with minor asbolane and hematite, is the main ore phase in the oxide zone. Silicate-rich saprolite is rarely observed. The mining area consists of two main pits where the oxide zones have different features: in the northern pit, the oxide zone shows goethite veins with calcite and/or silica; the profile in the southern pit has a banded texture with variable amounts of Mn-(oxy)-hydroxides developed. The upper portion of the laterite profile displays a high degree of reworking where late calcite cemented oxide-rich blocks (Thorne et al., 2009). Therefore, the samples selected for this study were collected from the oxide zone of the northern pit to better represent the in-situ weathered profile.

3.2. *Karaçam Ni-laterite (Turkey)*

The Karaçam Ni(Co)-laterite deposit is located in Western Turkey (Fig. 1) and, as the Çaldağ deposit, is derived from the weathering of a Tethyan ophiolite fragment. The local parent rock consists of a serpentinized cumulate peridotite (harzburgite and lherzolite). Previous studies (Herrington et al., in review) report that Ni and Co are hosted in goethite that is commonly associated with asbolane within the oxide zone of the lateritic profile. The Karaçam ore is oxide-dominated, similarly to Çaldağ, but it has a well-defined clay-rich saprolite zone in contrast to the latter. The oxide zone consists of massive fine-grained material associated with Mn-(oxy)-hydroxides, whereas the saprolite is rich in Ni-bearing phyllosilicates with the presence of the hydrotalcite phase, takovite, along with patchy goethite (Herrington et al., in review). Two samples were collected from the high-grade oxide zone and analyzed in this study.

3.3. *Piauí Ni-(Co)laterite (Brazil)*

The Piauí Ni(Co)-laterite deposit is located in North-eastern Brazil (Fig. 1). The laterite profile formed through the alteration of a Neoproterozoic layered mafic–ultramafic complex. The parental rocks consist of serpentinized dunite, with olivine-gabbros and diorites. The weathering profile comprises several zones, which from the bottom to top are: *i)* the saprock, where the ferromagnesian magmatic minerals are almost totally serpentinized and altered into FeO/OHs and smectite clays; *ii)* the saprolite zone, which is silicified with silica in a vein network at the lowermost portion of the unit, whereas top zone the saprolite is more clay-rich; *iii)* an argillaceous oxide zone, where the main FeO/OH is hematite; *iv)* a silica-rich unit (i.e., silcrete) (Krüger et al., 2017; Krüger, 2019). The samples used for the present study were collected from the oxide zone.

3.4. *Wingellina Ni(Co)-laterite (Western Australia)*

The Wingellina Ni(Co)-laterite deposit is located in Western Australia (Fig. 1) and formed from the weathering of the Mesoproterozoic mafic to ultramafic layered-intrusions of the Giles Complex (Putzolu et al., 2018). The mafic parent rocks of the laterite consist of gabbro/gabbronorite units and serpentinized ultramafic lithologies (i.e., peridotites and dunites, with minor pyroxenite). The Wingellina weathering profile comprises from bottom to top: *i)* phyllosilicate-rich saprolite; *ii)* a Fe- and Mn-(oxy)-hydroxide-rich oxide zone, where the main FeO/OH is goethite commonly associated with lithiophorite-asbolane intermediates; *iii)* a calcrete-silcrete duricrust, consisting of partly silicified nodular and massive carbonates (Putzolu et al., 2018). Two selected samples were collected for analysis from the oxide zone of Wingellina laterite.

4. Analytical methods

Seven FeO/OHs-rich specimens were selected for analysis (Table 2), collected from the oxide zones of the Ni(Co)-laterite deposits described above. Specimens were selected from collections held at the Natural History Museum (NHM) of London (UK) and the Dipartimento di Scienze della Terra, dell'Ambiente e delle Risorse (DiSTAR) of the University of Napoli Federico II (Italy), based on characteristics revealed by previous studies (Thorne et al., 2009; Norman, 2014; Putzolu et al., 2018).

All samples were analyzed by wet chemical analysis of bulk rock using Inductively Coupled Plasma Mass Spectrometry (ICP-MS) and Inductively Coupled Plasma Atomic Emission Spectrometry (ICP-AES).

Table 3
Secondary standards used for LA-ICP-MS analysis.

	NIST 610			BC_28		
	(standard)	(average)*	standard deviation	(standard)	(average)*	standard deviation
^{24}Mg	432.00	404.04	13.98	11,618.00	11,827.79	104.89
^{27}Al	10,320.00	8724.39	797.81	20,787.00	20,499.50	143.75
^{45}Sc	455.00	401.41	26.80	31.00	25.51	2.74
^{47}Ti	452.00	389.25	31.37	87,615.00	74,962.25	6326.38
^{51}V	450.00	397.89	26.06	9603.00	9402.17	100.41
^{53}Cr	408.00	354.65	26.67	1172.00	1292.75	60.37
^{55}Mn	444.00	391.25	26.37	2125.00	1998.96	63.02
^{59}Co	410.00	350.79	29.61	241.00	292.44	25.72
^{60}Ni	458.70	387.84	35.43	573.00	574.35	0.68
^{66}Zn	460.00	384.08	37.96	588.00	439.89	74.06
^{69}Ga	433.00	366.61	33.20	41.10	48.24	3.57
^{74}Ge	433.00	306.01	63.50	0.86	0.71	0.07
^{89}Y	462.00	416.45	22.78	–	–	
^{139}La	440.00	393.22	23.39	–	–	
^{140}Ce	453.00	403.56	24.72	–	–	
^{141}Pr	448.00	397.76	25.12	–	–	
^{146}Nd	453.00	379.45	36.77	–	–	
^{147}Sm	430.00	396.43	16.78	–	–	
^{153}Eu	447.00	401.32	22.84	–	–	
^{157}Gd	449.00	401.36	23.82	–	–	
^{159}Tb	437.00	391.88	22.56	–	–	
^{163}Dy	437.00	373.93	31.53	–	–	
^{165}Ho	449.00	401.71	23.65	–	–	
^{166}Er	455.00	393.62	30.69	–	–	
^{169}Tm	435.00	387.21	23.90	–	–	
^{172}Yb	450.00	395.86	27.07	–	–	
^{175}Lu	439.00	397.08	20.96	–	–	
^{208}Pb	426.00	380.35	22.82	–	–	

* the average values are calculated from the results of LA-ICP-MS; - n.d.

Further analyses were performed via X-ray Powder Diffraction (XRPD), Scanning Electron Microscopy equipped with Energy Dispersive Spectroscopy (SEM-EDS), Electron Microprobe Analyses (EMPA) in Wavelength Dispersive Spectroscopy (WDS), Field Emission Gun Scanning Electron Microscopy (FEG-SEM), Laser-Ablation Inductively Coupled Plasma Mass Spectrometry (LA-ICP-MS) and Scanning Transmission Electron Microscopy (STEM).

Wet chemical analyses of major, minor and trace elements were carried out at ALS Minerals, OMAC Laboratories Ltd (Co Galway, Ireland). About 4 g of material was powdered and analyzed by multi-element ICP-MS for REEs and trace elements (Ba, Ce, Cr, Cs, Dy, Er, Eu, Ga, Hf, Ho, La, Lu, Nb, Nd, Pr, Rb, Sm, Sn, Sr, Ta, Tb, Th, Tm, U, V, W, Y, Yb, Zr) and by multi-element ICP-AES for SiO_2, Al_2O_3, Fe_2O_3, CaO, MgO, Na_2O, K_2O, Cr_2O_3, TiO_2, MnO, P_2O_5, SrO, BaO, following fused acid digestion. Base metals (Ag, As, Cd, Co, Cu, Li, Mo, Ni, Pb, Sc, Tl, Zn, Co, Ni, Pb, Zn) were analyzed by ICP-AES, following four acids digestion.

X-ray powder diffraction analyses were conducted at the NHM with a Panalytical ExPert Pro MPD automated diffractometer using CoKα radiation operating at 45 kV, 40 mA, with a step scan size of 0.02° 2θ. The mineral identification was performed with the HighScore Plus software package.

SEM-EDS analyses were carried out by using a ZEISS EVO LS 15 scanning electron microscope (NHM) at 20 kV, with 8.5 mm working distance and 3nA current equipped with X-Max detectors. Microprobe (EPMA) quantitative data sets were acquired by wavelength dispersion spectrometry (WDS), using a Cameca SX100 electron microprobe operating at 20 kV, 20nA, and 10 μm spot size (NHM).

High-resolution elemental maps were created using a FEI Quanta 650 FEG SEM at the NHM. The instrument is equipped with a Bruker Flat Quad 5060F energy dispersive X-Ray detector (EDS) for hyperspectral mapping. Maps were acquired at HV mode, and the instrument was operated at 15 Kv, with 28 mm working distance and 8 μm pixel size. For Co, the image resolution scale was adjusted to show its occurrence in FeO/OHs; quantitative values were then assessed by in situ EPMA.

The TEM-HRTEM analyses were performed using a FEI Titan Themis 200 (TEM/STEM) at the University of St. Andrews (Scotland, UK). The instrument was equipped with an X-FEG Schottky field emission gun providing high current, spatial and temporal coherence, and brightness. The incorporation of a spherical aberration corrector allows STEM images with an 80 pm resolution and TEM 0.240 nm resolution. The instrument was also equipped with Super-X high sensitivity windowless EDX detector. The analyses were run in High-Angle-Annular-Dark-Field scanning transmission electron microscopy (HAADF-STEM) and High-Resolution TEM (HRTEM). Single EDX analyses and elemental maps were carried out in selected areas using 30 s dwell time. The instrument operated at 300Kv and with a point-to-point resolution of 0.08 nm resolution. HRTEM images and Selected Area Electron Diffraction (SAED) patterns were calibrated and processed by software package Gatan Digital Micrograph, which allowed the automatic conversion of rings radius in *d*-spacing and hence the mineral identification.

The trace element composition of the FeO/OHs was assessed using LA-ICP-MS at the NHM; the data were collected through an Agilent 7700 × quadrupole ICP-MS coupled to a 193 nm ESI NWR ArF excimer laser. The output energy of the laser was typically 3.5 J cm^{-2} and used a 10 Hz pulse repetition rate with a crater size of 35 or 50 μm. Routine measurements of the GSD-1 g synthetic basaltic glass (three every 30 unknown analyses) were used as external standards to correct instrumental drifting. Dwell times for each element ranged from 5 to 20 ms and peak-hopping was employed. Oxide generation was optimized at $ThO^+/Th^+ = <0.18$ %. For each analysis, a baseline was measured for 35 s prior to 55 s of ablation. The absolute element concentrations were calculated by ExLAM (Zachariáš and Wilkinson, 2007), using the Fe concentration predetermined by SEM-EDS as internal standard and GSD-1 g as the primary reference material. The accuracy of the measurements was monitored by comparing the major element concentrations calculated by LA-ICP-MS with the data from SEM-EDS and repeated analyses of secondary standards (NIST 610, BC 28, Table 3).

The trace element geochemical data (i.e., LA-ICP-MS) were treated using multivariate statistical analysis to assess the potential chemical

Table 4
Major (wt%), minor and trace (ppm) element concentrations.

Deposit		Çaldag		Karaçam		Piaui	Wingellina	
Sample ID		CN-03	CN-10080902	KC-04	KC-09	COG3-PI-160413-16	WPDD005-11	WPDD009-7
wt%	dl							
SiO_2	0.01	3.46	5.44	19.90	22.00	9.66	4.96	2.50
Al_2O_3	0.01	0.98	0.68	0.04	1.49	5.92	20.00	24.70
Fe_2O_3	0.01	75.10	76.00	64.70	55.60	57.70	47.40	48.10
CaO	0.01	0.05	0.02	0.13	0.18	<0.01	0.05	0.04
MgO	0.01	0.11	0.09	2.68	0.31	6.10	0.99	0.56
Na_2O	0.01	<0.01	<0.01	0.01	<0.01	<0.01	0.03	0.03
K_2O	0.01	<0.01	<0.01	<0.01	<0.01	<0.01	<0.01	<0.01
Cr_2O_3	0.01	1.78	3.02	0.29	0.89	4.51	2.97	0.79
TiO_2	0.01	0.01	0.01	<0.01	<0.01	0.10	0.49	0.45
MnO	0.01	0.02	0.01	2.05	0.31	0.73	0.78	1.08
P_2O_5	0.01	0.02	0.01	0.03	<0.01	0.04	0.02	<0.01
SrO	0.01	<0.01	<0.01	<0.01	<0.01	<0.01	<0.01	<0.01
BaO	0.01	<0.01	<0.01	0.01	<0.01	0.02	<0.01	<0.01
LOI		16.60	13.10	7.50	15.55	9.57	20.80	20.90
Total		98.13	98.38	97.34	96.33	94.35	98.49	99.15
wt%								
Ni	1.00	0.13	0.11	2.27	2.26	2.11	0.84	0.52
Co	0.00	0.01	0.00	0.22	0.10	0.08	0.04	0.07
Pb	0.00	<0.0002	<0.0002	<0.0002	<0.0002	<0.0002	0.00	<0.0002
Zn	0.00	0.01	0.01	0.01	0.03	0.04	0.08	0.01
ppm								
Ag	0.50	<0.5	<0.5	<0.5	<0.5	<0.5	<0.5	<0.5
As	5.00	44.00	318.00	293.00	901.00	7.00	<5	<5
Cd	0.50	<0.5	<0.5	0.70	0.70	0.80	<0.5	<0.5
Cu	1.00	263.00	215.00	4.00	3.00	1190.00	51.00	84.00
Li	10.00	<10	<10	<10	<10	<10	<10	<10
Mo	1.00	<1	<1	1.00	1.00	2.00	<1	1.00
Tl	10.00	10.00	<10	<10	<10	<10	10.00	<10
Ga	0.10	2.60	4.30	2.00	1.00	11.50	28.70	16.90
U	0.05	3.14	2.03	2.72	2.27	0.24	0.05	0.05
V	5.00	300.00	255.00	5.00	27.00	195.00	277.00	243.00
Zr	2.00	2.00	2.00	<2	<2	2.00	7.00	11.00
W	1.00	1.00	1.00	1.00	8.00	1.00	<1	1.00
Nb	0.20	<0.2	<0.2	<0.2	0.20	<0.2	0.30	0.40
Rb	0.20	1.10	0.50	2.80	0.60	0.50	0.20	<0.2
Sn	1.00	1.00	1.00	1.00	1.00	<1	1.00	1.00
Sr	0.10	3.60	2.30	18.90	20.40	3.50	8.70	19.60
Cs	0.01	0.22	0.25	11.00	0.77	0.10	<0.01	0.01
Hf	0.20	<0.2	<0.2	<0.2	<0.2	<0.2	0.30	0.50
Ta	0.10	<0.1	<0.1	<0.1	0.20	<0.1	0.10	0.10
Th	0.05	0.30	0.11	0.09	<0.05	0.08	0.07	0.09
Sc	1.00	33.00	13.00	2.00	9.00	27.00	30.00	34.00
La	0.10	1.80	0.60	0.60	0.70	0.40	3.90	1.80
Ce	0.10	1.00	0.40	0.60	1.30	0.60	4.90	4.40
Pr	0.03	0.47	0.07	0.08	0.15	0.09	0.92	0.44
Nd	0.10	1.80	0.20	0.30	0.80	0.50	4.90	2.00
Y	0.10	1.70	0.30	2.30	9.40	3.30	5.50	3.50
Tb	0.01	0.06	<0.01	0.02	0.12	0.03	0.24	0.16
Sm	0.03	0.44	<0.03	0.09	0.22	0.06	1.33	0.59
Dy	0.05	0.44	0.06	0.15	0.89	0.18	1.23	0.95
Eu	0.03	0.11	<0.03	0.03	0.11	0.05	0.51	0.27
Gd	0.05	0.42	<0.05	0.17	0.68	0.16	1.14	0.83
Ho	0.01	0.07	0.01	0.04	0.22	0.07	0.24	0.17
Lu	0.01	0.03	0.01	0.01	0.10	0.06	0.10	0.07
Tm	0.01	0.05	0.02	0.03	0.12	0.05	0.16	0.10
Er	0.03	0.19	<0.03	0.14	0.70	0.27	0.58	0.48
Yb	0.03	0.26	0.04	0.08	0.60	0.29	0.97	0.43
ΣREE	0.69	8.84	1.71	4.64	16.11	6.11	26.62	16.19

differences between the considered FeO/OHs. The variance was studied by using Principal Component Analysis (PCA), Multivariate Analysis of Variance (MANOVA test), and a post hoc Tukey's test, performed through the R software (v 3.6.1). The PCA was carried out through the *princomp* and *ggbiplot* packages using 11 variables for 92 LA-ICP-MS analyses. The above-described proportions between variables (chosen elements) and observations (point analyses) comply with the numerical criteria applied to ensure stable results during PCA (i.e., $n > p2 + 3p + 1$, where n is the number of observations and p is the number of variables) (Reimann et al., 2011). Prior to PCA, the elements were selected based on their variance and significance in mineralized laterite systems. The element concentrations were then normalized using the isometric log-ratio transformation. As the latter conversion is based on a matrix with no zero data, the concentration values below the detection limits (dl) have been represented by a value of 65 % of the dl value (Martín-Fernández et al., 2003). For the interpretation of the outcomes of PCA,

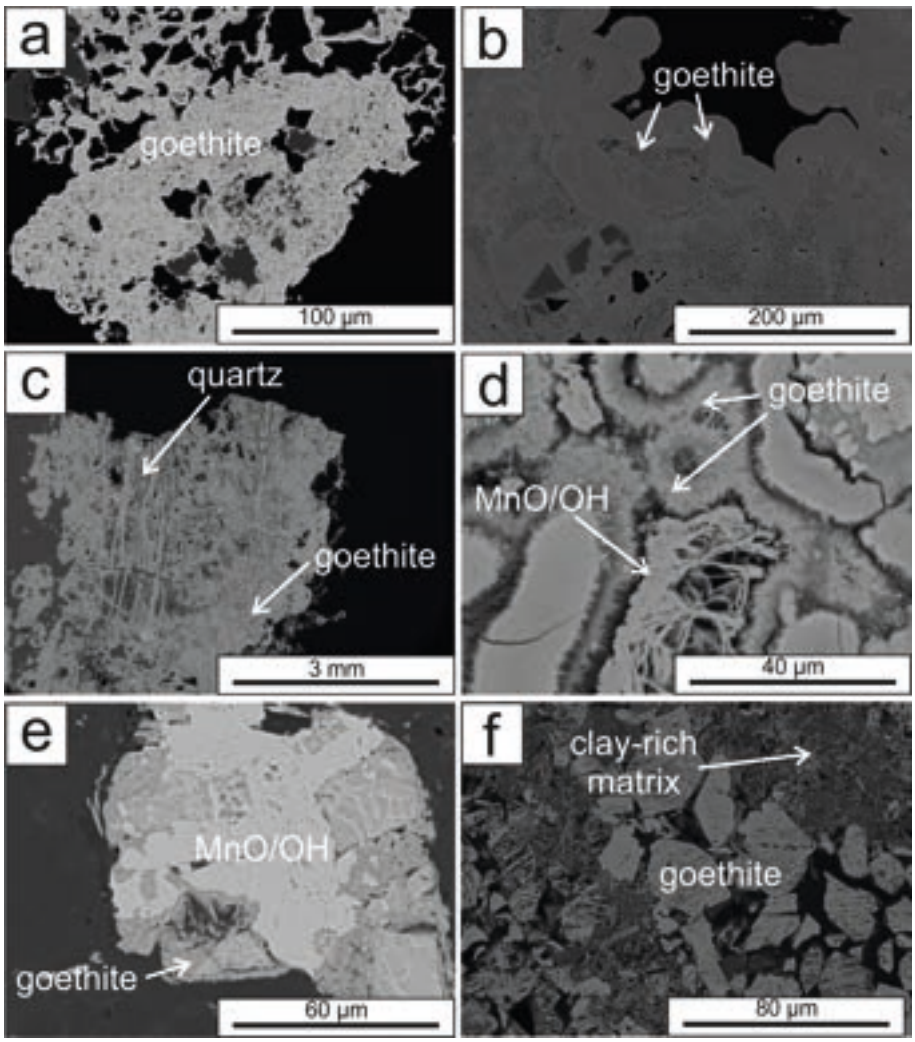

Fig. 2. Backscattered electron (BSE) photomicrographs of iron-(oxy)-hydroxides: a) goethite crust filling voids (Çaldağ); b) colloform goethite (Çaldağ); c) skeletal goethite aggregate coating quartz (Karaçam); d) fibrous goethite and Mn-(oxy)-hydroxide (Karaçam); e) cryptocrystalline intergrowth of goethite and Mn-(oxy)-hydroxide (Piaui); f) skeletal goethite enveloped in a clay-rich matrix (Wingellina).

we relied only on components explaining at least 10% of the variance of the dataset. The MANOVA test was also carried out to assess the reliability of the clusters defined by PCA in discriminating the chemically contrasting FeO/OH species. During the MANOVA test, only PC axes, explaining at least 95% of the dataset's total variance, were used. A multivariate multiple linear regression was also conducted between the same PC axes (dependent variables) and the groups previously identified and encoded as dummy independent variables to feed the post hoc Tukey's test and evaluate the pairwise differences between groups o determine the group clusters statistically.

5. Results

5.1. Wet chemical whole-rock geochemistry

From bulk-rock geochemistry (Table 4), Fe is the dominant element in the analyzed suite of samples, with Fe_2O_3 values > 45 wt%. SiO_2 shows concentrations between ~2 wt% and 10 wt% in the Wingellina, Piauí, and Çaldag samples, whereas Si values above 20 wt% were recorded in the Karaçam samples. The Wingellina and Piauí oxide samples have a high Al content (up to ~24 wt% Al_2O_3 and ~6 wt% Al_2O_3, respectively), while in Turkish specimens, Al rarely exceeds 1 wt %. Magnesium is generally <5% MgO, except in the sample from Piauí. The overall MnO content is low: <0.5 wt% at Çaldag and ranges between ~0.3 wt% and ~2 wt% in the other deposits, with the highest concentrations observed in the Wingellina and Karaçam samples. Chromium oxide is variable, with values ranging between <0.5 wt% and ~5 wt% Cr_2O_3. Among the selected deposits, Ni shows high values in Karaçam and Piauí samples (>2 wt% Ni), while is less enriched at Wingellina (0.5 wt% < Ni < 1 wt%) and Çaldag (<0.5 wt% Ni). The highest Co contents have been measured in the Karaçam specimens (up to 0.22 wt% Co), while the Wingellina and Piauí samples show intermediate Co grades (0.4 wt% to 0.08 wt% Co). The Co grade hardly reaches the 0.01 wt% Co at Çaldag.

5.2. Mineralogy, textures, and chemistry of iron-(oxy)-hydroxides

X-ray powder diffraction analyses (Table 2 and Appendix A) have shown that goethite is the dominant FeO/OH phase in all the selected samples, with minor hematite observed in the samples from Wingellina

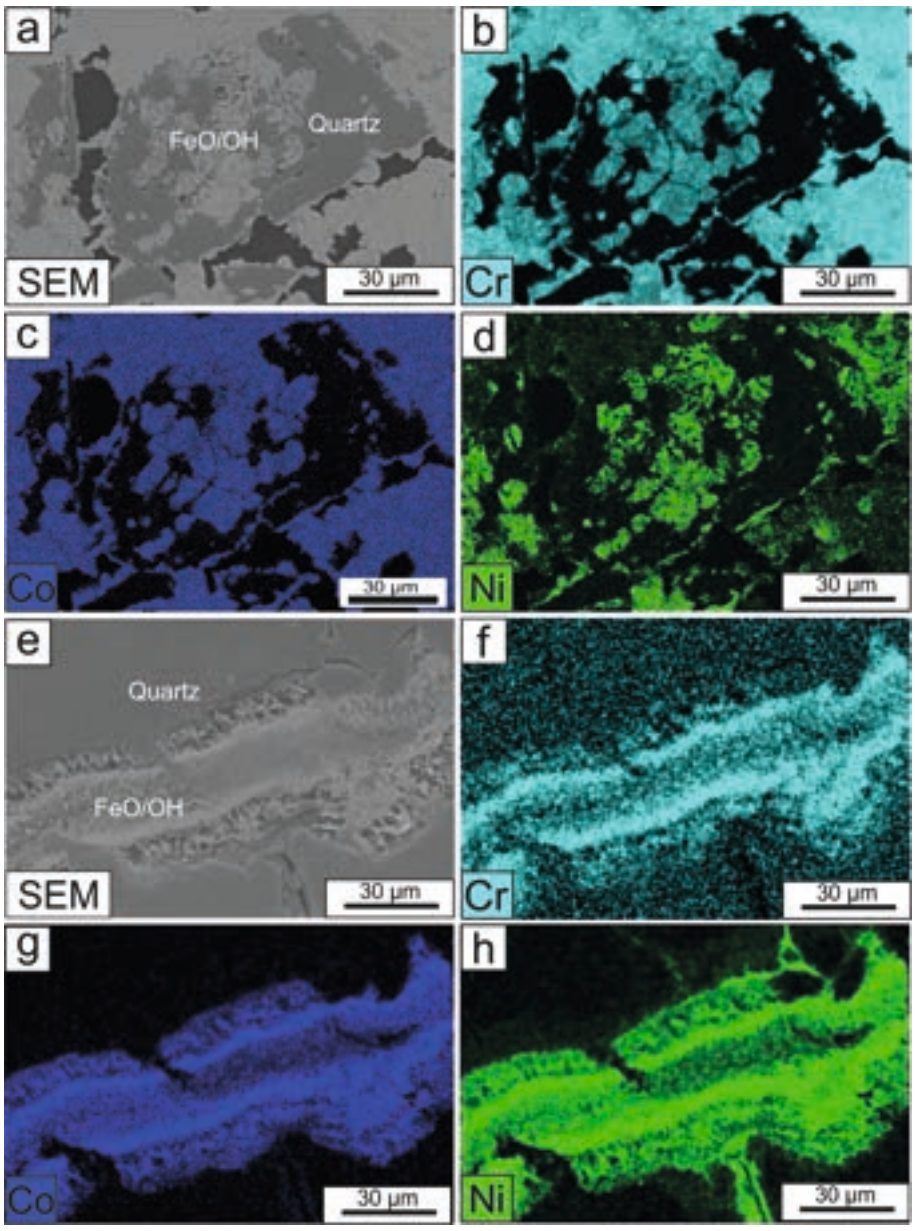

Fig. 3. High-resolution elemental maps of iron-(oxy)-hydroxides: a) to d) BSE image and Cr, Co, Ni maps of iron-(oxy)-hydroxides from the Çaldağ deposit (sample CN-03); e) to h) BSE image and Cr, Co, Ni maps of iron-(oxy)-hydroxides from the Karaçam deposit (sample KC-04).

and Piauí. The textures of FeO/OHs are shown in Fig. 2a to f, the high-resolution qualitative elemental mapping in Fig. 3a–h, and their compositions by EMPA are listed in Table 5.

Iron-(oxy)-hydroxides at Çaldağ occur in two generations, as porous goethite crusts (Fig. 2a) and as colloform goethite concretions filling cavities (Fig. 2b). The FeO_t in Çaldağ FeO/OHs reaches ~85 wt%, averaging ~79 wt%. The FeO/OHs show high Cr_2O_3 concentrations (up to ~3 wt%) with Cr variability (from ~1 to ~3 wt% Cr_2O_3) shown in distinct bands in the concretionary goethite. Silicon is ubiquitous and has concentrations ranging between ~1 wt% and ~3 wt% SiO_2. Goethite crusts have high NiO and CoO concentrations (Fig. 3): NiO can be up to ~2 wt%, while CoO is <0.1 wt% on average (Fig. 3 and Table 5). The concretionary goethites have NiO values < 0.5 wt%, while CoO is negligible. Other elements, as Mn, Al, and Mg also occur only in trace amounts.

At Karaçam, goethite is the only FeO/OH phase detected through XRPD. It shows a skeletal texture and is intergrown with quartz (Fig. 2c and Fig. 3e–h), or it occurs in fibrous aggregates associated with Mn-(oxy)-hydroxides (Fig. 2d). Goethite from Karaçam is slightly depleted in Fe (max. concentration ~77 wt% FeO_t), probably due to the higher amounts of Ni and Si (avg. values ~4.7 wt% NiO and ~9 wt% SiO_2). The Co grade at Karaçam is commonly <0.2 wt% CoO.

Piauí goethite forms concretions associated with Mn-(oxy)-hydroxides (Fig. 2e). The FeO_t content is ~78 wt% on average. On average, the Ni grade is ~3 wt% NiO, while Co displays lower values (avg. ~0.3 wt% CoO). Silicon and Mg are also present in significant amounts (~3 wt%

Table 5
Representative compositions and structural formulasof Fe-(oxy)-hydroxides from laterite deposits.

	Çaldağ				Karaçam				Wingellina			Piaui	
	CN_03		CN_10080902		KC_04		KC_09		WPDD009-7	WPDD005-11		COG3_PI	
Al_2O_3	0.42	0.43	0.62	0.23	–	–	1.60	2.07	5.85	5.98	5.83	–	0.72
MgO	0.61	0.27	0.03	0.03	0.62	0.51	0.30	0.23	1.97	0.76	0.57	1.07	5.44
SiO_2	3.16	2.42	1.99	1.99	9.65	11.37	8.03	7.80	3.64	3.96	4.31	2.06	3.89
CaO	0.11	0.07	0.02	0.02	0.28	0.21	0.10	0.13	–	–	–	–	–
TiO_2	–	–	–	–	–	–	–	–	0.28	1.08	1.86	0.14	0.02
MnO	0.19	0.59	–	–	0.08	0.04	0.16	0.09	0.38	0.66	0.75	0.75	0.24
FeO_t	82.47	80.06	81.68	84.21	72.97	70.55	76.79	72.98	72.64	73.09	72.85	82.23	76.93
CoO	0.03	0.16			0.06	0.04	0.10	0.06	0.03	0.01	0.02	0.17	
NiO	1.52	2.71	0.11	0.06	4.73	5.28	3.44	3.21	0.41	2.46	2.77	1.71	1.30
Cr_2O_3	1.33	1.50	3.10	1.43	0.05	0.05	0.10	1.48	0.24	0.77	0.64	0.51	0.23
Total	89.97	88.43	87.99	88.41	88.50	88.09	90.73	88.08	85.41	88.76	89.58	88.76	89.07
on the basis of $Fe^{3+}O(OH)$													
Al	0.01	0.01	0.01	–	–	–	0.03	0.03	0.10	0.10	0.09	–	0.01
Mg	0.01	0.01	–	–	0.01	0.01	0.01	–	0.04	0.02	0.01	0.02	0.12
Si	0.05	0.04	0.03	0.03	0.14	0.16	0.11	0.11	0.05	0.06	0.06	0.03	0.06
Ca	–	–	–	–	0.00	0.00	–	–	–	–	–	–	–
Ti	–	–	–	–	–	–	–	–	–	0.01	0.02	–	–
Mn*	–	–	–	–	–	–	–	–	–	0.01	0.01	0.01	
Fe	0.89	0.89	0.91	0.94	0.77	0.74	0.79	0.77	0.79	0.77	0.76	0.91	0.82
Co*	–	–	–	–	–	–		–	–	–	–	–	–
Ni	0.02	0.03	–	–	0.05	0.06	0.04	0.04	–	0.03	0.03	0.02	0.01
Cr	0.02	0.02	0.04	0.02	–	–		0.02	–	0.01	0.01	0.01	–
Total	1.00	1.00	0.99	0.99	0.98	0.97	0.98	0.98	1.00	0.99	0.99	1.00	1.02

atoms per formula unit (apfu) on the basis of $Fe^{3+}O(OH)$; * = calculated on the basis of Mn^{3+} and Co^{3+}; – = below detection limit.

SiO_2 and ~5 wt% MgO respectively).

In the Wingellina samples, goethite has a skeletal texture (Fig. 2f). The FeO_t is up to ~67 wt%. Aluminum is a common impurity (up to ~8 wt% Al_2O_3). The NiO content is always < 2 wt%, and the Co grade is negligible.

5.3. Nanoscale mineralogical and chemical features of iron-(oxy)-hydroxides

The HAADF-STEM and HRTEM analyses were carried out only on the Çaldağ and Karaçam specimens. This analytical choice was driven by the following considerations derived from previous analyses: *i)* the occurrence of the only goethite as the main FeO/OHs phase (observed in the XRPD analyses); *ii)* the high Ni, Co, Mn, and Cr contents within goethite (detected by EMPA); *iii)* the high Si content that could alternatively be ascribed to the occurrence of other FeO/OH phases (i.e., ferrihydrite) that are difficult to detect using XRPD.

Under HAADF-STEM, the Çaldağ FeO/OHs show a crystalline and platy texture consisting of randomly oriented crystals of several hundred nm in length (Fig. 4a); these are closely intergrown and commonly overlap each other (Fig. 4b and c). The images fail to reveal goethite intergrown with other crystalline phases (i.e., Cr, Si, Mn minerals), nor do they reveal the presence of any mineral inclusions. The EDX maps (Fig. 4d) and the EDX in situ analyses (Fig. 4e) confirm the EMPA analyses because significant concentrations of Cr, Ni, Si, Co, Al, and Mn were also detected. No clustering of elements was observed in the EDX maps, thus confirming the absence of mineral inclusions that could account for the high content of trace elements in FeO/OHs.

The atomic packing and the inter-atomic distances of FeO/OHs were assessed through HRTEM (Fig. 4f and g) and SAED (Fig. 4h). The latter shows the typical annular-shaped pattern of polycrystalline materials with a random orientation of crystallites. The conversion of the radius of the SAED patterns for each ring in *d*-spacing values resulted in a good match with the diffractometric features of goethite from literature (Gualtieri and Venturelli, 1999, Table 6); this would appear to exclude the occurrence of nanometric ferrihydrite.

In the Karaçam samples, FeO/OHs form needle-shaped nanocrystals (<100 nm) growing in voids (Fig. 5a–c). The EDX analyses (Fig. 5d) show both significant Si and Ni enrichments, while Cr, Co, and Mn are very low compared to the Çaldağ values, in agreement with EMPA analyses. EDX maps were acquired on the Fe-(oxy)-hydroxides/quartz border (Fig. 5e); this resulted in detecting two chemical domains: the Si-domain, which is indicative of quartz, while the Fe-domain represents the FeO/OHs-rich area. In this frame, Co and Ni concentrate within the Fe-domain, whereas Mn is exceptionally low, which constrain their deportment within FeO/OH rather than in Mn-(oxy)-hydroxides. Furthermore, no particular metal clustering was observed, which confirms the absence of other mineral intergrowths and/or inclusions with/within FeO/OHs (Fig. 5f). HRTEM image analyses showed inter-atomic distances matching those of goethite (Fig. 5f), while the SAED patterns showed the presence of single crystalline phases mixed with polycrystalline materials (Fig. 5g). The results match well with goethite data from the literature (Table 6), which would appear to exclude the presence of ferrihydrite intergrown with the Karaçam goethite.

5.4. Trace elements geochemistry of iron-(oxy)-hydroxides

Laser Ablation-ICP-MS analyses (Figs. 6 and 7, Appendix B and Appendix C) have shown that FeO/OHs from the selected deposits host a wide range of trace elements. At Çaldağ, FeO/OHs have high Cr and V, ranging between 8218–29,842 ppm and 55–508 ppm, respectively. Conspicuous amounts of Mn, Co, Ni, Mg, Ti, and Zn (avg. values = 1087 ppm Mn, 368 ppm Co, 6472 ppm Ni, 926 ppm Mg, 42 ppm Ti and 119 ppm Zn) were also detected. The Sc and Si concentrations are lower than those seen in FeO/OHs from the other deposits (avg. values = 12 ppm Sc and 9684 ppm Si). Iron-(oxy)-hydroxides from Karaçam have relatively high concentrations of Al, Si, Ni, Zn, and Co (6919–54,310 ppm Al, 29,736–265,148 ppm Si, 18,580–31,033 ppm Ni, 174–330 ppm Zn and 697–1235 ppm Co), and show a depletion in Sc, V and Ti (avg. values = 20 ppm Sc, 14 ppm V and 2 ppm Ti). Chromium, Mn, and Mg amount to

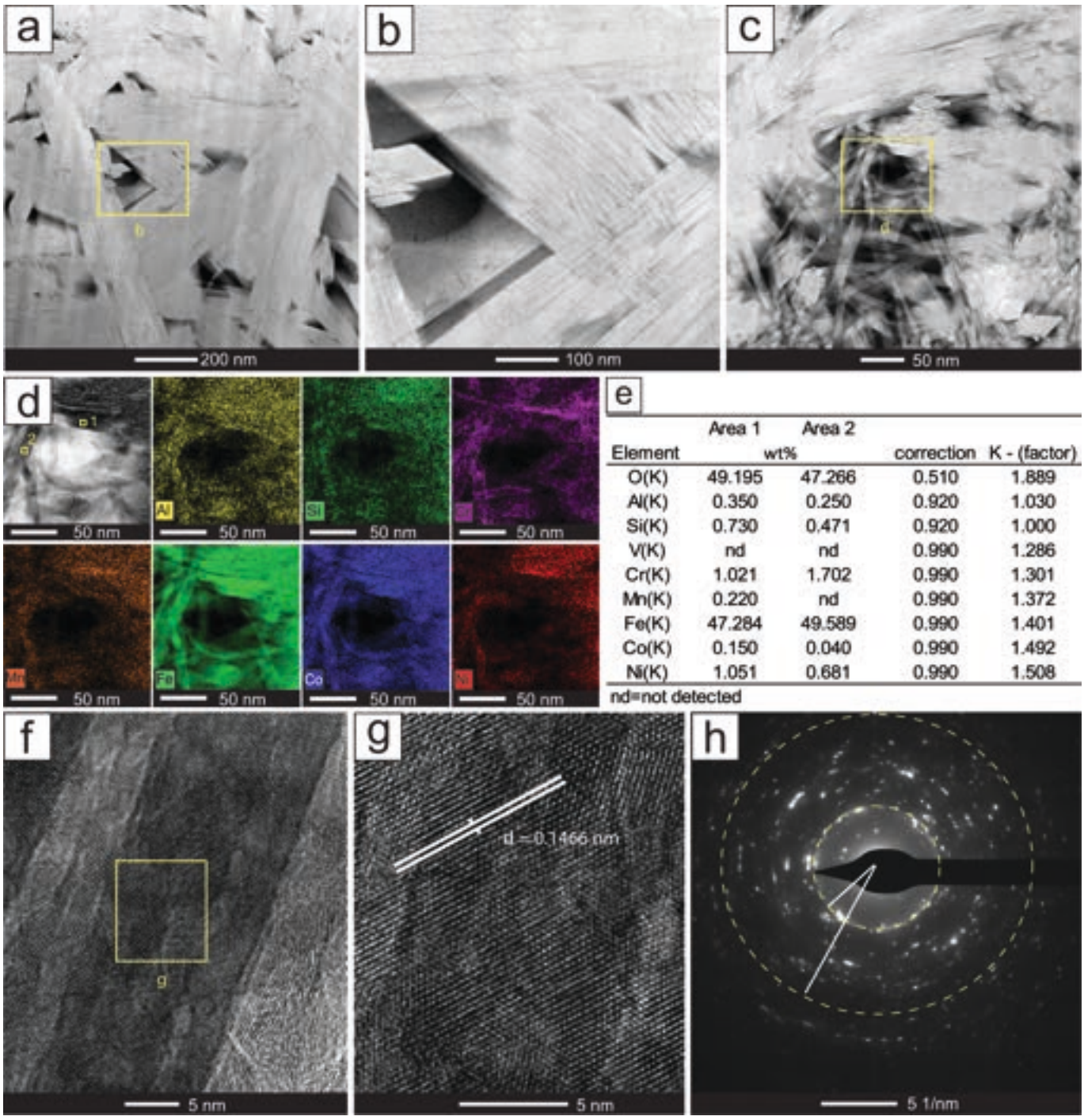

Element	Area 1 wt%	Area 2 wt%	correction	K - (factor)
O(K)	49.195	47.266	0.510	1.889
Al(K)	0.350	0.250	0.920	1.030
Si(K)	0.730	0.471	0.920	1.000
V(K)	nd	nd	0.990	1.286
Cr(K)	1.021	1.702	0.990	1.301
Mn(K)	0.220	nd	0.990	1.372
Fe(K)	47.284	49.589	0.990	1.401
Co(K)	0.150	0.040	0.990	1.492
Ni(K)	1.051	0.681	0.990	1.508

nd=not detected

Fig. 4. TEM-HRTEM analyses on iron-(oxy)-hydroxides from Çaldağ (sample CN-03): a) to c) HAADF-STEM images of iron-(oxy)-hydroxides (goethite) crystals; d) EDX mapping for Al, Si, Cr, Mn, Fe, Co, Ni; e) EDX analyses on selected areas of Fig. d; f) and g) HRTEM images showing the atomic structure of the selected areas and related d-spacing; h) SAED pattern for the selected area showing the typical pattern of polycrystalline and randomly oriented material.

medial concentrations in the dataset (avg. values = 1,673 ppm Cr, 1112 ppm Mn, and 1901 ppm Mg). In the FeO/OHs from Wingellina the most relevant trace elements are Al, Ti, Mn, Sc, and V (13,301–252,112 ppm Al, 358–5886 ppm Ti, 2333–15,210 ppm Mn, 25–105 ppm Sc and 220–391 ppm V). Although Cr and Mg are common impurities, their concentrations are erratic (259–5432 ppm Cr and 1162–7144 ppm Mg). Nickel, Zn, Co, and Si are in low concentrations (avg. values = 3297 ppm Ni, 77 ppm Zn, 42 ppm Co, 13,318 ppm Si) compared to the other deposits. In the Piauí deposit, the FeO/OHs are particularly enriched in a wide range of trace elements, namely Ti, Mn, Mg, Ni, Co, and Zn, whose concentrations range between 96 and 989 ppm Ti, 1723–5337 ppm Mn, 10,290–11,474 ppm Mg, 26,775–54,851 ppm Ni, 553–3276 ppm Co and 123–704 ppm Zn. The Si content varies between 13,717 and 30,426 ppm, while the amounts of Al, Cr, V, and Sc are relatively low (avg. values = 163 ppm Al, 474 ppm Cr, 32 ppm V, and 12 ppm Sc). The REEs are negligible in all the studied samples (<50 ppm total REE, Appendix C). The binary plots illustrate a good correlation between Ni and Co in goethites from Karaçam, Piauí, and in one set of data from Çaldağ; at the

Table 6
Summary of the obtained d-spacings of goethite and comparison with literature data.

Goethite (AMS data)*		Goethite (SAED, this study)	*h*	*k*	*l*
2.440	Çaldağ	2.418	1	1	1
2.290		2.287	0	0	2
2.180		2.161	4	0	1
2.002		2.001	3	1	1
1.793		1.791	1	1	2
1.558		1.559	5	1	1
1.499		1.491	5	0	2
1.469		1.462	4	1	2
1.287		1.297	4	2	0
1.239		1.228	4	2	1
2.575	Karaçam	2.576	2	1	0
2.478		2.478	4	0	0
2.231		2.218	1	0	2
2.180		2.172	4	0	1
1.557		1.561	5	1	1
1.449		1.434	6	1	0

* American Mineralogy Crystal Structure Database.

same time, they are poorly correlated in the data from Wingellina and few analyses from Çaldağ (Fig. 8a). Scandium is correlated with Al in all deposits, although the data from Wingellina goethites show a slight scattering (Fig. 8b). The Cr–V pair covaries significantly in the Çaldağ and Wingellina deposits, whereas no clear relationships have been observed for the goethites from Piauí and Karaçam (Fig. 8c).

5.5. Multivariate statistical analysis

The results of the PCA, carried out on the LA-ICP-MS data, show that the first three components (PC1–PC3) comply with the 10% cut-off value of explained variance and together account for approximately 90% of the total variance of the dataset (Table 7 and Fig. 9a). The PC1 vs. PC2 and PC1 vs. PC3 projections (Fig. 9b and c, respectively) show that FeO/OHs from the selected laterite deposits form clusters falling in different fields of the plots and are thus characterized by contrasting elemental associations. PC1, accounting for a significant portion of the explained variance (i.e., 53.79%), produces two anticorrelated groups of elements, which is Zn–Co–Ni–Si–(Mg–Mn) and Cr–(V), which along the PC1 axis have positive and negative loadings, respectively. The PC2 (21.24% of the explained variance) drives the generation of the Ti–Al–Sc group, which has negative PC2 values and close to zero PC1 loadings. It is worth noting that the PC2 also exerts a minor control on V, Mn, and Mg, whose *eigenvectors* are slightly displaced toward the bottom region of the plot. In this scenario, the trace element composition for the FeO/OHs from Karaçam, Piauí, and Çaldağ is mainly controlled by the PC1, with the point analyses of Karaçam and Piauí being correlated with the Zn–Co–Ni–Si group.

Furthermore, PC1 accounted for the formation of two clusters of FeO/OHs from Çaldağ (i.e., Çaldağ 1 and Çaldağ 2, Fig. 9). The former is correlated with the Cr *eigenvector*, while the Çaldağ 2 cluster has intermediate PC1 values. The distribution of FeO/OHs from Wingellina is significantly correlated with the Ti–Al–Sc group and less with V, Mn, and Mg. The PC3 (14.74% of the explained variance) provides insights into the difference between FeO/OHs from Karaçam and Piauí, which were grouped in a single cluster in the PC1 vs. PC2 projection. In particular, the third component exerts a significant clustering effect of the aforementioned FeO/OH species, with data from Piauí having positive values of PC3 and being correlated with Mn–Mg–Co–Ni–Ni group, data from Karaçam being displaced toward negative PC3 values and showing a relevant correlation with the Si, Sc, and Al *eigenvectors*.

The MANOVA test, carried out on the PC1 to PC5 (cumulative explained variance approximately 96%; Fig. 9a and Table 7), validated the statistical significance of the difference in the trace element composition of the FeO/OH types detected by the PCA (Pillai = 3.6709, Approximate F = 191.88, p-value < 0.001). The post hoc Tukey's test, conducted on the linear combinations of the PC1 to PC5 axis, shows that most of the FeO/OHs are different from one another, except for the Karaçam and Çaldağ 2 types, which were classified as belonging to the same statistical group (Table 8). However, it is worth mentioning that the MANOVA test provided a significant variance in the weightings of all deposits, thus confirming that the clusters defined by PCA are statistically meaningful.

6. Discussion

6.1. General features of iron-(oxy)-hydroxides in the studied Ni(Co)-laterites deposit

The current work was devoted to the study of FeO/OH phases within the "*oxide zone*" of four different Ni(Co)-laterite deposits located in different geographic areas (i.e., Wingellina, Western Australia; Piauí, Brazil; Karaçam and Çaldağ, Turkey). An extensive review of previous work has been included, but objective comparisons between literature data and new findings are problematic for two reasons. The first is that the published work individually focused on different aspects of FeO/OHs geochemistry and morphology in Ni(Co)-laterites (e.g., Sc content, As/Al ratio, REEs behavior, etc.). Secondly, there are clear differences in the analytical methods and procedures used in the published studies and the modern work; goethite features were investigated by different authors using different techniques (e.g., EDS, EPMA, LA-ICP-MS, etc.), making objective data comparisons difficult. Moreover, in works whose investigations were carried out by the same analytical technique, such as LA-ICP-MS, data are also difficult to compare since different standards were used during data acquisition. As a result, historical and modern data were only compared in the broadest sense in our discussion.

In the current study, we observed that goethite is the main FeO/OH in the oxide ores of the studied Ni(Co)-laterite deposits and is the sole phase in both the Çaldağ and Karaçam specimens, although hematite is recorded in other parts of these two deposits (Thorne et al., 2009; Herrington et al., in review). Only small amounts of hematite mixed with goethite were found at the Wingellina and Piauí deposits. These findings are in agreement with the literature on Ni(Co)-laterites, confirming goethite as the main FeO/OH mineral, while hematite might dominate either when gabbroic rocks are the main protolith or in the upper parts of the weathering profile where the dehydration results in the formation of Fe-oxides (Teitler et al., 2019; Ulrich et al., 2019).

Goethite-hematite mixtures in supergene deposits are common weathering products derived from complex processes involving the biosphere, atmosphere, and hydrosphere under tropical or subtropical conditions with defined wet and dry seasons. Even though all the studied deposits are currently located in warm, arid to semi-arid or temperate climatic zones, they all formed in more humid paleoclimates. The Karaçam and Çaldağ deposits formed during the Cretaceous to Early Eocene, for weathering of the ultramafic rocks occurred in tropical climatic conditions (Eliopoulos et al., 2012; Talvan et al., 2011; Thorne et al., 2012; Herrington et al., in review). The Piauí deposit is considered to have been formed through multistage weathering processes under different climatic regimes; the first one involving little seasonality and the second consisting in a tropical high seasonality regime developed in Pleistocene (Krüger, 2019). So far, no exact age has been established for the Wingellina Ni-laterite. Still, this deposit was supposed to have

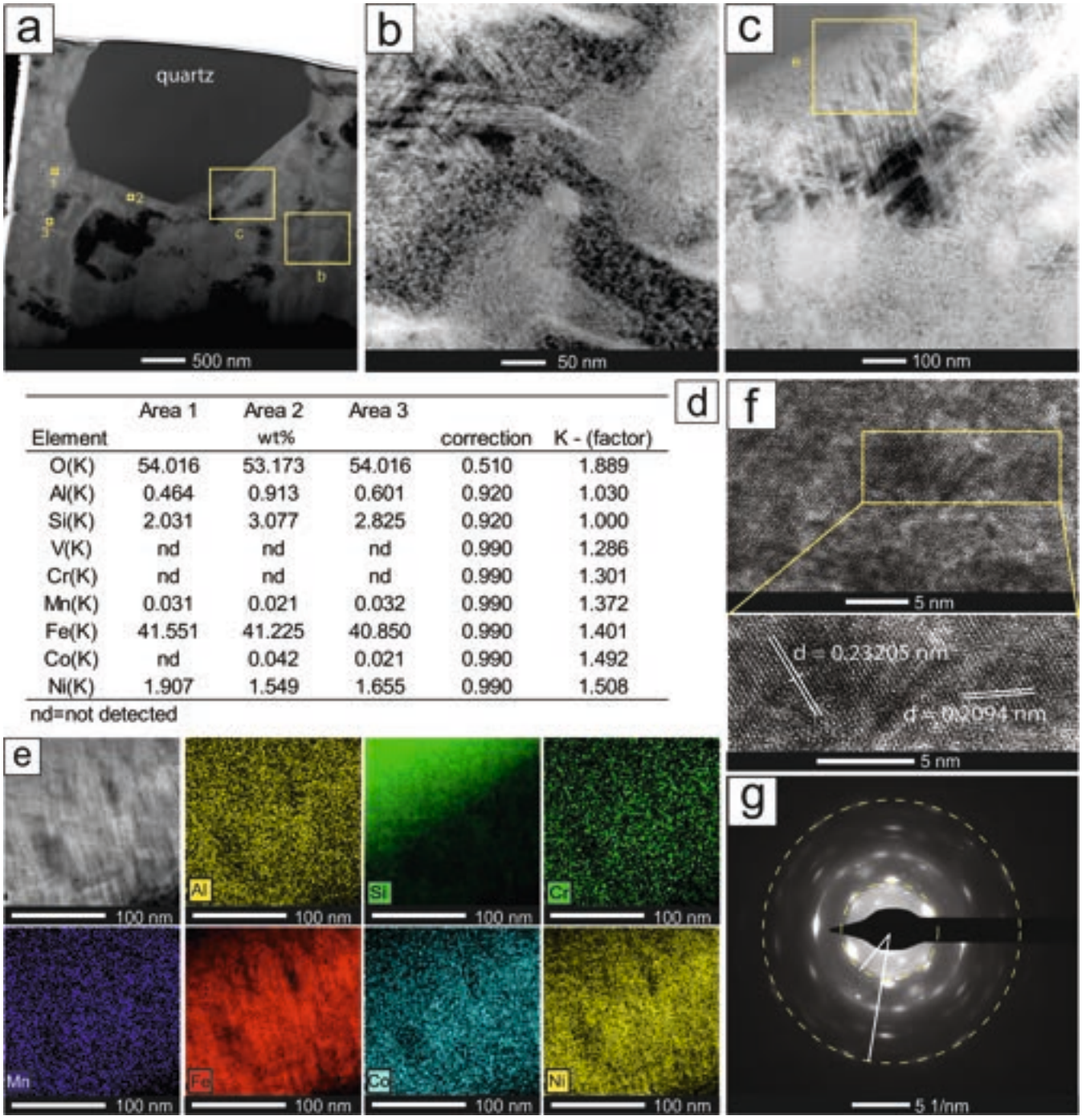

Fig. 5. TEM-HRTEM analyses on iron-(oxy)-hydroxides from Karaçam (sample KC-09): a) to c) HAADF-STEM images of iron-(oxy)-hydroxides (goethite) crystals; d) results of EDX analyses on selected areas of Fig. a; e) EDX mapping for Al, Si, Cr, Mn, Fe, Co, Ni; f) HRTEM images showing the atomic structure of the selected areas and related d-spacing; g) SAED pattern for the selected area indicating single crystals mixed with polycrystalline material with a random orientation (goethite).

formed during one of several weathering cycles that the Australian continent experienced before its migration outside the tropical latitudes during the Late Miocene (Putzolu et al., 2019).

Based on the XRPD and TEM-HRTEM data on FeO/OHs, no ferrihydrite was found in either of the samples. The FeO/OHs mainly consist of micro- to crypto-crystalline goethite in crusts or botryoidal concretions or as replacement of primary minerals. At the nanoscale, goethite occurs as platy to needle-like, variably oriented nanocrystals, commonly overlapping to form massive patches. Significantly, despite high Si levels being recorded, no discrete Si clusters were detected within goethite, and thus, it is concluded that the Si must be bound within the goethite crystal structure. The nano-crystallinity of goethite can be explained by acknowledging that natural FeO/OHs' morphology is due to the high rate of mineral precipitation in supergene environments (Cornell and Schwertmann, 2003).

6.2. *Deportment of trace elements in iron-(oxy)-hydroxides from Ni(Co)-laterites: The effect of parent rock and pH of the weathering systems*

The EMPA and LA-ICP-MS data of this study confirmed that FeO/OHs

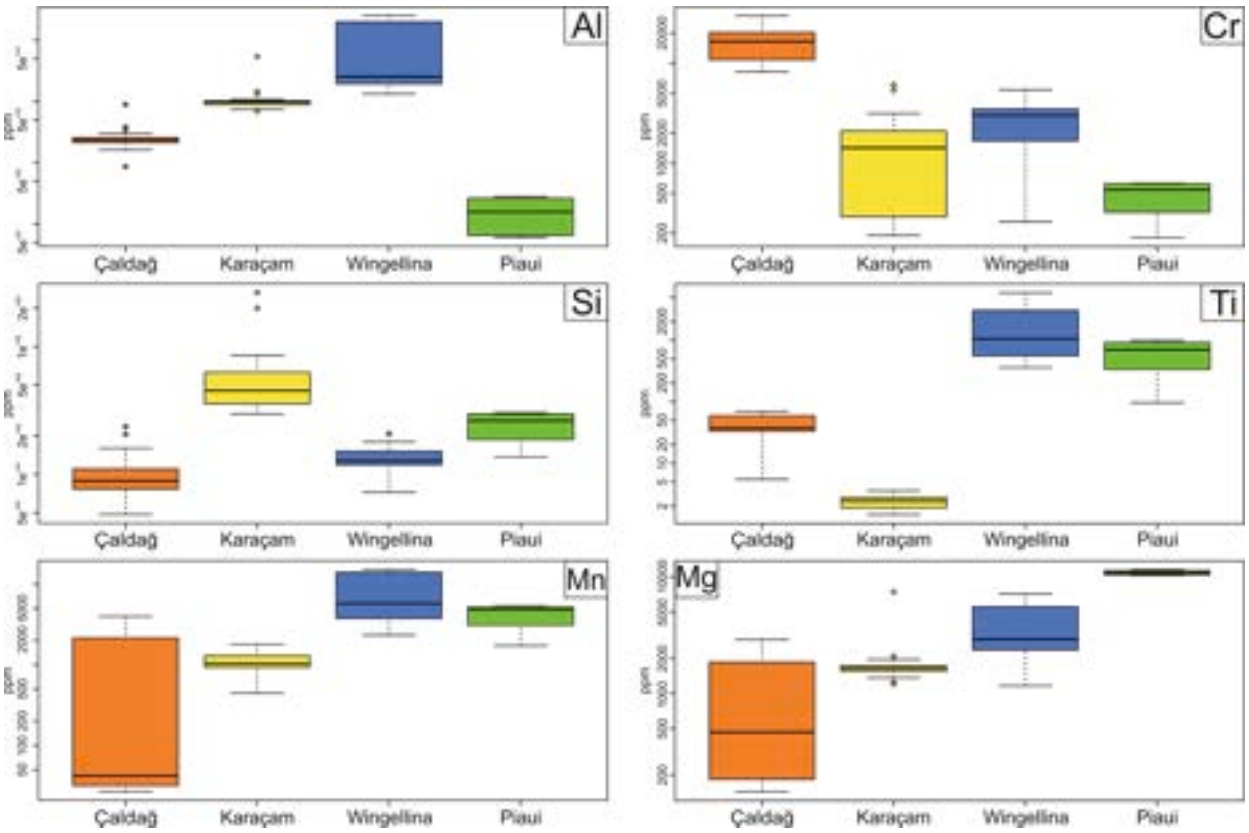

Fig. 6. Box and whisker plots showing the Al, Cr, Si, Ti, Mn and Mg concentrations by LA-ICP-MS of the studied iron-(oxy)-hydroxides.

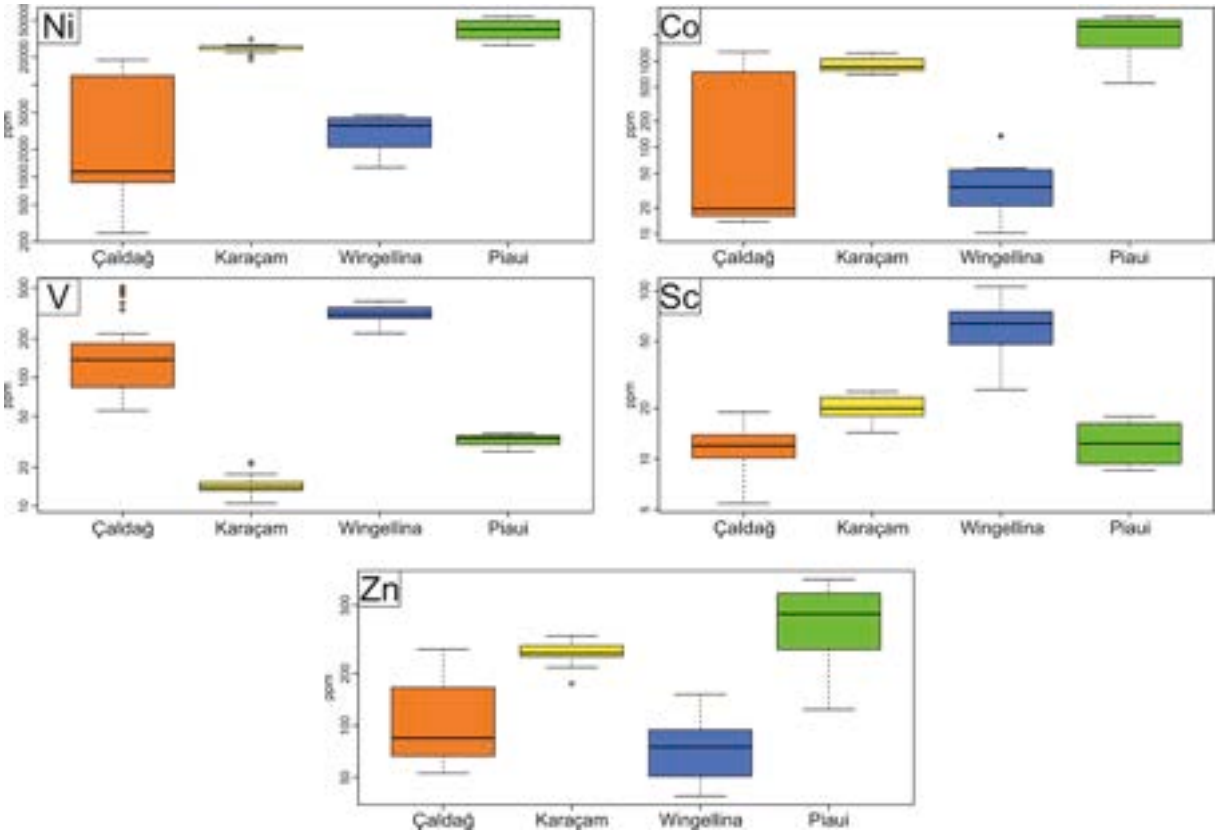

Fig. 7. Box and whisker plots showing the Ni, Co, V, Sc and Zn concentrations by LA-ICP-MS of the studied iron-(oxy)-hydroxides.

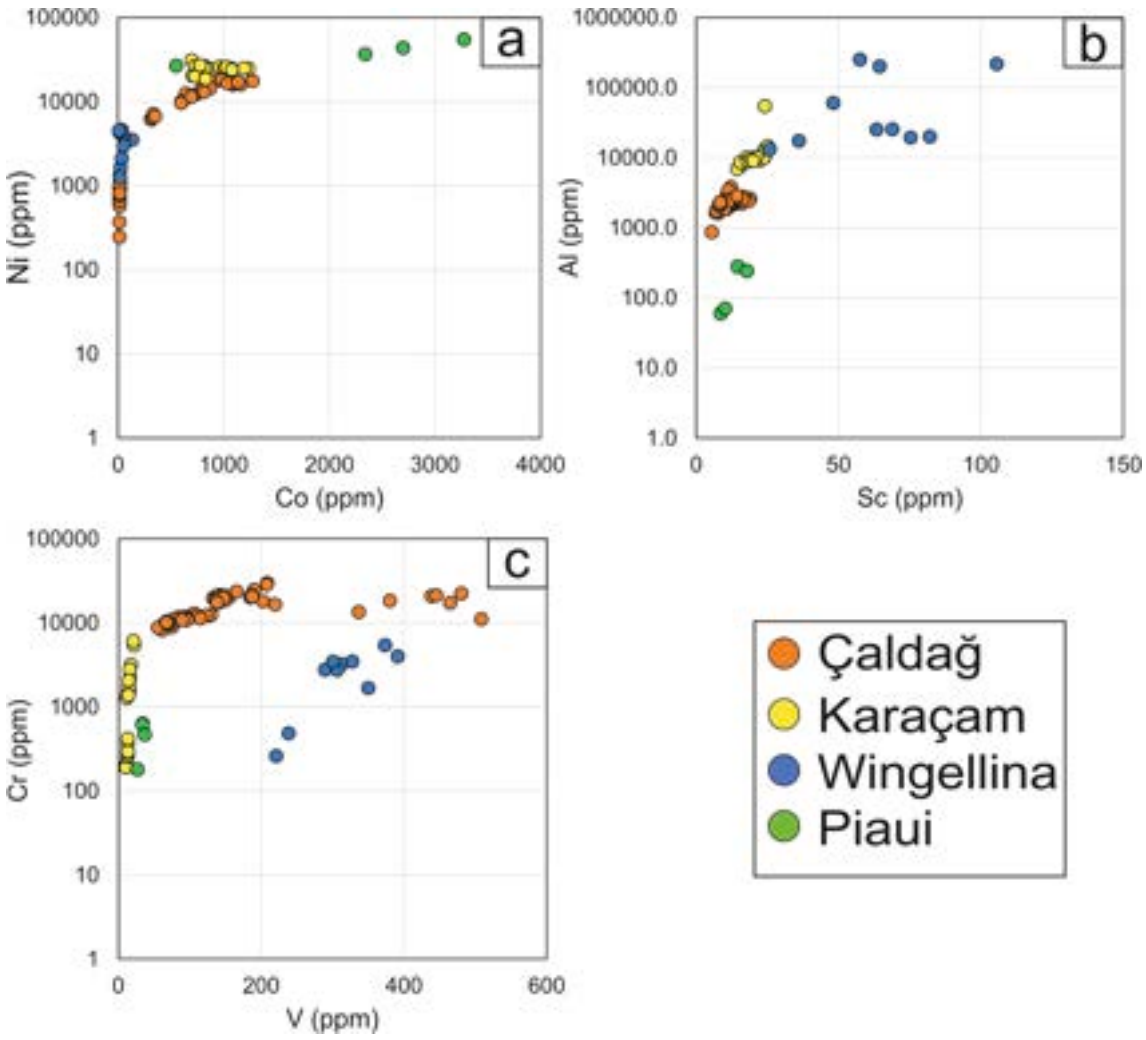

Fig. 8. Semilogarithmic binary plots showing the Al–Sc, Ni–Co and Cr–V covariance in the analysed goethite.

Table 7
Summary, loading and scores of the PCA performed on the LA-ICP-MS dataset.

	PC1	PC2	PC3	PC4	PC5	PC6	PC7	PC8	PC9	PC10	PC11
Standard deviation	2.43	1.53	1.27	0.67	0.53	0.40	0.33	0.25	0.20	0.12	0.12
Proportion of Variance (%)	53.79	21.24	14.74	4.03	2.56	1.45	1.01	0.56	0.38	0.13	0.12
Cumulative Proportion (%)	53.79	75.02	89.76	93.80	96.36	97.81	98.82	99.37	99.75	99.88	100.00

in Ni(Co)-laterite systems can host V, Ti, Al, Sc, Mn, Mg, Si, Ni, Co, Zn, and Cr, where Ni, Co, and Sc, reach levels of economic interest, while for other elements like V, Ti, Al, Mn, Mg, Si, and Zn, they are less likely to be economically recovered from goethite but can provide important insights into formation conditions of the profile. According to the PCA using these trace elements within FeO/OHs, three main associations have been observed: *i)* Cr–(V); *ii)* Co–Ni–Si–Zn; *iii)* Ti–Al–Sc–(V–Mn–Mg). Several FeO/OHs clusters have been observed along the PC1, reflecting the dichotomy between *i)* and *ii)* groups. Iron-(oxy)-hydroxides from Karaçam and Piauí correlate with the Co–Ni–Si–Zn group, while a subset of FeO/OHs from Çaldağ show a strong affiliation with Cr but a relatively poor affiliation with V. A data from Çaldağ plot in an intermediate position between the last two groups. Data from Wingellina mostly attributes to PC2 and thus correlates with the Ti–Al–Sc–(V–Mn–Mg) group. PC3 shows a close Cr–V association for the FeO/OHs from Çaldağ 1 and provides insights into the difference between Piauí and Karaçam clusters, with the latter having relatively higher Sc, Si, and Al contents. The above differences in trace element geochemistry may be explained by: *i)* the different features of the parent rocks of the selected deposits, and *ii)* the pH–Eh conditions occurring during the supergene ore formation processes. In supergene systems like laterites, the former aspect exerts a first-order control as it defines the presence/absence of a suite of elements in the ore system, whereas the physicochemical conditions in the supergene realm act as a second-order control, being able to drive the speciation of elements in specific mineral carriers. The effect of the first-order control explains the enrichment of Sc, Ti, and V in the FeO/OHs of the Wingellina laterite ore, as well as the scarcity of these elements in the other case studies. In ultramafic systems, Sc is fixed in pyroxene (Kd = 3.3; Dale and Henderson, 1972), which is also the source for V and Ti in New Caledonia laterite deposits (Teitler et al., 2019). Therefore, the alteration of the pyroxenite lenses of the Wingellina parent rock (Putzolu et al., 2018) may have increased the

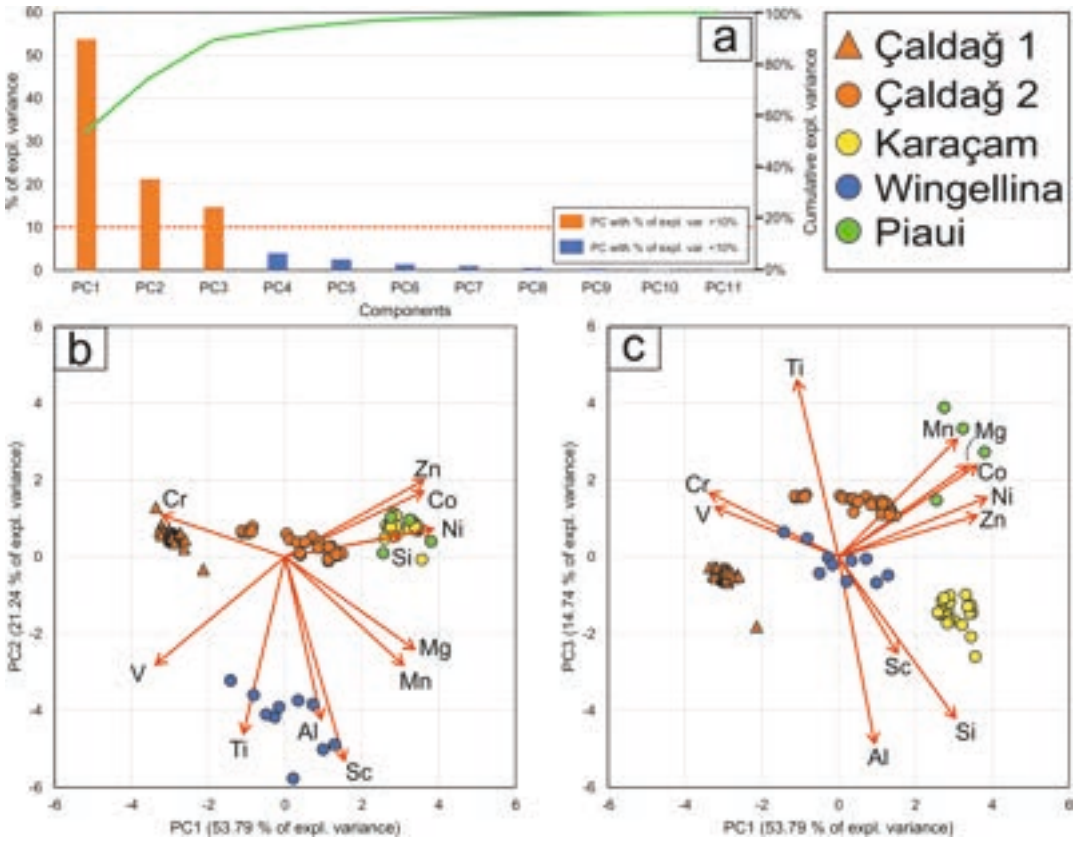

Fig. 9. Results of the principal component analysis (PCA) carried out on LA-ICP-MS data: a) Scree plot showing the % of explained variance of each PC of the dataset; b) and c) PC1 versus PC2 and PC3 biplots.

Table 8
Results of the post hoc Tukey's HSD test.

Deposit – FeO/OH type	Weighted difference	Group
Piaui	7.94	a
Karaçam	2.48	b
Çaldağ 2	1.73	b
Çaldağ 1	−2.85	c
Wingellina	−4.04	d

availability of Sc, Ti, and V. The PCA results also highlighted the Mn–Al association in FeO/OHs from the Wingellina deposit, which fits with the findings of Becquer et al. (2006), Raous et al. (2013), and Dublet et al. (2017), who reported on the common presence of Mn^{3+} in goethites formed in the lateritic environment. Furthermore, this Mn–Al association agrees with previous studies inferring a common substitution between Fe^{3+} by Al^{3+} and Mn^{3+} in weathered soils (Cornell and Schwertmann, 2003; Alvarez et al., 2007). Given that the Al content of mafic to ultramafic protoliths is low, the Al and Mn speciation in the specific case of FeO/OHs from Wingellina can be explained by the pH effect in the weathering system, the second-order control. Mn may be released from the preferential dissolution of the Mn-(oxy)-hydroxides in the uppermost portion of the regolith due to low pH conditions (Dublet et al., 2015; Dublet et al., 2017), which explains the inverse correlation between Cr and Co–Ni–Si–Zn groups, and thus the dichotomy between the chemistry of FeO/OHs from Çaldağ 1 and Karaçam–Piauí. According to mineral and petrographic data, goethites from Çaldağ are the most Cr enriched among the studied FeO/OH species. Previous studies indicate that the Cr adsorption onto goethite is a common process during lateritization and reaches the highest rates at low pH (pH = 2–5.5) (Schwertmann and Latham, 1986; Trolard et al., 1995; Schwertmann and Pfab, 1996; Oze et al., 2004; Fandeur et al. 2009; Yu et al., 2009; Ajouyed et al., 2010 and references therein). The FeO/OHs from Karaçam and Piauí are characterized by the Co–Ni–Si–Zn association. Published studies highlight that the main factors controlling the Ni-uptake in goethites are: *i)* the degree of crystallinity of the FeO/OH phases, and *ii)* the pH of the system. Vitovskaya (1989) showed that Ni content is always higher in gel-like amorphous phases than in crystalline phases with partial loss of Ni during the crystallization process. Moreover, the pH conditions and the presence of Si in the system can also influence the scavenging potential of goethite. The experiments of Gerth et al. (1993) tested Si-bearing goethite's ability to capture heavy metals such as Ni, Zn, and Cd at pH values of ~6–6.5. In contrast, Beukes et al. (2000) showed that the Ni-uptake in synthetic goethites reaches its maximum efficiency at pH values ranging between 6 and 8. Based on these results, we can infer that goethites from Karaçam and Piauí deposits formed in an environment relatively less acid than Çaldağ and Wingellina laterites. This outcome may explain the differences between goethites from Çaldağ and Karaçam, despite the two laterite deposits derived from similar parent rocks. Further clues about pH control come from the studies conducted by Teitler et al. (2019) and Ulrich et al. (2019) on goethites from New Caledonian laterite deposits; the authors inferred that FeO/OHs geochemistry regarding their Si, Ni, and Cr content vary depending on their location within the weathering profile. The above findings likely reflect different pH conditions in different horizons of the laterite system (i.e., high-Cr FeO/OHs in the oxide ore and high Ni–Si FeO/OHs in the saprolite ore). Concerning Co, the PCA results showed a negative correlation with Cr; as argued before, the presence of Cr in goethite is a proxy for the acidity of the pedogenetic system, so differences in the Co content of the FeO/OHs may be a function of the pH variations in the percolating groundwater. Cobalt is commonly adsorbed onto goethite between pH ~6 and 7.5, and its adsorption rate increases with increasing pH. Also, at pH values between

8 and 10, Co is likely to be present as a mixture of both Co^{2+} and Co^{3+} (Schenck et al., 1983). The strongly negative correlation between Cr and Co is in agreement with the proposed second-order of control, that the pH of the weathering system playing a key role in defining the trace element budget. Observations at Çaldağ support this idea, as it is the only deposit where the phyllosilicate-rich saprolite horizon is absent or poorly developed (Thorne et al., 2009), whereas the Wingellina, Karaçam and Piauí profiles all show a well-defined saprolite interval (Putzolu et al., 2018; Putzolu et al., 2019; Putzolu et al., 2020; Herrington et al., in review). Several authors (e.g., Gleeson et al., 2004; Golightly, 2010 and references therein) link the formation of a thick silicate-rich saprolite to higher stability of the newly formed silicate minerals when interacting with higher pH fluids in the deepest zones of the weathering profiles.

6.3. The potential role of silicon in the uptake of trace elements in iron-(oxy)-hydroxides

Silicic acid (H_4SiO_4) is a common product of weathering of silicates (Lindsay, 1979), and its adsorption and polymerization on the surfaces of FeO/OHs have strong effects on their stability, as well as on their surface chemistry (Davis et al., 2002; Swedlund et al., 2010; Song et al., 2013). The presence of Si within the FeO/OHs, especially in goethite, is quite controversial and is still a matter of debate. Previous studies report that Si is preferentially adsorbed onto specific crystal planes of goethite (Cornell et al., 1987; Cornell and Giovanoli, 1989) rather than incorporated in the mineral structure. Furthermore, the occurrence of Si within FeO/OHs is also believed to influence positively or negatively their chemical reactivity concerning metal retention. Gerth et al. (1993) assessed the increased capability of Si-rich goethite to uptake Zn, Ni, and Cd at slightly acid to neutral pH (~6–6.5).

On the other hand, the presence of H_4SiO_4 can compete for adsorption sites on ferrihydrite and goethite and make their surfaces less accessible to other anions occurring in solution (Swedlund and Webster, 1999; Luxton et al., 2008). Although natural metal-rich goethite is often Si-rich, as in the case of the Karaçam and Piauí goethites measured in this study, Si is not easily accommodated into the goethite structure, and its enrichment process in FeO/OHs is still not resolved. Therefore, although ferrihydrite was not detected in this study, the presence of this metastable Fe-phase could have played a role in facilitating the Si uptake during the early stage of formation of FeO/OHs before they transform to more stable phases. Other studies have revealed the pH dependency of Si adsorption on goethite, highlighting that this process reaches its highest efficiency at a basic pH of 9 (Kingston et al., 1972; Swedlund and Webster, 1999; Luxton et al., 2006; Himestra et al., 2007) and decreases at both lower and higher pH. These results agree with the Si association outlined by the PCA in the studied FeO/OHs (Fig. 9b), since Si-bearing goethite is spatially distinct from goethites enriched in trace elements like Cr, which, as stated before, represent a proxy for more acidic conditions. Therefore, understanding the Si distribution in FeO/OH minerals is a pivotal step in increasing the knowledge about the factors influencing the distribution of many economic elements during the weathering processes.

6.4. Goethite as a non-conventional metal source

In oxide-type Ni(Co)-laterites, goethite may represent the principal ore mineral (Brand et al., 1998; Elias, 2002). Goethite is amenable to treatment by hydrometallurgy processes, i.e., the Caron Process (Dalvi et al., 2004; Asselin, 2011), High-Pressure Acid Leaching (HPAL, Georgiou and Papangelakis, 1998; Kar et al., 2000; Rubisov and Papangelakis, 2000; Rubisov et al., 2000; Moskalyk and Alfantazi, 2002), Heap Leaching (HL) and Atmospheric Leaching (AL) (McDonald and Whittington 2008, Kyle, 2010 and references therein, Oxley et al. 2016). In the last decade, experimental studies on the bioprocessing of oxide ores (mainly consisting of goethite) were carried out on low-grade Ni(Co)-laterites with a recovery of over 70% of Ni and >99% of Co recorded (Ñancucheo and Johnson, 2010; Hallberg et al., 2011; Johnson et al., 2013; Johnson and du Plessis, 2015; Marrero et al., 2015; Smith et al., 2017). Many studies have also been carried out to assess the recovery of REEs, Sc, Ga, Ge, V, and other economically valuable heavy metals from *red mud* residues of the Bayer process applied to the alumina production from bauxite. The composition of *red muds* mainly consists of FeO/OHs, i.e., hematite and goethite, plus other minor phases (i.e., diaspore, gibbsite, calcite, rutile, etc.). Therefore, the processing techniques tested on *red muds* might also be effective on natural FeO/OHs formed in supergene ores. Borra et al. (2016a) reported that the combination of sulfation-roasting-leaching processes provides a significant breakthrough for the selective recovery of REEs and Sc from Fe-rich *red muds*, while Qu et al. (2013) and Qu et al. (2015) investigated the high efficacy of using bioleaching for the recovery of Ga, Ge, V, Sc, La, Eu, Yb, and heavy metals (i.e., Cd, Cr, Cu, Ni, Zn, and As) from *red muds* by the use of the fungus *Aspergillus Niger*.

The Pb and Zn contents of goethite in nonsulfide ore deposits are relatively high, but it is still considered too low to make metal recovery economically profitable using standard recovery methods. However, successful experiments have been carried out to assess the extraction of Zn, Pb, and other valuable metals from goethite wastes by either pyrometallurgy (Piga et al., 1995) or hydrometallurgy (Pelino et al., 1996). However, these processes are not currently viable on an industrial scale (Di Maria and Van Acker, 2018). Wang et al. (2013) have assessed the efficiency of the recovery of Zn from goethite and Zn-Ag from residues of the hydrometallurgy processes by using blowing methods, while Di Maria and Van Acker (2018) proposed the use of plasma fuming, followed by inorganic polymerization of the fumed slags.

7. Conclusions

This study focused on the geochemistry of natural FeO/OHs (mainly goethite) within the oxide horizons of Ni(Co)-laterites from four important "*oxided type*" globally representative deposits, namely Wingellina (Western Australia), Piauí (Brazil), Karaçam and Çaldağ (Turkey). The study yielded the following findings:

i) Goethite morphology and the degree of crystallinity are highly variable. The growth rate of the minerals influences both features. In the surficial environment, the mineral precipitation is rapid, resulting in nanocrystalline-to amorphous crystalline minerals;
ii) The studied goethite hosted variable concentrations of "*impurities*", with Ni, Si, and Al being the most common, followed by Co, Cr, and Mn. Mg is abundant at Piauí, while noteworthy Sc, V, and Ti concentrations were found in goethites from Wingellina. The Çaldağ goethites also show locally high V and Cr contents.
iii) Three major element associations were defined for the studied goethites: Mn–Al–Ti–Sc–V in the Wingellina samples; Mg–Ni–Si–Co association in the samples from Karaçam and Piauí, and Cr–V in Çaldağ samples. The contrasting associations are linked to the composition of the parent lithology and local weathering conditions (mainly the pH), which may enhance or restrict element fixation in FeO/OHs;
iv) High Si values recorded in FeO/OHs. Transmission Electron Microscopy analyses (TEM) confirm that Si is likely to be structurally bound in crystalline goethite. No evidence for any other Si-rich forms of FeO/OH was found.

The comparison between the novel results of our study and the published literature confirms and strengthens some of the conclusions on controls, features, and occurrences of FeO/OHs associated with supergene ore deposits. These conclusions can be summarized as follows:

i) The enrichment of elements, such as Sc, is primarily a function of the mineralogy of the parent rock, which is a first-order control on FeO/OH chemistry since the weathering of specific Sc-bearing minerals influences the element availability in the weathering system.
ii) The incorporation of elements into goethite is a function of pH, a second-order control of goethite chemistry. Neutral to basic pH favors the Ni and Co incorporation, whereas more acidic pH favors higher Cr concentrations within goethites.
iii) Climatic seasonality may trigger the dissolution-leaching-precipitation of unstable phases in surficial environments and hence the re-mobilization of metals within the weathering system. Seasonality influences a deposit's hematite/goethite ratio, as dry periods favor hematite crystallization via goethite dehydration. The latter process may also increase the availability of valuable metals (i.e., Sc), which are liberated from goethite and available to be remobilized and further enriched in late FeO/OHs.
iv) Further work is also needed to assess the FeO/OH's potential as non-conventional metal sources for a wider range of useful elements. Currently, goethite is targeted as a source of Ni and Co (and potentially Sc) metal in laterite ores. Goethite and other FeO/OHs in the *red muds* may also be suitable and targeted for future metal recovery. The role exerted by the type of bonding and presence of specific impurities (especially Si) on trace metal uptake in FeO/OHs is still poorly constrained. Further synchrotron-based studies should be carried out to better assess the nature of the minor metal association within the FeO/OH structure.

Author contributions

L.S. carried out specimen collection, XRPD, SEM-EDS, EPMA, TEM-HRTEM, EDX and LA-ICP-MS data collection, partial data interpretation and writing of the original draft of the paper; F.P performed the multivariate statistical analysis, the interpretation of LA-ICP-MS data and writing of the original draft of the paper; N.M, M.B and R.H have been partly in charge of data interpretation and of reviewing and editing.

Declaration of Competing Interest

The authors declare that they have no known competing financial interests or personal relationships that could have appeared to influence the work reported in this paper.

Acknowledgments

The authors are grateful to the NHM (London) curators S. Kocher (curator of the ores collection) and E. Vaccaro (curator of the petrology collection), for the efforts made during the selection of the specimens, as well as to the staff of the Core research Laboratories at NHM for the support given during the analytical work. The authors are also indebted to the reviewers for their observations and criticisms, which greatly improved the first version of the manuscript.

Funding information

This project has received funding from the European Union's Horizon 2020 research and innovation program, by a Marie Skłodowoska-Curie Individual Fellowship (Project number 751103) awarded to R. Herrington, supporting the fellowship of L. Santoro.

Appendix

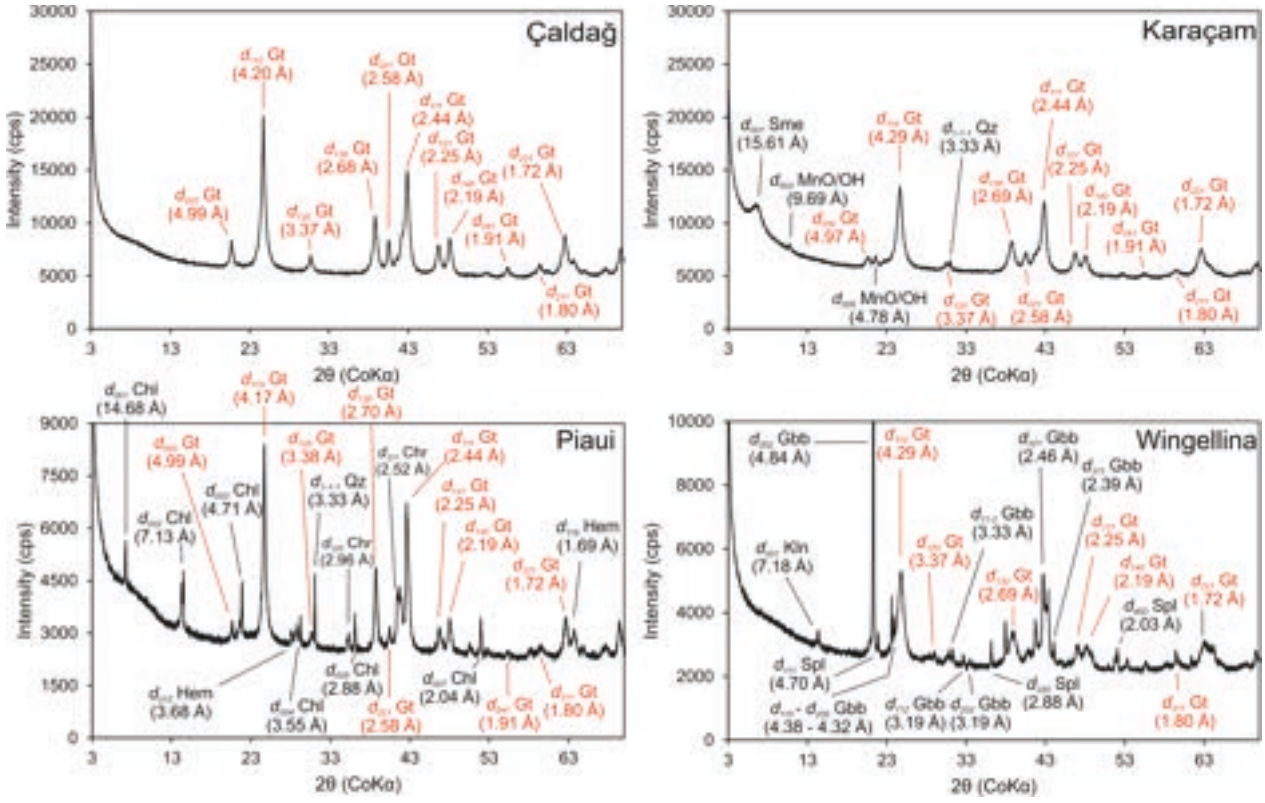

Appendix A. Selected XRPD patterns of the studied goethite-rich laterite samples. Abbreviations: Gt = goethite; Sme = smectite; MnO/OH = Mn-oxy-hydroxide (lithiophorite – asbolane); Qz = quartz; Chl = chlorite (clinochlore); Chr = chromite; Spl = spinel; Hem = hematite; Kln = kaolinite; Gbb = gibbsite.

Appendix B

LA-ICP-MS data of goethites from the studied Ni(Co)-laterite deposits.

^{89}Y µg-g-1	^{115}In µg-g-1	^{139}La µg-g-1	^{140}Ce µg-g-1	^{141}Pr µg-g-1	^{146}Nd µg-g-1	^{147}Sm µg-g-1	^{153}Eu µg-g-1	^{157}Gd µg-g-1	^{159}Tb µg-g-1	^{163}Dy µg-g-1	^{165}Ho µg-g-1	^{166}Er µg-g-1	^{169}Tm µg-g-1	^{172}Yb µg-g-1	^{175}Lu µg-g-1	^{208}Pb µg-g-1	^{232}Th µg-g-1	^{238}U µg-g-1	LREE µg-g-1	MREE µg-g-1	HREE µg-g-1	Tot REE µg-g-1
0.4	<0.0166	0.0	0.0	0.0	<0.0292	<0.0154	0.0	<0.047	<0.00474	0.1	0.0	0.0	0.0	0.0	0.0	0.0	0.1	18.5	0.1	0.1	0.1	0.3
0.6	0.0	0.0	0.0	0.0	0.0	<0.0149	0.0	<0.0404	0.0	0.0	0.0	0.0	0.0	0.1	0.0	<0.027	0.1	24.9	0.1	0.1	0.1	0.3
0.6	<0.0146	0.0	0.0	0.0	<0.0274	<0.0161	<0.00601	0.1	0.0	0.0	0.0	0.0	0.0	0.1	0.0	<0.0303	0.1	25.7	0.1	0.1	0.2	0.3
0.4	<0.0541	0.0	0.1	<0.00685	<0.106	<0.0958	<0.0128	0.1	<0.0195	0.1	<0.00697	<0.021	<0.0171	0.0	<0.0139	<0.0687	0.1	17.3	0.2	0.2	0.1	0.5
0.2	<0.0282	0.0	0.0	0.0	0.0	<0.07	<0.0148	<0.0713	0.0	<0.0204	0.0	<0.0307	0.0	<0.033	0.0	<0.0604	0.2	10.4	0.1	0.1	0.1	0.3
0.2	0.0	0.0	0.0	0.0	<0.0414	<0.0437	<0.00583	0.0	0.0	<0.0127	<0.00636	0.0	<0.00422	0.0	0.0	<0.0484	0.2	10.5	0.1	0.1	0.1	0.2
0.2	<0.0219	0.0	0.0	<0.0083	<0.0383	<0.0225	<0.00599	<0.0883	<0.00688	0.0	0.0	<0.00983	<0.00309	0.0	<0.00326	<0.0414	0.2	11.0	0.1	0.1	0.0	0.2
0.2	0.0	0.0	0.0	<0.00427	<0.0898	<0.0176	<0.00937	<0.0377	<0.0068	0.0	0.0	0.0	<0.00484	0.0	<0.00566	<0.0306	0.2	11.2	0.1	0.1	0.1	0.2
0.5	<0.663	0.0	0.0	0.0	<0.0289	0.0	0.0	<0.0414	0.0	0.0	0.0	0.0	0.0	0.0	0.0	0.1	0.0	24.5	0.1	0.1	0.1	0.2
0.5	<0.0175	0.0	0.0	0.0	0.0	0.0	<0.00745	<0.0658	0.0	0.0	0.0	0.0	0.0	0.1	0.0	<0.0289	0.0	24.9	0.1	0.1	0.1	0.4
0.6	<0.0154	0.0	0.0	0.0	0.1	<0.0147	<0.00668	<0.0589	0.0	0.1	0.0	0.0	0.0	0.1	0.0	<0.0261	0.0	31.2	0.1	0.1	0.1	0.4
0.5	<0.0452	0.2	0.0	<0.0184	0.1	<0.0918	<0.0122	<0.151	<0.0108	0.0	<0.00666	<0.02	<0.00631	0.0	0.0	<0.0847	0.1	19.0	0.3	0.2	0.1	0.5
0.6	<0.0148	0.0	0.1	0.0	0.1	0.0	0.0	<0.0397	0.0	0.0	0.0	0.0	<0.00869	0.1	0.0	<0.0305	0.0	29.3	0.1	0.1	0.1	0.4
0.8	<0.0234	0.0	0.0	0.0	<0.0396	<0.0192	0.0	0.0	0.0	0.0	0.0	0.0	0.0	0.1	0.0	<0.041	0.1	31.0	0.1	0.1	0.1	0.3
0.7	0.0	0.0	0.0	0.0	0.0	<0.0148	<0.00789	0.0	<0.00286	0.0	0.0	0.0	0.0	0.1	0.0	<0.0263	0.1	30.5	0.1	0.1	0.1	0.3
0.6	0.0	0.0	0.0	0.0	0.0	<0.0171	<0.0101	0.0	0.0	0.0	0.0	0.0	<0.00468	0.0	0.0	<0.0237	0.1	24.2	0.1	0.1	0.1	0.3
0.4	0.0	0.0	0.0	0.0	<0.0409	<0.048	<0.00809	<0.0503	<0.00596	0.0	0.0	0.1	<0.00505	0.0	0.0	0.1	0.1	26.5	0.1	0.1	0.1	0.3
0.7	0.0	0.0	0.0	0.0	0.0	<0.03	0.0	<0.0428	0.0	0.1	0.0	0.0	0.0	0.1	0.0	0.0	0.1	29.5	0.1	0.1	0.1	0.4
0.4	<0.0354	0.0	<0.0592	0.0	0.1	<0.0354	<0.00946	<0.0341	<0.0108	<0.0455	<0.0114	0.0	<0.00486	0.0	<0.0152	<0.0572	0.1	24.2	0.1	0.1	0.1	0.3
0.4	<0.0175	0.0	0.0	0.0	<0.0162	<0.038	<0.0101	<0.0406	0.0	<0.0325	0.0	0.0	0.0	<0.0224	0.0	<0.0447	0.1	16.4	0.1	0.1	0.1	0.2
0.2	0.0	0.0	0.0	<0.00498	0.0	<0.0249	<0.0187	0.0	<0.00687	0.0	<0.00722	0.0	<0.00758	0.0	<0.0102	0.2	0.2	11.8	0.1	0.1	0.1	0.2
0.4	<0.0179	0.0	0.0	0.0	<0.0171	<0.0563	<0.00536	<0.0271	0.0	<0.028	0.0	0.0	<0.00468	0.0	<0.00584	<0.0325	0.1	15.9	0.1	0.1	0.1	0.2
0.4	0.0	0.0	0.0	0.0	0.0	0.0	<0.00999	<0.036	0.0	0.0	0.0	0.0	<0.00768	0.0	0.0	<0.0317	0.1	18.5	0.1	0.1	0.1	0.3
0.6	<0.016	0.0	0.0	0.0	0.0	<0.0173	0.0	0.0	0.0	0.0	0.0	0.0	<0.00473	0.1	0.0	<0.0293	0.0	24.0	0.1	0.1	0.1	0.3
0.5	0.0	0.0	0.0	0.0	0.1	<0.0708	0.0	0.0	<0.00814	0.1	0.0	0.0	<0.00809	0.1	0.0	<0.0285	0.1	23.7	0.1	0.1	0.1	0.4
0.6	<0.0174	0.0	0.0	0.0	0.1	<0.0156	0.0	0.0	0.0	0.1	0.0	0.0	0.0	0.1	0.0	<0.0274	0.0	25.2	0.1	0.1	0.1	0.4
0.0	0.0	0.0	0.1	0.0	0.0	<0.0215	<0.00625	<0.00928	<0.00268	<0.0095	<0.00414	<0.00943	<0.00323	<0.00702	<0.0014	<0.0192	0.0	2.3	0.1	0.0	0.0	0.2
0.0	0.0	0.0	0.1	0.0	0.0	<0.0096	<0.00257	<0.0204	<0.00133	0.0	<0.00139	<0.0124	<0.00133	<0.00533	<0.00278	<0.0154	0.0	2.2	0.1	0.0	0.0	0.2
0.0	0.0	0.0	0.1	0.0	0.0	<0.0342	<0.00513	<0.0129	<0.00265	<0.0155	<0.00139	0.0	0.0	<0.00313	<0.00307	<0.0107	0.0	2.5	0.1	0.0	0.0	0.2
0.0	0.0	0.0	0.1	0.0	0.0	<0.0189	<0.00252	<0.0201	<0.0029	<0.00545	<0.00137	<0.00414	<0.0013	<0.00523	<0.00136	<0.0182	0.0	2.3	0.1	0.0	0.0	0.2
0.0	0.0	0.0	0.1	0.0	0.0	<0.00951	<0.00254	0.0	<0.00132	0.0	<0.00276	<0.0129	0.0	<0.00435	<0.00275	<0.0201	0.0	2.5	0.1	0.0	0.0	0.2
0.0	<0.0133	0.0	0.1	0.0	0.0	<0.0205	0.0	0.0	<0.00128	<0.0119	<0.00376	<0.00406	<0.00256	<0.00671	<0.00134	<0.0206	0.0	2.5	0.1	0.0	0.0	0.2
0.0	0.0	0.0	0.1	0.0	0.0	<0.0142	<0.00272	<0.0217	<0.00197	0.0	<0.00413	<0.00447	<0.00141	<0.00737	<0.00147	<0.0228	0.0	1.9	0.1	0.0	0.0	0.2
0.0	0.0	0.0	0.1	0.0	0.0	<0.0102	<0.00656	<0.00977	<0.00141	<0.0118	<0.00148	<0.00447	0.0	<0.008	<0.00294	<0.0174	0.0	1.7	0.2	0.0	0.0	0.2
0.0	0.0	0.0	0.1	0.0	0.0	0.0	<0.00758	<0.00972	<0.0014	0.0	0.0	0.0	<0.0028	<0.0033	<0.00146	0.0	0.0	1.8	0.2	0.0	0.0	0.2
0.0	0.0	0.0	0.1	0.0	0.0	0.0	<0.00515	<0.0157	<0.00266	<0.00556	<0.00139	0.0	<0.00133	<0.00757	0.0	<0.0119	0.0	1.6	0.2	0.0	0.0	0.2
0.0	0.0	0.0	0.1	0.0	0.1	<0.00947	0.0	<0.0202	<0.00184	<0.00548	<0.00385	<0.0107	<0.00291	<0.00746	<0.00274	<0.0144	0.0	1.6	0.2	0.0	0.0	0.2
0.0	0.0	0.0	0.1	0.0	0.0	0.0	<0.00265	<0.0211	<0.00137	<0.00572	<0.00318	<0.00964	<0.00137	0.0	<0.00317	<0.0132	0.0	1.3	0.2	0.0	0.0	0.2
0.0	0.0	0.0	0.1	0.0	0.0	<0.0204	<0.00273	<0.0218	<0.00283	<0.00592	<0.00357	<0.00449	<0.00313	0.0	<0.00148	<0.019	0.0	1.6	0.1	0.0	0.0	0.2
0.0	<0.0133	0.0	0.1	0.0	0.0	<0.00975	<0.00365	<0.0226	<0.00135	<0.00791	<0.00141	<0.0126	<0.00135	<0.00891	<0.00141	<0.0197	0.0	2.1	0.1	0.0	0.0	0.2
0.7	0.0	0.5	0.5	0.1	0.5	0.1	0.0	0.1	0.0	0.1	0.0	0.1	0.0	0.1	0.0	<0.0271	0.0	3.3	1.6	0.3	0.2	2.1
0.6	0.0	0.4	0.3	0.1	0.4	0.1	0.0	0.1	0.0	0.1	0.0	0.0	0.0	0.0	0.0	<0.0167	0.0	3.3	1.2	0.2	0.1	1.5
0.4	0.0	0.3	0.2	0.1	0.2	0.0	0.0	0.0	<0.0052	0.0	0.0	0.0	0.0	0.0	0.0	<0.0155	0.0	2.8	0.8	0.1	0.1	1.0
0.0	0.0	0.0	0.1	0.0	0.0	<0.0252	<0.00864	0.0	<0.00322	<0.00607	<0.00152	<0.0046	<0.00145	0.0	<0.00151	<0.0114	0.1	0.6	0.1	0.0	0.0	0.2
0.0	0.0	0.0	0.0	0.0	0.0	0.0	<0.00825	<0.0106	<0.00305	<0.00639	<0.0016	<0.00968	0.0	<0.0111	<0.00159	<0.0155	0.1	0.6	0.1	0.0	0.0	0.1
0.0	0.0	0.0	0.1	0.0	0.1	<0.00956	0.0	<0.0205	<0.00294	0.0	0.0	0.0	0.0	0.0	0.0	<0.0218	0.0	0.9	0.2	0.0	0.0	0.2
0.0	0.0	0.0	0.1	0.0	0.0	<0.029	0.0	<0.019	<0.00302	<0.0137	<0.00143	<0.00432	<0.00515	<0.00545	<0.00367	0.0	0.0	0.8	0.1	0.0	0.0	0.2
0.0	0.0	0.0	0.1	0.0	0.0	<0.0216	<0.00261	<0.0243	<0.00326	<0.0192	<0.00142	0.0	<0.00135	<0.00637	<0.00141	<0.0204	0.0	0.8	0.1	0.0	0.0	0.2
0.0	0.0	0.0	0.1	0.0	0.0	<0.0188	0.0	<0.0127	0.0	<0.0164	<0.00137	<0.00414	<0.0013	0.0	<0.00136	0.0	0.0	0.8	0.1	0.0	0.0	0.2
0.0	0.0	0.0	0.1	0.0	0.0	<0.00966	<0.00258	<0.0131	<0.00134	<0.00561	<0.0014	<0.00425	<0.00133	0.0	<0.0014	<0.0209	0.0	0.9	0.1	0.0	0.0	0.2
0.1	0.1	0.1	0.1	0.0	0.1	<0.0223	<0.0103	<0.0306	<0.00182	0.0	0.0	<0.00577	<0.00181	<0.00428	<0.0019	0.0	0.2	1.0	0.3	0.1	0.0	0.4
0.0	0.1	0.0	0.1	0.0	0.0	<0.0114	<0.00304	<0.011	<0.00158	<0.00661	0.0	<0.005	<0.00157	<0.0052	<0.00165	<0.0229	0.2	0.2	0.1	0.0	0.0	0.1
0.0	0.0	0.0	0.1	0.0	<0.0323	<0.0344	<0.827	<0.0233	<0.00238	<0.00998	<0.00249	<0.0195	<0.00237	<0.0173	<0.00599	<0.0237	0.1	0.2	0.1	0.6	0.0	0.7

(*continued on next page*)

Appendix B (*continued*)

^{89}Y µg-g-1	^{115}In µg-g-1	^{139}La µg-g-1	^{140}Ce µg-g-1	^{141}Pr µg-g-1	^{146}Nd µg-g-1	^{147}Sm µg-g-1	^{153}Eu µg-g-1	^{157}Gd µg-g-1	^{159}Tb µg-g-1	^{163}Dy µg-g-1	^{165}Ho µg-g-1	^{166}Er µg-g-1	^{169}Tm µg-g-1	^{172}Yb µg-g-1	^{175}Lu µg-g-1	^{208}Pb µg-g-1	^{232}Th µg-g-1	^{238}U µg-g-1	LREE µg-g-1	MREE µg-g-1	HREE µg-g-1	Tot REE µg-g-1
0.0	0.0	0.0	0.1	0.0	0.0	0.0	<0.00384	<0.0584	<0.00199	<0.00836	<0.00417	<0.00885	0.0	0.0	<0.00208	<0.0335	0.1	0.3	0.2	0.1	0.0	0.3
0.0	0.0	0.0	0.1	0.0	0.0	<0.0171	<0.011	<0.0678	<0.00236	0.0	<0.00248	<0.0075	<0.00236	<0.0171	<0.00594	0.0	0.1	0.3	0.2	0.1	0.0	0.3
0.0	0.0	0.0	0.1	0.0	0.0	0.0	<0.00475	<0.0344	<0.00246	<0.0207	<0.00258	<0.0133	<0.00545	<0.014	<0.00257	<0.0297	0.1	0.3	0.2	0.1	0.0	0.3
0.0	0.0	0.0	0.1	0.0	<0.0155	<0.0366	<0.0108	<0.0393	<0.00812	<0.038	<0.00266	<0.00804	<0.00354	<0.0184	<0.00928	<0.0227	0.2	0.3	0.1	0.1	0.0	0.2
10.0	<0.018	0.8	1.0	0.1	0.7	0.5	0.1	0.8	0.1	1.1	0.2	0.8	0.1	0.8	0.1	0.1	<0.0115	1.5	2.6	2.6	2.0	7.2
10.8	0.0	0.8	0.9	0.2	0.9	0.3	0.1	0.8	0.2	1.1	0.3	0.9	0.1	0.7	0.1	0.0	<0.0139	1.7	2.7	2.6	2.1	7.4
10.9	<0.0164	0.9	0.9	0.2	0.9	0.2	0.1	0.8	0.2	1.2	0.2	0.9	0.1	0.7	0.1	0.0	<0.00389	1.6	2.9	2.5	2.0	7.3
11.4	0.0	0.8	1.0	0.2	0.8	0.3	0.1	0.8	0.2	1.2	0.3	0.8	0.1	0.8	0.1	<0.0226	<0.00664	1.5	2.8	2.7	2.1	7.6
12.3	<0.0196	0.9	1.0	0.2	0.9	0.3	0.2	0.8	0.2	1.3	0.3	1.0	0.1	0.9	0.1	<0.0245	<0.00597	1.6	3.1	2.8	2.5	8.3
9.2	<0.0734	0.5	0.4	0.1	0.6	0.3	0.1	0.6	0.1	1.0	0.2	0.7	0.1	0.6	0.1	<0.0553	<0.0332	1.8	1.5	2.2	1.8	5.5
10.9	<0.0357	0.9	1.1	0.2	0.8	0.2	0.1	0.8	0.2	1.2	0.3	1.0	0.1	0.8	0.1	<0.072	<0.00659	1.6	2.9	2.5	2.3	7.8
11.8	<0.0234	0.8	0.9	0.1	0.8	0.2	0.1	1.0	0.2	1.3	0.3	1.1	0.1	0.9	0.2	0.1	<0.0122	1.9	2.7	2.7	2.6	7.9
9.7	<0.0169	0.8	1.1	0.1	0.8	0.3	0.1	0.9	0.1	1.0	0.2	0.7	0.1	0.7	0.1	0.0	<0.00638	1.3	2.7	2.4	1.8	6.9
8.0	<0.0275	0.7	0.8	0.1	0.5	0.3	0.1	0.7	0.1	1.1	0.2	0.6	0.1	0.5	0.1	<0.0512	<0.0136	1.1	2.2	2.3	1.5	6.0
8.4	0.0	0.7	0.9	0.1	0.6	0.2	0.1	0.6	0.1	0.9	0.2	0.7	0.1	0.6	0.1	<0.0134	<0.00433	1.0	2.3	1.9	1.6	5.8
10.1	<0.0195	0.8	1.0	0.1	0.7	0.2	0.1	0.8	0.1	1.0	0.2	0.8	0.1	0.7	0.1	0.0	<0.0167	1.3	2.7	2.3	1.9	6.9
10.7	<0.0255	0.9	1.2	0.2	0.8	0.3	0.1	0.8	0.1	1.0	0.2	0.8	0.1	0.7	0.1	0.0	0.0	1.2	3.0	2.3	1.9	7.3
10.8	<0.0215	0.9	1.0	0.2	0.7	0.3	0.2	0.7	0.1	1.0	0.2	0.8	0.1	0.7	0.1	<0.0162	<0.0124	1.3	2.8	2.3	1.9	7.1
10.6	<0.012	0.9	1.2	0.2	0.8	0.3	0.1	0.7	0.1	1.0	0.3	0.8	0.1	0.7	0.1	<0.0222	<0.00605	1.1	3.0	2.2	1.9	7.1
10.7	<0.014	0.8	1.1	0.2	0.8	0.3	0.1	0.7	0.1	1.1	0.3	0.8	0.1	0.7	0.1	<0.018	<0.00526	1.3	2.8	2.4	2.0	7.3
10.7	0.0	0.8	1.2	0.2	0.8	0.3	0.1	0.7	0.1	1.1	0.3	0.9	0.1	0.7	0.1	<0.0307	<0.00449	1.2	3.0	2.3	2.0	7.3
11.6	<0.0164	0.9	1.1	0.2	0.8	0.3	0.1	0.7	0.2	1.1	0.3	0.9	0.1	0.8	0.1	<0.0269	<0.00889	1.5	3.0	2.4	2.2	7.7
10.8	<0.0153	0.9	1.3	0.2	0.8	0.3	0.1	0.6	0.1	1.0	0.2	0.7	0.1	0.6	0.1	<0.0196	<0.0082	1.3	3.1	2.2	1.8	7.1
14.3	<0.0683	0.9	0.9	0.2	1.0	0.3	0.2	1.0	0.2	1.3	0.3	1.0	0.2	0.9	0.1	<0.0687	0.0	1.9	3.0	3.0	2.5	8.4
10.9	<0.0153	0.9	1.1	0.2	0.7	0.3	0.1	0.8	0.1	1.1	0.2	0.8	0.1	0.6	0.1	<0.0137	<0.0101	1.3	2.9	2.4	1.9	7.2
4.6	<0.0325	1.1	2.4	0.5	2.5	1.0	0.4	1.0	0.2	1.3	0.3	0.7	0.1	0.6	0.1	0.3	0.0	0.0	6.5	3.8	1.8	12.1
5.0	<0.203	1.3	2.3	0.6	2.5	0.7	0.4	1.0	0.2	1.5	0.3	1.0	0.1	0.7	0.1	<0.267	<0.0809	<0.0554	6.7	3.8	2.2	12.7
3.6	0.4	4.4	7.0	0.5	2.5	<1.34	0.7	1.6	<0.101	1.0	<0.121	0.8	<0.101	<0.45	<0.0869	<0.577	<0.203	<0.175	14.3	4.2	1.3	19.9
2.8	<0.373	1.0	1.9	0.2	0.4	1.5	0.4	0.8	0.1	1.0	<0.184	0.7	<0.157	0.5	0.1	<0.505	<0.0961	<0.13	3.5	3.8	1.5	8.8
2.4	0.1	5.2	8.8	0.7	3.4	0.8	0.3	0.7	0.1	0.7	0.1	0.3	0.1	0.3	0.1	0.2	0.0	<0.0166	18.1	2.6	0.9	21.5
1.7	0.0	5.6	9.2	0.7	3.3	0.8	0.3	0.6	0.1	0.4	0.1	0.3	0.0	0.3	0.0	0.3	0.0	<0.00992	18.8	2.1	0.7	21.6
3.1	<0.0879	5.6	10.0	0.9	3.2	1.0	0.3	0.7	0.2	1.0	0.2	0.6	0.1	0.4	<0.0392	0.2	0.1	<0.035	19.7	3.2	1.3	24.2
3.2	0.1	2.6	5.8	0.4	2.2	0.9	0.3	0.6	0.1	0.9	0.2	0.4	0.0	0.5	0.1	0.1	0.0	0.0	11.0	2.8	1.2	15.0
3.4	0.1	1.8	5.7	0.3	1.6	0.8	0.3	0.7	0.1	0.9	0.2	0.4	0.1	0.5	0.1	0.1	0.0	0.0	9.4	2.7	1.2	13.3
4.5	0.0	0.9	3.1	0.4	1.8	0.6	0.3	1.0	0.2	1.2	0.2	0.7	0.1	0.6	0.1	0.2	<0.0178	0.0	6.2	3.3	1.7	11.2
15.5	<0.0484	0.4	4.9	0.2	1.2	0.3	0.1	0.6	0.1	1.0	0.3	1.1	0.2	1.0	0.1	9.7	0.0	0.1	6.7	2.1	2.7	11.5
20.9	<0.0462	0.5	6.6	0.3	1.5	0.5	0.2	1.3	0.2	1.6	0.5	1.5	0.2	1.5	0.3	10.0	0.1	0.1	9.0	3.8	3.9	16.6
27.6	<0.0527	0.6	5.6	0.3	1.9	0.5	0.3	1.8	0.3	2.0	0.6	1.9	0.3	2.1	0.4	9.8	0.1	0.1	8.4	4.9	5.3	18.6
8.0	<0.0999	2.4	0.0	0.4	2.3	0.6	0.2	0.9	0.1	1.0	0.2	0.6	0.1	0.6	0.1	1.4	<0.0154	0.2	5.2	2.8	1.6	9.5

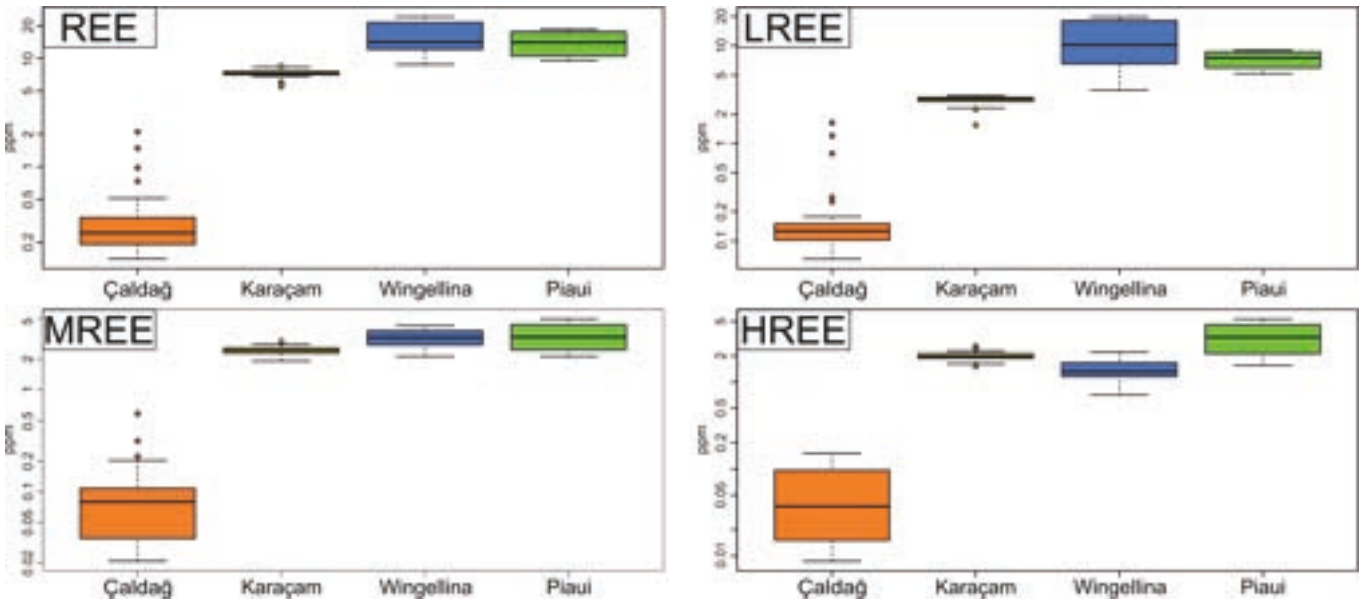

Appendix C. Box and whisker plots showing the REE, LREE, MREE and HREE concentrations by LA-ICP-MS of the studied iron-(oxy)-hydroxides.

References

Aiglsperger, T., Proenza, J.A., Zaccarini, F., Lewis, J.F., Garuti, G., Labrador, M., Longo, F., 2015. Platinum group minerals (PGM) in the Falcondo Ni laterite deposit, Loma Caribe peridotite (Dominican Republic). Mineral. Deposita 50, 105–123. https://doi.org/10.1007/s00126-014-0520-9.

Aiglsperger, T., Proenza, J.A., Lewis, J.F., Labrador, M., Svojtka, M., Rojas-Puròn, A., Longo, F., Ďurišová, J., 2016. Critical metals (REE, Sc, PGE) in Ni laterites from Cuba and the Dominican Republic. Ore Geol. Rev. 73, 127–147. https://doi.org/10.1016/j.oregeorev.2015.10.010.

Ajouyed, O., Hurel, C., Ammari, M., Allal, L.B., Marmier, N., 2010. Sorption of Cr (VI) onto natural iron and aluminium (oxy) hydroxides: effects of pH, ionic strength and initial concentration. J. Hazard. Mater. 174, 616–622. https://doi.org/10.1016/j.jhazmat.2009.09.096.

Akcil, A., Akhmadiyeva, N., Abdulvaliyev, R., Meshram, A.P., 2018. Overview on extraction and separation of rare earth elements from red mud: focus on scandium. Miner. Process. Extr. Metall. Rev. 39, 145–151. https://doi.org/10.1080/08827508.2017.1288116.

Al-Khirbash, S.A., 2015. Genesis and mineralogical classification of Ni-laterites Oman Mountains. Ore Geol. Rev. 65, 199–212. https://doi.org/10.1016/j.oregeorev.2014.09.022.

Al-Khirbash, S.A., 2016. Geology, mineralogy, and geochemistry of low-grade Ni-lateritic soil (Oman Mountains, Oman). Geochemistry 76, 363–381. https://doi.org/10.1016/j.chemer.2016.08.002.

Alvarez, M., Rueda, E.H., Sileo, E.E., 2007. Simultaneous incorporation of Mn and Al in the goethite structure. Geochim. Cosmochim. Acta 71, 1009–1020. https://doi.org/10.1016/j.gca.2006.11.012.

Anand, R.R., Gilkes, R.J., 1987. Iron oxides in lateritic soils from Western Australia. Eur. J. Soil Sci. 38, 607–622. https://doi.org/10.1111/j.1365-2389.1987.tb02158.x.

Andersen, J.C.Ø., Rollinson, G.K., Snook, B., Herrington, R., Fairhurst, R.J., 2009. Use of QEMSCAN® for the characterization of Ni-rich and Ni-poor goethite in laterite ores. Min. Eng. 22, 1119–1129. https://doi.org/10.1016/j.mineng.2009.03.012.

Antelo, J., Avena, M., Fiol, S., Lopez, R., Arce, F., 2005. Effects of pH and ionic strength on the adsorption of phosphate and arsenate at the goethite-water interface. J. Colloid Interface Sci. 285, 476–486. https://doi.org/10.1016/j.jcis.2004.12.032.

Asselin, A.E., 2011. Thermochemistry of the Fe, Ni and Co-NH_3-H_2O systems as they relate to the Caron process: a review. Miner. Metall. Process. 28, 169–175. https://doi.org/10.1007/bf03402448.

Audet, M.A., 2008. Le massif du Koniambo, Nouvelle-Calédonie: Formation et obduction d'un complexe ophiolitique du type SSZ. Enrichissement en nickel, cobalt et scandium dans les profils résiduels. PhD thesis (in French), pp. 327.

Avias, J., 1967. Overthrust structure of the main ultrabasic New Caledonian massives. Tectonophysics 4, 531–541. https://doi.org/10.1016/0040-1951(67)90017-0.

Ballantyne, P.D., 1991. Petrological constraints upon the provenance and genesis of the East Halmahera Ophiolite. Orogenesis in action. J. South East Asian Earth Sci. 6, 259–269. https://doi.org/10.1016/0743-9547(91)90072-6.

Bárdossy, G., Aleva, G.J.J., 1990. In: Lateritic bauxites. Elsevier, Amsterdam, p. 624.

Becquer, T., Quantin, C., Rotte-Capet, S., Ghanbaja, J., Mustin, C., Herbillon, A.J., 2006. Sources of trace metals in Ferralsols in New Caledonia. Eur. J. Soil Sci. 57, 200–213. https://doi.org/10.1111/j.1365-2389.2005.00730.x.

Bekker, A., Planavsky, N.J., Krapež, B., Rasmussen, B., Hofmann, A., Slack, J.F., Rouxel, O.J., Konhauser, K.O., 2014. Iron formations: their origins and implications for ancient seawater chemistry. Treat. Geochem. (Second Edition) 9, 561–628. https://doi.org/10.1016/B978-0-08-095975-7.00719-.

Bekker, A., Slack, J.F., Planavsky, N., Krapež, B., Hofmann, A., Konhauser, K.O., Rouxel, J., 2010. Iron formation: the sedimentary product of the complex interplay among mantle, tectonic, oceanic, and biospheric processes. Econ. Geol. 105, 467–508. https://doi.org/10.2113/gsecongeo.105.3.467.

Berger, V.I., Singer, D.A., Bliss, J.D., Moring, B.C., 2011. Ni-Co laterite deposits of the world; database and grade and tonnage models: U.S.G.S. Open-File Report 1058, p. 1–30. http://pubs.usgs.gov/of/2011/1058/.

Beukes, J., Giesekke, E., Elliott, W., 2000. Nickel retention by goethite and hematite. Miner. Eng. 13, 1573–1579. https://doi.org/10.1016/S0892-6875(00)00140-0.

Bolanz, R.M., Kiefer, S., Göttlicher, J., Steininger, R., 2018. Hematite (α-Fe_2O_3). A potential Ce^{4+} carrier in red mud. Sci. Total Environ. 622–623, 849–860. https://doi.org/10.1016/j.scitotenv.2017.12.043.

Boni, M., Large, D., 2003. Nonsulfide zinc mineralization in Europe: an overview. Econ. Geol. 98, 715–729. https://doi.org/10.2113/gsecongeo.98.4.715.

Borra, C.R., Pontikes, Y., Binnemans, K., Van Gerven, T., 2015. Leaching of rare earths from bauxite residue (red mud). Miner. Eng. 76, 20–27. https://doi.org/10.1016/j.mineng.2015.01.005.

Borra, C.R., Mermans, J., Blanpain, B., Pontikes, Y., Binnemans, K., Van Gerven, T., 2016a. Selective recovery of rare earths from bauxite residue by combination of sulfation, roasting and leaching. Min. Eng. 92, 151–159. https://doi.org/10.1016/j.mineng.2016.03.002.

Borra, C.R., Blanpain, B., Pontikes, Y., Binnemans, K., Van Gerven, T., 2016b. Recovery of rare earths and other valuable metals from bauxite residue (red mud): a review. J. Sustainability Metall. 2, 365–386. https://doi.org/10.1007/s40831-016-0068-2.

Brand, N.W., Butt, C.R.M., Hellsten, K.J., 1996. Structural and lithological controls in the formation of the Cawse nickel laterite deposits, Western Australia - implications for supergene ore formation and exploration in deeply weathered terrains. In: E.J. Grimsey and I. Neuss (Editors), Nickel '96. Conference Proceedings Kalgoorlie, Australian Institute of Mining and Metallurgy, Publication 6/96, 185-190.

Brand, N.W., Butt, C.R.M., Elias, M., 1998. Nickel laterites-Classification and features. AGSO J. Aust. Geol. Geophys. 17 (4), 81–88.

Butt, C.R.M., Cluzel, D., 2013. Nickel laterite ore deposits: Weathered serpentinites. Elements 9, 123–128. https://doi.org/10.2113/gselements.9.2.123.

Carvalho-e-Silva, M.L., Ramos, A.Y., Nogueira Tolentino, H.C., Enzweiler, J., Netto, S.M., do Carmo Martins Alves, M., 2003. Incorporation of Ni into natural goethite: an investigation by X-ray absorption spectroscopy. Am. Min. 88, 876–882. https://doi.org/10.2138/am-2003-5-617.

Cathelineau, M., Myagkiy, A., Quesnel, B., Boiron, M.-C., Gautier, P., Boulvais, P., Ulrich, M., Truche, L., Golfier, F., Drouillet, M., 2017. Multistage crack seal vein and hydrothermal Ni enrichment in serpentinized ultramafic rocks (Koniambo massif, New Caledonia). Mineral. Deposita 52, 945–960. https://doi.org/10.1007/s00126-016-0695-3.

Chassé, M., Griffin, W.L., O'Reilly, S.Y., Calas, G., 2017. Scandium speciation in a world-class lateritic deposit. Geochem. Persp. Let. 3, 105–114. https://doi.org/10.7185/geochemlet.1711.

Chassé, M., Griffin, W.L., O'Reilly, S.Y., Calas, G., 2019. Australian laterites reveal mechanisms governing scandium dynamics in the critical zone. Geochim. Cosmochim. Acta 260, 292–310. https://doi.org/10.1016/j.gca.2019.06.036.

Chavez, X.W., 2000. Supergene oxidation of copper deposits: Zoning and distribution of copper oxide minerals. Soc. Econ. Geol. Newsletter 41, 10–21.

Chen, T.T., Dutrizac, J.E., Krause, E., Osborne, R., 2004. Mineralogical characterization of nickel laterites from New Caledonia and Indonesia. In: International Laterite Nickel Symposium. Proceedings of Symposium TMS Annual Meeting, Charlotte, NC, United States, pp. 79–99.

Childs, C.W., 1992. Ferrihydrite: a review of structure, properties and occurrence in relation to soils. Z. Pflanz. Bodenkunde 155, 441–448. https://doi.org/10.1002/jpln.19921550515.
Cluzel, D., Aitchison, J.C., Picard, C., 2001. Tectonic accretion and underplating of mafic terranes in the Late Eocene intraoceanic fore-arc of New Caledonia (Southwest Pacific): Geodynamic implications. Tectonophysics 340 (1–2), 23–59. https://doi.org/10.1016/S0040-1951(01)00148-2.
Cluzel, D., Jourdan, F., Meffre, S., Maurizot, P., Lesimple, S., 2012. The metamorphic sole of New Caledonia ophiolite: $^{40}Ar/^{39}Ar$, U-Pb, and geochemical evidence for subduction inception at spreading ridge. Tectonics 31, 3, TC3016. https://doi.org/10.1029/2011TC003085.
Cornell, R.M., Giovanoli, R., Schindler, P.W., 1987. Effect of silicate species on the transformation of ferrihydrite into goethite and hematite in alkaline media. Clays Clay Miner. 35 (1), 21–28. https://doi.org/10.1346/CCMN.1987.0350103.
Colin, D.N., Trescases, J-J., Melfi, A.J., 1990. Lateritic weathering of pyroxenites at Niquelandia, Goias, Brazil; the supergene behavior of nickel. Econ. Geol. 85 (5), 1010–1023. https://doi.org/10.2113/gsecongeo.85.5.1010.
Cornell, R.M., Giovanoli, R., 1989. Effect of cobalt on the formation of crystalline iron oxides from ferrihydrite in alkaline media. Clays Clay Miner. 37, 65–70. https://doi.org/10.1346/CCMN.1989.0370108.
Cornell, R.M., Schwertmann, U., 2003. The Iron Oxides: Structure, Properties, Reactions, Occurrences and Uses, scond ed. Wiley-VCH, Weinheim.
Cudennec, Y., Lecerf, A., 2006. The transformation of ferrihydrite into goethite or hematite, revisited. J. Solid State Chem. 179, 716–722. https://doi.org/10.1016/j.jssc.2005.11.030.
Dale, I.M., Henderson, P., 1972. The partitioning of transition elements in phenocryst-bearing basalts and their implication about melt structure. In: 24th Int Geol Congr Section, pp. 105–111.
Dalvi, A.D., Bacon, W.G., Osborne, R.C., 2004. The past and the future of nickel laterites. PDAC 2004 International Convention — Trade Show and Investors Exchange.
Davis, C.C., Chen, H.-W., Edwards, M., 2002. Modeling silica sorption to iron hydroxide. Environ. Sci. Technol. 36, 582–587. https://doi.org/10.1021/es010996t.
Davris, P., Balomenos, E., Panias, D., Paspaliaris, I., 2016. Selective leaching of rare earth elements from bauxite residue (red mud), using a functionalized hydrophobic ionic liquid. Hydrometallurgy 164, 125–135. https://doi.org/10.1016/j.hydromet.2016.06.012.
Davris, P., Stopic, S., Balomenos, E., Panias, D., Paspaliaris, I., Friedrich, B., 2017. Leaching of rare earth elements from eudialyte concentrate by suppressing silica gel formation. Miner. Eng. 108, 115–122. https://doi.org/10.1016/j.mineng.2016.12.011.
Deady, É.A., Mouchos, E., Goodenough, K., Williamson, B.J., Wall, F., 2016. A review of the potential for rare-earth element resources from European red muds: examples from Seydişehir, Turkey and Parnassus-Giona, Greece. Mineral. Mag. 80, 43–61. https://doi.org/10.1180/minmag.2016.080.052.
de Oliveira, S.M.B., Trescases, J.J., Melfi, A.J., 1992. Lateritic nickel deposits of Brazil. Mineral. Deposita 27, 137–146. https://doi.org/10.1007/BF00197099.
Dimalanta, C.B., Faustino-Eslava, D.V., Gabo-Ratio, J.A.S., Marquez, E.J., Padrones, J.T., Payot, B.D., Queaño, K.L., Ramos, N.T., Yumul Jr., G.P., 2020. Characterization of the proto-Philippine Sea Plate: evidence from the emplaced oceanic lithospheric fragments along eastern Philippines. Geosci. Front. 11, 3–21. https://doi.org/10.1016/j.gsf.2019.01.005.
Di Maria, A., Van Acker, K., 2018. Turning industrial residues into resources: an environmental impact assessment of goethite valorization. Engineering 4, 421–429. https://doi.org/10.1016/j.eng.2018.05.008.
Dublet, G., Juillot, F., Morin, G., Fritsch, E., Fandeur, D., Ona-Nguema, G., Brown Jr., G. E., 2012. Ni speciation in a New Caledonian lateritic regolith: a quantitative X-ray absorption spectroscopy investigation. Geochim. Cosmochim. Acta 95, 1–40. https://doi.org/10.1016/j.gca.2012.07.03.
Dublet, G., Juillot, F., Morin, G., Fritsch, E., Fandeur, D., Brown Jr, G.E., 2015. Goethite aging explains Ni depletion in upper units of ultramafic lateritic ores from New Caledonia. Geochim. Cosmochim. Acta 160, 1–15. https://doi.org/10.1016/j.gca.2017.07.010.
Dublet, G., Juillot, F., Brest, J., Noël, V., Fritsch, E., Proux, O., Olivi, L., Ploquin, F., Morin, G., 2017. Vertical changes of the Co and Mn speciation along a lateritic regolith developed on peridotites (New Caledonia). Geochim. Cosmochim. Acta 217, 1–15. https://doi.org/10.1016/j.gca.2017.07.010.
Einaudi, M.T., Burt, D.M., 1982. Introduction, terminology, classification, and composition of skarn deposits. Econ. Geol. 77, 745–754. https://doi.org/10.2113/gsecongeo.77.4.745.
Elias, M., Donaldson, M.J., Giorgetta, N.E., 1981. Geology, mineralogy, and chemistry of lateritic nickel-cobalt deposits near Kalgoorlie, Western Australia. Econ. Geol. 76, 1775–1783. https://doi.org/10.2113/gsecongeo.76.6.1775.
Elias, M., 2002. Nickel laterite deposits — geological overview, resources and exploitation. In: Genesis and Exploitation: CODES Special Publication. Centre for Ore Deposit Research, University of Tasmania, pp. 205–220.
Elias, M., 2006. Lateritic nickel mineralization of the Yilgarn Craton. Soc. Econ. Geol., Spec. Publ. 13, 195–210. https://doi.org/10.5382/SP.13.07.
Eliopoulos, D.G., Economou-Eliopoulos, M., 2000. Geochemical and mineralogical characteristics of Fe–Ni and bauxitic-laterite deposits of Greece. Ore Geol. Rev. 16, 41–58. https://doi.org/10.1016/S0169-1368(00)00003-2.
Eliopoulos, D.G., Economou-Eliopoulos, M., 2010. Arsenic Distribution in Laterites of the Balkan Peninsula. Scientific Annals, School of Geology, Aristotle University of Thessaloniki Proceedings of the XIX CBGA Congress, Thessaloniki, Greece. Special Volume. 325-332. https://doi.org/10.1016/j.oregeorev.2012.05.008.
Eliopoulos, D.G., Economou-Eliopoulos, M., Apostolikas, A., Golightly, J.P., 2012. Geochemical features of nickel-laterite deposits from the Balkan Peninsula and Gordes, Turkey: the genetic and environmental significance of arsenic. Ore Geol. Rev. 48, 413–427. https://doi.org/10.1016/j.oregeorev.2012.05.008.
Eliopoulos, D.G., Economou, G., Tzifas, I., Papatrechas, C., 2014. The potential of rare earth elements in Greece. Proceedings of the ERES: First European Rare Earth Resources Conference, Milos, Greece.
Faivre, D., Frankel, B.R., 2016. Iron Oxides: From Nature to Applications. Wiley-VCH, Weinheim.
Fan, R., Gerson, A.R., 2011. Nickel geochemistry of a Philippine laterite examined by bulk and microprobe synchrotron analyses. Geochim. Cosmochim. Acta 75, 6400–6415. https://doi.org/10.1016/j.gca.2011.08.003.
Fan, R., Gerson, A.R., 2013. Mineralogical characterisation of Indonesian laterites prior to and post atmospheric leaching. Hydrometallurgy 134–135, 102–109. https://doi.org/10.1016/j.hydromet.2013.02.004.
Fandeur, D., Julliot, F., Morin, G., Olivi, L., Cognigni, A., Ambrosi, J.-P., Guyot, F., Fritsch, E., 2009. Synchrotron-based speciation of chromium in an Oxisol from New Caledonia: importance of secondary Fe-oxyhydroxides. Am. Min. 94 (5–6), 710–719. https://doi.org/10.2138/am.2009.3073.
Farrokhpay, S., Cathelineau, M., Blancherb, S.B., Laugierb, O., Filippova, L., 2019. Characterization of Weda Bay nickel laterite ore from Indonesia. J. Geochem. Explor. 196, 270–281. https://doi.org/10.1016/j.gexplo.2018.11.002.
Fendorf, S., Eick, M.J., Grossl, P., Sparks, D.L., 1997. Arsenate and chromate retention mechanisms on goethite. 1: surface structure. Environ. Sci. Technol. 31, 315–320. https://doi.org/10.1021/es950653t.
Fleischer, M., Chao, G.Y., Kato, A., 1975. New mineral names. Am. Mineral. 60, 485–486.
Fonseca, E., Zelepugin, V.N., Heredia, M., 1985. Structure of the ophiolite association of Cuba. Geotectonic 19, 321–329.
Fortin, D., Langley, S., 2005. Formation and occurrence of biogenic iron-rich minerals. Earth-Sci. Rev. 72, 1–19. https://doi.org/10.1016/j.earscirev.2005.03.002.
Freyssinet, P., Butt, C.R.M., Morris, R.C., Piantone, P., 2005. Ore-forming processes related to lateritic weathering. Econ. Geol., 100th Anniversary Volume. pp. 681–722.
Fu, W., Yang, J.W., Yang, M.L., Pang, B.C., Liu, X.J., Niu, H.J., Huang, X.R., 2014. Mineralogical and geochemical characteristics of a serpentinite-derived lateritic profile from East Sulawesi, Indonesia: implications for the lateritization process and Ni supergene enrichment in the tropical rainforest. J. Asian Earth Sci. 93, 74–88. https://doi.org/10.1016/j.jseaes.2014.06.030.
Fu, W., Zhanga, Y., Panga, C., Zenga, X., Huanga, X., Yanga, M., Shaoa, Y., Lin, H., 2018. Garnierite mineralization from a serpentinite-derived lateritic regolith, Sulawesi Island, Indonesia: mineralogy, geochemistry and link to hydrologic flow regime. J. Geochem. Explor. 188, 240–256. https://doi.org/10.1016/j.gexplo.2018.01.022.
Gamaletsos, P.N., Kalatha, S., Godelitsas, A., Economou-Eliopoulos, M., Göttlicher, J., Steininger, R., 2018. Arsenic distribution and speciation in the bauxitic Fe-Ni-laterite ore deposit of the Patitira mine, Lokris area (Greece). J. Geochem. Explor. 194, 189–197. https://doi.org/10.1016/j.gexplo.2018.07.018.
Gaudin, A., Decarreau, A., Noack, Y., Grauby, O., 2005. Clay mineralogy of the nickel laterite ore developed from sepentinised peridotites at Murrin, Western Australia. Austr. J. Earth Sci. 52, 231–241. https://doi.org/10.1080/08120090500139406.
Georgiou, D., Papangelakis, V.G., 1998. Sulphuric acid pressure leaching of limonitic laterite: chemistry and kinetics. Hydrometallurgy 49, 23–46. https://doi.org/10.1016/S0304-386X(98)00023-1.
Gerth, J., 1990. Unit-cell dimensions of pure and trace metal-associated goethites. Geochim. Cosmochim. Acta 54, 363–371. https://doi.org/10.1016/0016-7037(90)90325-F.
Gerth, J., Brümmer, G.W., Tiller, K.G., 1993. Retention of Ni, Zn and Cd by Si-associated goethite. J. Plant Nutr. Soil Sci. 156, 123–129. https://doi.org/10.1002/jpln.19931560205.
Gleeson, S.A., Butt, C., Elias, M., 2003. Nickel laterites: a review. Soc. Econ. Geol. Newsl. 54, 9–16.
Gleeson, S.A., Herrington, R.J., Durango, J., Velásquez, C.A., Koll, G., 2004. The mineralogy and geochemistry of the Cerro Matoso SA Ni laterite deposit, Montelíbano, Colombia. Econ. Geol. 99, 1197–1213. https://doi.org/10.2113/gsecongeo.99.6.1197.
Glennie, K.W., Boeuf, M.G.A., Hughes, C.W., Moody-Stuart, M., Pilaar, W.F.H., Reinhardt, B.M., 1973. Late Cretaceous nappes in the Oman Mountains and their geologic evolution. Am. Assoc. Petrol. Geol. Bull. 57, 5–27.
Golightly, J.P., 1981. Nickeliferous laterite deposits. Econ. Geol., 75th Anniversary Volume, pp. 710–735.
Golightly, J.P., 2010. Progress in understanding the evolution of nickel laterites. In: Goldfarb, R.J., Marsh, E.E., Monecke, T. (Eds.), The challenge of finding new mineral resources—Global metallogeny, innovative exploration, and new discoveries: Soc. Econ. Geol., Special Publication, pp. 451–485.
Golightly, J.P., Arancibia, O.N., 1979. The chemical composition and infrared spectrum of nickel and iron-substituted serpentine from a nickeliferous laterite profile, Soroako, Indonesia. Can. Mineral. 17, 719–728.
Granados-Correa, F., Corral-Capulin, N.G., Olguin, M.T., Acosta-Leon, C.E., 2011. Comparison of the Cd(II) adsorption processes between boehmite (gamma-AlOOH) and goethite (alpha-FeOOH). Chem. Engin. J. 171, 1027–1034. https://doi.org/10.1016/j.cej.2011.04.055.
Gray, J.D., Schorin, K.H., Butt, C.R.M., 1996. Mineral associations of platinum and palladium in lateritic regolith, Ora Banda Sill, Western Australia. J. Geochem. Explor. 57, 245–255. https://doi.org/10.1016/S0375-6742(96)00040-4.
Gualtieri, A.F., Venturelli, P., 1999. In situ study of the goethite-hematite phase transformation by real time synchrotron powder diffraction. Am. Min. 84, 895–904. https://doi.org/10.2138/am-1999-5-624.
Haldemann, E.G., Buchan, R., Blowes, J.H., Chandler, T., 1979. Geology of lateritic nickel deposits, Dominican Republic. Intern. Laterite Symp. 4, 57–84.

Hallberg, K.B., Grail, B.M., du Plessis, C.A., Johnson, D.B., 2011. Reductive dissolution of ferric iron minerals: a new approach for bio-processing nickel laterites. Miner. Eng. 24, 620–624. https://doi.org/10.1016/j.mineng.2010.09.005.
Heikoop, J.M., Tsujita, C.J., Risk, M.J., Tomascik, T., Mah, A.J., 1996. Modern iron ooids from a shallow-marine volcanic setting: Mahengetang, Indonesia. Geology 24, 759–762. https://doi.org/10.1130/0091-7613(1996)024<0759:MIOFAS>2.3.CO;2.
Herrington, R., 2012. Potential for cobalt recovery from lateritic ores in Europe. Geophysical Research Abstracts, 14, EGU2012-13888. EGU General Assembly 2012.
Herrington, R., Boni, M., Skarpelis, N., 2007. Palaeoclimate, weathering and ore deposits – a European perspective. In: Proceedings of the Ninth Biennial SGA Meeting, Dublin.
Herrington, R., Kinchington, M., Tavlan, M., Thorne, R. Generation of oxide-type lateritic Ni-Co-Sc profiles: Evidence from Karaçam (Adatepe) deposit Turkey. J. Geochem. Explor. in review.
Herrington, R., Mondillo, N., Boni, M., Thorne, R., Tavlan, M., 2016. Bauxite and nickel-cobalt lateritic deposits of the Tethyan Belt. Soc. Econ. Geol., Inc. Spec. Publ. 19, 349–387.
Himestra, T., Barnett, M., van Riemsdijk, W.H., 2007. Interaction of silicic acid with goethite. L. Colloid. Interface Sci. 310, 8–17. https://doi.org/10.1016/j.jcis.2007.01.065.
Hitzman, M.W., Reynolds, N.A., Sangster, D.F., Allen, C.R., Carman, C.E., 2003. Classification, genesis, and exploration guides for nonsulfide zinc deposits. Econ. Geol. 98, 685–714. https://doi.org/10.2113/gsecongeo.98.4.685.
Ilyas, A., Koike, K., 2012. Geostatistical modeling of ore grade distribution from geomorphic characterization in a laterite nickel deposit. Nat. Resour. Res. 21 (2), 177–191. https://doi.org/10.1007/s11053-012-9170-8.
INSG (International Nickel Study Group) 2021, <https://www.insg.org>, (accessed 08/2021).
Iturralde-Vinent, M.A., Díaz Otero, C., Rodríguez Vega, A., Díaz Martínez, R., 2006. Tectonic implications of paleontologic dating of Cretaceous-Danian sections of Eastern Cuba. Geol. Acta 4, 89–102. https://doi.org/10.1344/105.000000359.
Johan, Z., Ohnenstetter, M., Slansky, E., Barron, L.M., Suppel, D.W., 1989. Platinum mineralization in the Alaskan-type intrusive complexes near fifield, New South Wales, Australia Part 1. Platinum-Group minerals in clinopyroxenites of the Kelvin Grove Prospect, Owendale Intrusion. Miner. Petrol. 40, 289–309. https://doi.org/10.1007/BF01164604.
Johnson, D.B., Grail, B.M., Hallberg, K.B., 2013. A new direction for biomining: extraction of metals by reductive dissolution of oxidised ores. Minerals 3, 49–58. https://doi.org/10.3390/min3010049.
Johnson, D.B., du Plessis, C., 2015. Biomining in reverse gear: using bacteria to extract metals from oxidized ores. Miner. Eng. 75, 2–5. https://doi.org/10.1016/j.mineng.2014.09.024.
Kadarusman, A., Miyashita, S., Maruyama, S., Parkinson, C.D., Ishikawa, A., 2004. Petrology, geochemistry and paleogeographic reconstruction of the East Sulawesi Ophiolite, Indonesia. Tectonophysics 392, 55–83. https://doi.org/10.1016/j.tecto.2004.04.008.
Kar, B.B., Swamy, Y.V., Murthy, B.V.R., 2000. Design of experiments to study the extraction of nickel from lateritic ore by sulphatization using sulphuric acid. Hydrometallurgy 56, 387–394. https://doi.org/10.1016/S0304-386X(00)00086-4.
Kelly, W.C., 1957. Mineralogy of limonite in lead-zinc gossans. Econ. Geol. 52, 536–545. https://doi.org/10.2113/gsecongeo.52.5.536.
Kingston, A.M., Posner, J.P., Quirk, J.P., 1972. Anion adsorption by goethite and gibbsite. I. The role of the proton in determining adsorption envelopes. J. Soil Sci. 23, 177–192. https://doi.org/10.1111/j.1365-2389.1972.tb01652.x.
Klein, C., 2005. Some Precambrian banded iron-formations (BIFs) from around the world: their age, geologic setting, mineralogy, metamorphism, geochemistry, and origins. Am. Min. 90, 1473–1499. https://doi.org/10.2138/am.2005.1871.
Kneeshaw, M., Kepert, D.A., 2002. Genesis of High-grade hematite orebodies of the Hamersley Province, Western Australia – a Discussion. Econ. Geol. 97, 173. https://doi.org/10.2113/gsecongeo.97.1.173.
Krüger, J.C., James, R.H., Herrington, R., Pearce, C.R., Roberts, S., 2017. Behaviour of Cr and its isotopes in laterites and implications for Ni laterite formation. Abstract, Goldschmidt Conference 2017.
Krüger, J.C., 2019. The behaviour of chromium and its isotopes in nickel laterites. University of Southampton, Doctoral Thesis, 314 pp.
Kyle, J.H., 2010. Nickel laterite processing technologies-where to next? In: ALTA 2010 Nickel/Cobalt/Copper Conference, 24-27 May, Perth, Western Australia.
Lambiv Dzemua, G., Gleeson, S.A., 2012. Petrography, mineralogy, and geochemistry of the Nkamouna serpentinite: Implications for the formation of the Cobalt-Manganese Laterite Deposit, Southeast Cameroon. Econ. Geol. 107 (1), 25–41. https://doi.org/10.2113/econgeo.107.1.25.
Lambiv Dzemua, G., Gleeson, S.A., Schofield, P.F., 2013. Mineralogical characterization of the Nkamouna Co–Mn laterite ore, southeast Cameroon. Mineral. Deposita 48 (2), 155–171. https://doi.org/10.1007/s00126-012-0426-3.
Large, D., 2001. The geology of non-sulphide zinc deposits – an overview. Erzmetall 54, 264–276.
Lavaut, W., 1998. Tendencias geológicas del intemperismo de las rocas ultramáficas en Cuba oriental. Rev. Minera Geol. 15, 9–16.
Levard, C., Borschneck, D., Grauby, O., Rose, J., Ambrosi, J.-P., 2018. Goethite, a tailor-made host for the critical metal scandium: the FexSc(1-x)OOH solid solution. Geochem. Perspect. Lett. 9 https://doi.org/10.7185/geochemlet.1832.
Lewis, J.F., Jiménez, J.G., 1991. Duarte Complex in the La Vega-Jarabacoa-Janico area, central Hispaniola; Geologic and geochemical features of the sea floor during the early stages of arc evolution. Geol. Soc. Am. Spec. Pap. 262, 115–141. https://doi.org/10.1130/SPE262-p115.
Lewis, J.F., Escuder-Viruete, J., Hernaiz-Huerta, P.P., Gutiérrez, G., Draper, G., Pérez-Estaún, A., 2002. Subdivisión geoquímica del arco de Isla Circum-Caribeño, Cordillera Central Dominicana: Implicaciones para la formación, acreción y crecimiento cortical en un ambiente intraoceánico. Acta Geol. Hisp. 37, 81–122.
Lewis, J.F., Draper, G., Proenza, J.A., Espaillat, J., Jiménez, J., 2006. Ophiolite related ultramafic rocks (serpentinites) in the Caribbean region: a review of their occurrence, composition, origin, emplacement and nickel laterite soils. Geol. Acta 4, 237–263. https://doi.org/10.1344/105.000000368.
Linchenat, A., Shirakova, I., 1964. Individual characteristics of nickeliferous iron (laterite) deposits of the northeast part of Cuba (Pinares de Mayari, Nicaro and Moa). In: 24th International Geological Congress, Montreal, Part 14, Section 14, pp. 172–187.
Lindsay, W.L., 1979. In: Chemical equilibria in soils. Wiley Interscience, New York, p. 449.
Lindsley, D.H., 1991. Oxide minerals: Petrologic and magnetic significance. Rev. Mineral. Mineral. Soc. Am. 25, 509.
Lithgow, E.W., 1993. Nickel laterites of central Dominican Republic Part I. Mineralogy and ore dressing. In: Reddy, R.G., Weizenbach, R.N. (eds) The Paul E. Queneau Int. Symposium, Extractive Metallurgy of Copper, Nickel and Cobalt, Volume I: Fundamental Aspects. The Minerals, Metals and Materials Society, Portland, 403–425.
Logomerac, V.G., 1971. Distribution of rare-earth and minor elements in some bauxite and red mud produced. In: Proceedings of the Second International Symposium of ICSOBA, Budapest, Hungary, pp. 383–393.
Luxton, T.P., Tadanier, C.J., Eick, M.J., 2006. Mobilization of arsenite by competitive interaction with silicic acid. Soil Sci. Soc. Am. J. 70, 204–214. https://doi.org/10.2136/sssaj2005.0101.
Luxton, T.P., Eick, M.J., Rimstidt, D.J., 2008. The role of silicate in the adsorption/desorption of arsenite on goethite. Chem. Geol. 252, 125–135. https://doi.org/10.1016/j.chemgeo.2008.01.022.
Mackay, A., 1962. β-Ferric oxyhydroxide—akaganéite. Mineral. Mag. J. M. Soc. 33, 270–280. https://doi.org/10.1180/minmag.1962.033.259.02.
Mamindy-Pajany, Y., Hurel, C., Marmier, N., Roméo, M., 2009. Arsenic adsorption onto hematite and goethite. C. R. Chem. 12, 876–881. https://doi.org/10.1016/j.crci.2008.10.012.
Manceau, A., Calas, G., 1985. Heterogeneous distribution of nickel in hydrous silicates from New Caledonia ore-deposits. Am. Mineral. 70, 549–558.
Mano, E., Caner, L., Petit, S., Chaves, A., Mexias, A., 2014. Mineralogical characterization of Ni-bearing smectites from Niquelândia, Brazil. Clays Clay Min. 62, 324–335. https://doi.org/10.1346/CCMN.2014.0620406.
Marchesi, C., Garrido, C.J., Godard, M., Proenza, J.A., Gervilla, F., Blanco-Moreno, J., 2006. Petrogenesis of highly depleted peridotites and gabbroic rocks from the Mayarí – Baracoa Ophiolitic Belt (Eastern Cuba). Contrib. Miner. Petrol. 151, 717–736. https://doi.org/10.1007/s00410-006-0089-0.
Marchesi, C., Garrido, C.J., Godard, M., Belley, F., Ferré, E., 2009. Migration and accumulation of ultra-depleted subduction-related melts in the Massif du Sud ophiolite (New Caledonia). Chem. Geol. 266, 180–195. https://doi.org/10.1016/j.chemgeo.2009.06.004.
Marrero, J., Coto, O., Goldman, S., Graupner, T., Schippers, A., 2015. Recovery of nickel and cobalt from laterite tailings by reductive dissolution under aerobic conditions using Acidithiobacillus species. Environ. Sci. Technol. 49, 6674–6682. https://doi.org/10.1021/acs.est.5b00944.
Martín-Fernández, J.A., Barceló-Vidal, C., Pawlowsky-Glahn, V., 2003. Dealing with zeros and missing values in compositional data sets using nonparametric imputation. Math. Geol. 35, 253–278. https://doi.org/10.1023/A:1023866030544.
Maulana, A., Sanematsu, K., Sakakibara, M., 2016. An Overview on the Possibility of Scandium and REE Occurrence in Sulawesi, Indonesia. Indonesian. J. Geosci. 3, 139–147. https://doi.org/10.17014/ijog.3.2.139-147.
Maurizot, P., Sevin, B., Iseppi, M., 2019. Nickel-bearing laterite deposits in accretionary context and the case of New Caledonia: from the large-scale structure of earth to our everyday appliances. GSA Today 29, 4–10.
McDonald, R.G., Whittington, B.I., 2008. Atmospheric acid leaching of nickel laterites review. Part I. Sulfuric acid technologies. Hydrometallurgy 91, 35–55.
Michel, F.M., Ehm, L., Antao, S.M., Lee, P.L., Chupas, P.J., Liu, G., Strongin, D.R., Schoonen, M.A.A., Phillips, B.L., Parise, J.B., 2007. The structure of ferrihydrite, a nanocrystalline material. Science 316 (5832), 1726–1729. https://doi.org/10.1126/science.1142525.
Mondillo, N., Boni, M., Balassone, G., Joachimski, M., Mormone, A., 2014. The Jabali Nonsulfide Zn-Pb-Ag Deposit, Western Yemen. Ore Geol. Rev. 61, 248–267. https://doi.org/10.1016/j.oregeorev.2014.02.003.
Mondillo, N., Herrington, R., Boyce, A., Wilkinson, J., Santoro, L., Rumsey, M., 2018a. Critical elements in non-sulfide Zn deposits: a reanalysis of the Kabwe Zn-Pb ores (central Zambia). Mineral. Mag. 82 (S1), S89–S114. https://doi.org/10.1180/minmag.2017.081.038.
Mondillo, N., Arfé, G., Herrington, R., Boni, M., Wilkinson, C., Mormone, A., 2018b. Enrichment in supergene settings: evidence from the Cristal nonsulfide Zn prospect, Bongará district, Northern Peru. Mineral. Deposita 53, 155–169. https://doi.org/10.1007/s00126-017-0781-1.
Mondillo, N., Balassone, G., Boni, M., Chelle-Michou, C., Cretella, S., Mormone, A., Putzolu, F., Santoro, L., Scognamiglio, G., Tarallo, M., 2019. Rare Earth Elements (REE) in Al- and Fe-(Oxy)-Hydroxides in bauxites of Provence and Languedoc (Southern France): implications for the potential recovery of REEs as by-products of bauxite mining. Minerals 9, 504. https://doi.org/10.3390/min9090504.
Morikawa, M., 1975. Characteristics of laterite from the Acoje area, Philippines. Kogai Shigen Kenkyusho Iho 5, 33–41.

Morris, R.C., 1985. Genesis of iron ore in banded iron-formation by supergene and supergene-metamorphic processes—a conceptual model. In: Wolf, K.H. (Ed.), Handbook of Strata-bound and Stratiform Ore Deposits. Elsevier, Amsterdam, pp. 73–235.
Morris, R.C., 2002. Genesis of high-grade hematite orebodies of the Hamersley Province, Western Australia—a discussion. Econ. Geol. 97, 177–181. https://doi.org/10.2113/gsecongeo.97.1.177.
Moskalyk, R.R., Alfantazi, A.M., 2002. Nickel laterite processing and electrowinning practice. Min. Eng. 15, 593–605. https://doi.org/10.1016/S0892-6875(02)00083-3.
Murashko, V.I., Lavandero, R.M., 1989. Chromite in the hyperbasite belt of Cuba. Int. Geol. Rev. 31, 90–99. https://doi.org/10.1080/00206818909465864.
Mücke, A., Farshad, F., 2005. Whole-rock and mineralogical composition of Phanerozoic ooidal ironstones: comparison and differentiation of types and subtypes. Ore Geol. Rev. 26, 227–262. https://doi.org/10.1016/j.oregeorev.2004.08.001.
Muñoz, M., Ulrich, M., Cathelineau, M., Mathon, O., 2019. Weathering processes and crystal chemistry of Ni-bearing minerals in saprock horizons of New Caledonia ophiolite. J. Geochem. Exp. 198, 82–99. https://doi.org/10.1016/j.gexplo.2018.12.007.
Myagkiy, A., Truche, L., Cathelineau, M., Golfier, F., 2017. Revealing the conditions of Ni mineralization in the laterite profiles of New Caledonia: insights from reactive geochemical transport modelling. Chem. Geol. 466, 274–284. https://doi.org/10.1016/j.chemgeo.2017.06.018.
Nagano, T., Nakashima, S., Nakayama, S., Senoo, M., 1994. The use of color to quantify the effects of pH and temperature on crystallization kinetics of goethite under highly alkaline conditions. Clays Clay Min. 42, 226–234. https://doi.org/10.1346/CCMN.1994.0420213.
Nahon, D., Paquet, H., Delvigne, J., 1982. Lateritic weathering of ultramafic rocks and the concentration of nickel in the Western Ivory Coast. Econ. Geol. 77, 1159–1175. https://doi.org/10.2113/gsecongeo.77.5.1159.
Ñancucheo, I., Johnson, D.B., 2010. Production of glycolic acid by chemolithotrophic iron- and sulfur-oxidising bacteria and its role in delineating and sustaining acidophilic sulfide mineral-oxidising consortia. Appl. Environ. Microbiol. 76, 461–467. https://doi.org/10.1128/AEM.01832-09.
Norman, R.L., 2014. Incorporation of nickel into synthetic goethites and the stabilisation of mineral precursor phases - implications for natural systems. PhD thesis. University of Loughborough.
Ogura, Y., Hamada, Y., Chiba, J., Baba, R., Ise, K., Saito, I., Tamagawa, T., Kosuge, K., 1983. Mineralogy and geochemistry of pisolites in the nickeliferous laterite deposits in the Rio Tuba mine, Philippines. Kogai Shigen Kenkyusho Iho 13, 25–45.
Önen, A.P., Hall, R., 2000. Sub-ophiolite metamorphic rocks from NW Anatolia, Turkey. J. Metamorph. Geol. 18, 483–495. https://doi.org/10.1046/j.1525-1314.2000.00276.x.
Oxley, A., Smith, M.E., Caceres, O., 2016. Why heap leach nickel laterites? Miner. Eng. 88, 53–60. https://doi.org/10.1016/j.mineng.2015.09.018.
Oze, C., Fendorf, S., Bird, D.K., Coleman, R.G., 2004. Chromium geochemistry in serpentinized ultramafic rocks and serpentine soils from the Franciscan complex of California. Am. J. Sci. 304, 67–101. https://doi.org/10.2475/ajs.304.1.67.
Piga, L., Stoppa, L., Massidda, R., 1995. Recycling of industrial goethite wastes by thermal treatment. Resour. Conserv. Recycl. 14, 11–20. https://doi.org/10.1016/0921-3449(94)00039-8.
Pirard, C., Hermann, J., O'Neill, H.S.C., 2013. Petrology and geochemistry of the crust-mantle boundary in a Nascent Arc, Massif du Sud Ophiolite, New Caledonia, SW Pacific. J. Petrol. 54, 1759–1792. https://doi.org/10.1093/petrology/egt030.
Pelino, M., Cantalini, C., Abbruzzese, C., Plescia, P., 1996. Treatment and recycling of goethite waste arising from the hydrometallurgy of zinc. Hydrometallurgy 40, 25–35. https://doi.org/10.1016/0304-386X(95)00004-Z.
Perelomov, L.V., Pinskiy, D.L., Violante, A., 2011. Effect of organic acids on the adsorption of copper, lead, and zinc by goethite. Eurasian Soil Sci. 44, 22–28. https://doi.org/10.1134/S1064229311010091.
Prinzhofer, A., Nicolas, A., Cassard, D., Moutte, J., Leblanc, M., Paris, J., Rabinowitcz, M., 1980. Structures in the New Caledonia peridotites-gabbros: implications for oceanic mantle and crust. Tectonophysics 69, 85–112. https://doi.org/10.1016/0040-1951(80)90128-6.
Prinzhofer, A., Allègre, C.J., 1985. Residual peridotites and the mechanisms of partial melting. Earth Planet. Sci. Lett. 74, 251–265. https://doi.org/10.1016/0012-821X(85)90025-1.
Proenza, J.A., Gervilla, F., Melgarejo, J.C., Bodinier, J.L., 1999a. Al- and Cr-rich chromitites from the Mayarí-Baracoa Ophiolitic Belt (Eastern Cuba): consequence of interaction between volatile-rich melts and peridotite in suprasubduction mantle. Econ. Geol. 94, 547–566. https://doi.org/10.2113/gsecongeo.94.4.547.
Proenza, J.A., Gervilla, F., Melgarejo, J.C., 1999b. La Moho Transition Zone en el Macizo Ofiolítico Moa–Baracoa: Un ejemplo de interacción magma/peridotite. Rev. Soc. Geol. Esp. 12, 309–327.
Proenza, J.A., Zaccarini, F., Lewis, J.F., Longo, F., Garuti, G., 2007. Chromian spinel composition and the platinum group minerals of the PGE-rich Loma Peguera chromitites, Loma Caribe peridotite, Dominican Republic. Can. Mineral. 45, 631–648. https://doi.org/10.2113/gscanmin.45.3.631.
Putzolu, F., Balassone, G., Boni, M., Maczurad, M., Mondillo, N., Najorka, J., Pirajno, F., 2018. Mineralogical association and Ni-Co deportment in the Wingellina oxide-type laterite deposit (Western Australia). Ore Geol. Rev. 97, 21–34. https://doi.org/10.1016/j.oregeorev.2018.05.005.
Putzolu, F., Boni, M., Mondillo, N., Maczurad, M., Pirajno, F., 2019. Ni-Co enrichment and High-Tech metals geochemistry in the Wingellina Ni-Co oxide-type laterite deposit (Western Australia). J. Geoch. Expl. 196, 282–296. https://doi.org/10.1016/j.gexplo.2018.11.004.
Putzolu, F., Abad, I., Balassone, G., Boni, M., Cappelletti, P., Graziano, S.F., Maczurad, M., Mondillo, M., Santoro, L., 2020. Parent rock and climatic evolution control on the genesis of Ni-bearing clays in Ni-Co laterites: New inferences from the Wingellina deposit (Western Australia). Ore Geol. Rev. 120, 103431 https://doi.org/10.1016/j.oregeorev.2020.103431.
Putzolu, F., Santoro, L., Porto, C., Mondillo, N., Machado, M., De Almeida, B.S., Herrington, R., 2021. The influence of the magmatic to postmagmatic evolution of the parent rock on the Co deportment in lateritic systems: the example of the Santa Fé Ni-Co deposit (Brazil). Econ. Geol. https://doi.org/10.5382/econgeo.4819.
Putzolu, F., 2021. Mineralogy and geochemistry of Ni Co in lateritic profiles. Ph.D thesis. Università Federico II, Napoli Italy, p. 281 pp..
Qu, Y., Lian, B., Mo, B., Liu, C., 2013. Bioleaching of heavy metals from red mud using *Aspergillus niger*. Hydrometallurgy 136, 71–77. https://doi.org/10.1016/j.hydromet.2013.03.006.
Qu, Y., Li, H., Tian, W., Wang, X., Wang, X., Jia, X., Shi, B., Song, G., Tang, Y., 2015. Leaching of valuable metals from red mud via batch and continuous processes by using fungi. Min. Eng. 81, 1–4. https://doi.org/10.1016/j.mineng.2015.07.022.
Raous, S., Echevarria, G., Sterckeman, T., Hanna, K., Thomas, F., Martins, E.S., Becquer, T., 2013. Potentially toxic metals in ultramafic mining materials: identification of the main bearing and reactive phases. Geoderma 192, 111–119. https://doi.org/10.1016/j.geoderma.2012.08.017.
Ratiè, G., Jouvin, D., Garnier, J., Rouxel, O., Miska, S., Guimarães, E., Cruz Vieira, L., Sivry, Y., Zelano, I., Montarges-Pelletier, E., Thil, F., Quantin, C., 2015. Nickel isotope fractionation during tropical weathering of ultramafic rocks. Chem. Geol. 40, 68–76. https://doi.org/10.1016/j.chemgeo.2015.02.039.
Reid, S., Tam, J., Yang, M., Azimi, G., 2017. Technospheric mining of rare earth elements from bauxite residue (red mud): Process optimization, kinetic investigation, and microwave pretreatment. Sci. Rep. 7, 15252. https://doi.org/10.1038/s41598-017-15457-8.
Reimann, C., Filzmoser, P., Garrett, R., Dutter, R., 2011. Statistical Data Analysis Explained: Applied Environmental Statistics with R. John Wiley & Sons:, Hoboken, NJ, USA.
Rivera, R.M., Ulenaers, B., Ounoughene, G., Binnemans, K., Van Gerven, T., 2018. Extraction of rare earths from bauxite residue (red mud) by dry digestion followed by water leaching. Min. Eng. 119, 82–92. https://doi.org/10.1016/j.mineng.2018.01.023.
Rubisov, D.H., Papangelakis, V.G., 2000. Sulphuric acid pressure leaching of laterites — a comprehensive model of a continuous autoclave. Hydrometallurgy 58, 89–101. https://doi.org/10.1016/S0304-386X(00)00092-X.
Rubisov, D.H., Krowinkel, J.M., Papangelakis, V.G., 2000. Sulphuric acid pressure leaching of laterites — universal kinetics of nickel dissolution for limonites and limonitic/saprolitic blends. Hydrometallurgy 58, 1–11. https://doi.org/10.1016/S0304-386X(00)00094-3.
Russel, J.D., 1979. Infrared spectroscopy of ferrihydrite: evidence for the presence of structural hydroxyl groups. Clay Miner. 14, 109–113.
Salpeteur, I., Martel-Jantin, B., Rakotomanana, D., 1995. Pt and Pd mobility in ferralitic soils of the west Andriamena area Ž. Madagascar. Evidence of a supergene origin of some Pt and Pd minerals. Chron. Rech. Min. 520, 27–45.
Samouhos, M., Godelitsas, A., Nomikou, C., Taxiarchou, M., Tsakiridis, P., Zavašnik, J., Gamaletsos, P.N., Apostolikas, A., 2019. New insights into nanomineralogy and geochemistry of Ni-laterite ores from central Greece (Larymna and Evia deposits). Geochemistry 79, 268–279. https://doi.org/10.1016/j.geoch.2018.12.005.
Santoro, L., Boni, M., Herrington, R., Clegg, A., 2013. The Hakkari nonsulfide Zn-Pb deposit in the context of other nonsulfide Zn-Pb deposits in the Tethyan Metallogenic Belt of Turkey. Ore Geol. Rev. 53, 244–260. https://doi.org/10.1016/j.oregeorev.2013.01.011.
Santoro, L., Boni, M., Rollinson, G.K., Mondillo, N., Balassone, P., Clegg, A.M., 2014. Mineralogical characterization of the Hakkari nonsulfide Zn(Pb) deposit (Turkey): the benefits of QEMSCAN®. Min. Engin. 69, 29–39. https://doi.org/10.1016/j.mineng.2014.07.002.
Santoro, L., Boni, M., Mondillo, N., Joachimski, M., Woodman, J.A., 2015. Cold supergene zinc deposit in Alaska: the Reef Ridge case. Geol. Soc. Am. 127, 1534–1549. https://doi.org/10.1130/B31219.1.
Santoro, L., Putzolu, F., Mondillo, N., Boni, M., Herrington, R., 2020. Influence of genetic processes on geochemistry of Fe-oxy-hydroxides in supergene Zn non-sulfide deposits. Minerals 10, 602. https://doi.org/10.3390/min10070602.
Santoro, L., Putzolu, F., Mondillo, N., Herrington, R., Najorka, J., Boni, M., Dosbaba, M., Maczurad, M., Balassone, G., 2021. Quantitative mineralogical evaluation of Ni-Co laterite ores through XRPD-QPA- and automated SEM-based approaches: the Wingellina (Western Australia) case study. J. Geochem. Explor. 223 https://doi.org/10.1016/j.gexplo.2020.106695.
Santos-Ynigo, L., 1965. Distribution of iron, alumina, and silica in the Pujada laterite of Mati, Davao Province, Mindanao Island, Philippines. Philipp. Geol. 19, 97–110.
Schenck, C.V., Dillard, J.G., Murray, J.W., 1983. Surface analysis and the adsorption of Co (II) on goethite. J. Colloid Interface Sci. 95, 398–409. https://doi.org/10.1016/0021-9797(83)90199-6.
Schwertmann, U., Murad, E., 1983. Effect of pH on the formation of goethite and hematite from ferrihydrite. Clays Clay Min. 31, 277–1184. https://doi.org/10.1346/CCMN.1983.0310405.
Schwertmann, U., Latham, M., 1986. Properties of iron oxides in some New Caledonian Oxisols. Geoderma 39, 105–123. https://doi.org/10.1016/0016-7061(86)90070-4.
Schwertmann, U., Pfab, G., 1996. Structural vanadium and chromium in lateritic iron oxides: genetic implications. Geoch. Cosmoch. Acta 60 (21), 4279–4283. https://doi.org/10.1016/S0016-7037(96)00259-1.
Schwertmann, U., Cornell, R.M., 2007. Iron Oxides in the Laboratory: Preparation and characterization. Wiley-VCH, Weinheim.

Schwertmann, U., Stanjek, H., Becher, H.-H., 2004. Long-term in vitro transformation of 2-line ferrihydrite to goethite/hematite at 4, 10, 15 and 25 °C. Clay Min. 39, 433–438. https://doi.org/10.1180/0009855043940145.

Siehl, A., Thein, J., 1989. Minette-type ironstones. In: Young, T.P., Taylor, W.E.G. (Eds.), Phanerozoic Ironstones. Geological Society of London, Special Publication. Geological Society of London, pp. 175–193.

Singh, B., Sherman, D.M., Gilkes, R.J., Wells, M.A., Mosselmans, J., 2002. Incorporation of Cr, Mn and Ni into goethite (α-FeOOH): mechanism from extended X-ray absorption fine structure spectroscopy. Clay Miner. 37, 639–649. https://doi.org/10.1180/000985502374066.

Smith, S.L., Grail, B.M., Johnson, D.B., 2017. Reductive bioprocessing of cobalt-bearing limonitic laterites. Min. Eng. 106, 86–90. https://doi.org/10.1016/j.mineng.2016.09.009.

Song, Y., Swedlund, P.J., Zou, C., Dol Hamid, R., 2013. The influence of surface structure on H_4SiO_4 sorption and oligomerization on goethite surfaces: an XPS study using goethites differing in morphology. Chem. Geol. 347, 114–122. https://doi.org/10.1016/j.chemgeo.2013.03.014.

Sufriadin, S., Idrus, A., Pramumijoyo, S., Warmada, I.W., Imai, A., 2011. Study on mineralogy and chemistry of the saprolitic nickel ores from Soroako, Sulawesi, Indonesia: implication for the lateritic ore processing. J. Southeast Asian Appl. Geol. 3, 23–33. https://doi.org/10.22146/jag.7178.

Swedlund, P.J., Webster, J.G., 1999. Adsorption and polymerization of silicic acid on ferrihydrite, and its effect on arsenic adsorption. Water Res. 33, 3413–3422. https://doi.org/10.1016/S0043-1354(99)00055-X.

Swedlund, P.J., Hamid, R.D., Miskelly, G.M., 2010. Insights into H_4SiO_4 surface chemistry on ferrihydrite suspensions from ATR-IR, Diffuse Layer Modeling and the adsorption enhancing effects of carbonates. J. Colloid. and Interface Sci. 352, 149–157. https://doi.org/10.1016/j.jcis.2010.08.011.

Talvan, M., Thorne, R., Herrington, R.J., 2011. Uplift and lateritization history of Çaldağ ophiolite in the context of Neo-Tethyan ophiolite obduction and uplift: implications for Cenozoic weathering history of western Anatolia. J. Geol. Soc. London 168, 927–940. https://doi.org/10.1144/0016-76492010-086.

Tauler, E., Lewis, J.F., Villanova-de-Benavent, C., Aiglsperger, T., Proenza, J.A., Domènech, C., Gallardo, T., Longo, F., Galí, S., 2017. Discovery of Ni-smectite-rich saprolite at Loma Ortega, Falcondo mining district (Dominican Republic): Geochemistry and mineralogy of an unusual case of "hybrid hydrous Mg silicate–clay silicate" type Ni-laterite. Miner. Deposita 52 (7), 1011–1030. https://doi.org/10.1007/s00126-017-0750-8.

Taylor, D., Dalstra, H.J., Harding, A.E., Broadbent, G.C., Barley, M.E., 2001. Genesis of high-grade hematite orebodies of the Hamersley Province, Western Australia. Econ. Geol. 96, 837–873. https://doi.org/10.2113/gsecongeo.96.4.837.

Teitler, Y., Cathelineau, M., Ulrich, M., Ambrosi, J.P., Munoz, M., Sevin, B., 2019. Petrology and geochemistry of scandium in New Caledonian Ni-Co laterites. J. Geochem. Explor. 196, 131–155. https://doi.org/10.1016/j.gexplo.2018.10.009.

Thorne, R., Herrington, R., Roberts, S., 2009. Composition and origin of Çaldağ oxide nickel laterite, W. Turkey. Miner. Deposita 44, 581–595. https://doi.org/10.1007/s00126-009-0234-6.

Thorne, R., Roberts, S., Herrington, R., 2012. Climate change and formation of nickel laterite deposits. Geology 40, 331–334. https://doi.org/10.1130/G32549.1.

Tobón, M., Weber, M., Proenza, J.A., Aiglspergers, T., Betancur, S., Farré-de-Pablo, J., Ramiréz, C., Pujol-Solà, N., 2020. Geochemistry of Platinum-Group Elements (PGE) in Cerro Matoso and Planeta Rica. Boletín Soc. Geol. Mex. 72 (3) https://doi.org/10.18268/BSGM2020v72n3a201219. A201219.

Tóth, T.M., Schubert, F., Raucsik, B., Fintor, K., 2019. Mineralogical and geochemical constraints of the REE accumulation in the Almásfüzitő red mud depository in Northwest Hungary. Appl. Sci. 9, 3654. https://doi.org/10.3390/app9183654.

Towe, K.M., Bradley, W.F., 1967. Mineralogical constitution of colloidal "'hydrous ferric oxides'.". J. Colloid Interf. Sci. 24, 383–392. https://doi.org/10.1016/0021-9797(67)90266-4.

Tupaz, C.A.J., Watanabe, Y., Sanematsu, K., Echigo, T., Arcilla, C., Ferrer, C., 2020a. Ni-Co mineralization in the Intex laterite deposit, Mindoro, Philippines. Minerals 10, 579. https://doi.org/10.3390/min10070579.

Trolard, F., Bourrie, G., Jeanroy, E., Herbillon, A.J., Martin, H., 1995. Trace metals in natural iron oxides from laterites: A study using selective kinetic extraction. Geochim. et Cosmochim. Acta 59 (7), 1285–1297. https://doi.org/10.1016/0016-7037(95)00043-Y.

Tupaz, C.A.J., Watanabe, Y., Sanematsu, K., Echigo, T., 2020b. Mineralogy and geochemistry of the Berong Ni-Co laterite deposit, Palawan, Philippines. Ore Geol. Rev. 125, 103686 https://doi.org/10.1016/j.oregeorev.2020.103686.

Ulrich, M., Picard, C., Guillot, S., Chauvel, C., Cluzel, D., Meffre, S., 2010. Multiple melting stages and refertilization as indicators for ridge to subduction formation: the New Caledonia ophiolite. Lithos 115, 223–236. https://doi.org/10.1016/j.lithos.2009.12.011.

Ulrich, M., Cathelineau, M., Munoz, M., Boiron, M.C., Teitler, Y., Karpoff, A.M., 2019. The relative distribution of critical (Sc, REE) and transition metals (Ni Co, Cr, Mn, V) in some Ni laterite deposits of New Caledonia. J. Geochem. Explor. 197, 93–113. https://doi.org/10.1016/j.gexplo.2018.11.017.

USGS Mineral Commodities Summary 2021. <https://www.usgs.gov/centers/nmic/nickel-statistics-and-information>. (accessed 02/2021).

Villacís-García, M., Ugalde-Arzate, M., Vaca-Escobar, K., Villalobos, M., Zanella, R., Martínez-Villegas, N., 2015. Laboratory synthesis of goethite and ferrihydrite of controlled particle sizes. Bol. Soc. Geol. Mex. 67, 433–446. https://doi.org/10.18268/bsgm2015v67n3a7.

Villalobos, M., Leckie, J.O., 2001. Surface complexation modeling and FTIR study of carbonate adsorption to goethite. J. Colloid Interface Sci. 235, 15–32. https://doi.org/10.1006/jcis.2000.7341.

Villanova-de-Benavent, C., Proenza, J.A., Galí, S., García-Casco, A., Tauler, E., Lewis, J. F., Longo, F., 2014. Garnierites and garnierites: textures, mineralogy and geochemistry of garnierites in the Falcondo Ni-laterite deposit, Dominican Republic. Ore Geol. Rev. 58, 91–109. https://doi.org/10.1016/j.oregeorev.2013.10.008.

Vind, J., Malfliet, A., Bonomi, C., Paiste, P., Sajó, I.E., Blanpain, B., Tkaczyk, A.H., Vassiliadou, V., Panias, D., 2018. Modes of occurrences of scandium in Greek bauxite and bauxite residue. Min. Engin. 123, 35–48. https://doi.org/10.1016/j.mineng.2018.04.025.

Vitovskaya, I.V., 1989. Mineral forms and concentration mechanisms in lateritic deposits. In: Weathering its Products and Deposits, vol. II. Products-Deposits-Geotechnics. Theophratus publications, 144–169.

Wang, X.Q., Xie, K.Q., Ma, W.H., Yang, M.Y., Zeng, P., Cao, Y.C., 2013. Recovery of zinc and other valuable metals from zinc leach residue by top blowing fuming method. Min. Proc. Ext. Met. Rev. 122, 174–178. https://doi.org/10.1179/1743285513Y.0000000045.

Wells, M.A., Ramanaidou, E.R., Verrall, M., Tessarolo, C., 2009. Mineralogy and crystal chemistry of "garnierites'' in the Goro lateritic nickel deposit, New Caledonia. Eur. J. Mineral. 21, 467–483. https://doi.org/10.1127/0935-1221/2009/0021-1910.

Yongue-Fouateu, R., Ghogomu, R.T., Penaye, J., Ekodeck, G.E., Stendal, H., Colin, F., 2006. Nickel and cobalt distribution in the laterites of the Lomié region, south-east Cameroon. J. Afr. Earth Sc. 45, 33–47. https://doi.org/10.1016/j.jafrearsci.2006.01.003.

Yu, X., Zhu, L., Guo, B., He, S., 2009. A study on the adsorption of chromium on laterite from Guizhou Province, China. Chin. J. Geochem. 28, 220–226. https://doi.org/10.1007/s11631-009-0220-9.

Zachariáš, J., Wilkinson, J., 2007. Exlam 2000: Excel VBA application for processing of transient signals from laser ablation (LA-ICPMS) of fluid inclusions and solid phases. In: Proceedings of the ECROFI-XIX Biennial Conference on European Current Research on Fluid Inclusions, Bern, Switzerland.

Zhang, N., Li, H.X., Liu, X.M., 2016. Recovery of scandium from bauxite residue—red mud: a review. Rare Met. 35, 887–900. https://doi.org/10.1007/s12598-016-0805-5.